

Cavity optomechanics with whispering-gallery mode optical micro-resonators

Albert Schliesser^a and Tobias J. Kippenberg^{a,b}

^a*Max-Planck-Institut für Quantenoptik, D-85478 Garching, Germany*

^b*École Polytechnique Fédérale de Lausanne (EPFL), CH-1015 Lausanne, Switzerland*

Abstract

Parametric coupling of optical and mechanical degrees of freedom forms the basis of many ultra-sensitive measurements of both force and mechanical displacement. An optical cavity with a mechanically compliant boundary enhances the optomechanical interaction, which gives rise to qualitatively new behavior which can modify the dynamics of the mechanical motion. As early as 1967, in a pioneering work, V. Braginsky analyzed theoretically the role of radiation pressure in the interferometric measurement process, but it has remained experimentally unexplored for many decades. Here, we use whispering-gallery-mode optical microresonators to study these radiation pressure phenomena. Optical microresonators simultaneously host optical and mechanical modes, which are systematically analyzed and optimized to feature ultra-low mechanical dissipation, photon storage times exceeding the mechanical oscillation period (i.e. the “resolved-sideband regime”) and large optomechanical coupling. In this manner, it is demonstrated for the first time that dynamical backaction can be employed to cool mechanical modes, i.e., to reduce their thermally excited random motion. Utilizing this novel technique together with cryogenic pre-cooling of the mechanical oscillator, the phonon occupation of mechanical radial-breathing modes could be reduced to $\langle n \rangle = 63 \pm 20$ excitation quanta. The corresponding displacement fluctuations are monitored interferometrically with a sensitivity at the level of $1 \cdot 10^{-18} \text{ m}/\sqrt{\text{Hz}}$, which is below the imprecision at the standard quantum limit (SQL). This implies that the readout is already in principle sufficient to measure the quantum mechanical zero-point position fluctuations of the mechanical mode. Moreover, it is shown that optical measurement techniques employed here are operating in a near-ideal manner according to the principles of quantum measurement, displaying a backaction-imprecision product close to the quantum limit.

Contents

1	Introduction	2
2	Theory of optomechanical interactions	9
2.1	Classical description and elementary phenomenology	9

2.2	Formal framework: quantum Langevin equations	16
3	WGM resonators as optomechanical systems	19
3.1	Optical properties of WGM silica microresonators	20
3.2	Optomechanical coupling in silica WGM resonators	21
3.3	Optomechanical coupling	37
4	Ultrahigh-sensitivity interferometric motion transduction	44
4.1	Theoretical limits of displacement sensing	44
4.2	Experimental techniques	49
4.3	Observation and analysis of quantum and thermal noises	55
5	Observation of dynamical backaction	59
5.1	Optical spring and optical damping	59
5.2	Radiation pressure cooling by dynamical backaction	62
5.3	Radiation pressure versus thermal effects	65
6	Resolved-sideband cooling	70
6.1	Ground state cooling: the atomic physics case	70
6.2	Limits of radiation-pressure cooling using dynamical backaction	72
6.3	Resolved-sideband cooling of a silica microtoroid	75
6.4	Direct sideband spectroscopy	81
7	Approaching the quantum ground state	85
7.1	Implementation	85
7.2	Cooling towards the quantum ground state	94
7.3	Assessing measurement backaction	97
8	Conclusion	101
9	Outlook	104
	Acknowledgements	108
	References	108

1 Introduction

The tails of comets always point away from the sun. Kepler, in the 17th century, already conjectured from this observation that sunlight exerts a force on particles in the comet tail. Some 250 years later, Maxwell’s theory of electromagnetic radiation put this conjecture on solid theoretical grounds, yet, collecting experimental evidence for the fact that light carries momentum has eluded even the most skilled experimentalists of that age. As a famous example, Crookes attempted to construct a radiometer in which the transfer of optical momentum makes a vane spin, now famous as the “light mill” (figure 1).



Fig. 1. Radiometer used by Crookes around 1877. The pivoted vanes, each silvered and blackened on one face, are free to revolve around the central axis. Crookes observed that the vanes started to turn when illuminated by a strong light source. The origin of the effect was not radiation pressure, it was mediated by the dilute gas still present in the globe. In refined experiments by Lebedev in Russia and Hull in the US, effects of radiation pressure on mechanical objects were observed at the beginning of the 20th century. Image copyright Science Museum/SSPL, London, reproduced with permission.

After much debate, however, it was understood that the observed rotation is mediated by the dilute gas in which the vane is kept (Woodruff (1968)). True radiation-pressure effects, in agreement with Maxwell’s predictions, were not observed until the beginning of the 20th century, in more sophisticated experiments carried out by Lebedew in Russia (Lebedew (1901)) and Nichols and Hull in the United States (Nichols and Hull (1901, 1903a,b)).

The situation changed dramatically with the advent of lasers as highly coherent light sources in the 1970s. It was soon suggested that one could *utilize* the resulting forces to manipulate the motion of dielectric particles and atoms or ions in a controlled manner. Pioneering work of Ashkin at Bell Laboratories demonstrated trapping of dielectric particles using radiation pressure, a technique still widely adopted today and known as “optical tweezers” (Ashkin (1970)). Soon thereafter, proposals to utilize the laser field to cool the motion of atoms emerged. Hänsch and Schawlow (Hänsch and Schawlow (1975)) and also Wineland and Dehmelt (Wineland and Dehmelt (1975); Wineland and Itano (1979)) suggested ways to use radiation pressure to dampen the random motion of atoms or ions, now widely known as “laser cooling”. Ashkin and Chu demonstrated this principle to trap and cool neutral particles using optical forces (Ashkin (1978); Chu et al. (1985)). In the decades to follow, the implementation of these ideas lead to what can be considered a true revolution in atomic physics, pivotal for discoveries such as Bose-Einstein condensation

and the development of the most precise frequency standards available today.

Among the most spectacular advances of this laser control is the demonstration of quantum ground state cooling of a harmonically trapped ion (Diedrich et al. (1989); Monroe et al. (1995); Hamann et al. (1998)), which has enabled the generation of such exotic motional states as Fock or Schrödinger cat states (Leibfried et al. (2003)) of a single trapped ion. However, it is a prime example of the enigmatic quantum-classical “boundary” that such quantum effects and state preparation have never been accomplished with mechanical oscillators. It is an interesting, yet little known fact that the ramifications of radiation pressure on mechanical oscillators is a subject that even predates the work of Ashkin and co-workers.

Braginsky’s group at Moscow state university has played a pioneering role in this regard. Embedded eventually in a very general theory of quantum measurements (Braginsky et al. (1980); Braginsky and Khalili (1992, 1996); Braginsky et al. (2003)), Braginsky considered already in the year 1967 the role of radiation pressure in an optical interferometer (Braginskii and Manukin (1967)). Since the end mirrors of a interferometer are mechanically compliant they are subject to a radiation pressure force. An important impetus for such *theoretical* analysis has been the use of interferometers as detectors for gravitational waves. The exquisite sensitivity required in these experiments caused a strong theoretical interest in understanding the limits of linear continuous displacement measurements based on parametric transducers. Braginsky identified two important consequences of the radiation pressure force that photons exert on the interferometer end mirrors, and has developed a comprehensive understanding of optomechanical interactions as they occur in the fundamental building block of a gravitational wave observatory shown in figure 2: Monochromatic light trapped in a high-finesse cavity (a Fabry-Perot resonator in this case) exerts radiation pressure on the massive end mirrors, coupling their oscillatory motion to the light.

As early as 1967 Braginsky and coworkers (Braginskii and Manukin (1967)) recognized that radiation pressure can change the dynamics of the mechanical degree of freedom, effectively adding an optically induced viscous damping to the mirror motion. It was also soon understood that this phenomenon (termed *dynamical backaction* (Braginskii and Manukin (1967); Braginskii et al. (1970); Braginsky and Manukin (1977); Braginsky et al. (2001))) could be used in principle to amplify or cool the motion of the mirror (Dykman (1978); Braginsky and Vyatchanin (2002)) - which is in essence very similar to the principle of laser cooling of atoms, discovered in the decade to follow. While dynamical backaction is a classical effect, Braginsky and co-workers also showed that the quantum nature of light within the interferometer gives rise to an unsurmountable sensitivity limit in displacement measurements of the mirror: For sufficiently strong input power, quantum fluctuations of the radiation pres-

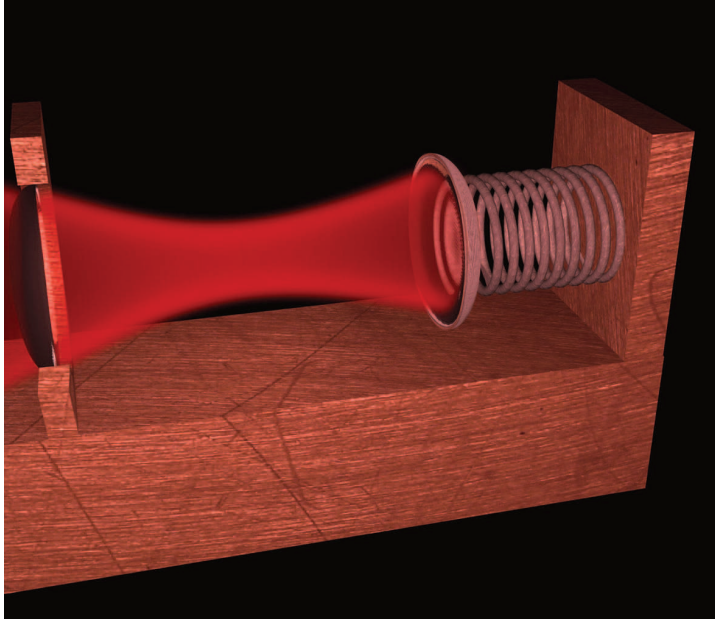


Fig. 2. Artist's view of a generic optomechanical system: A Fabry-Perot resonator, consisting of two mirrors trapping near-resonant monochromatic light. One of the mirrors is mechanically compliant, here it is mounted on a spring and therefore constitutes a mechanical harmonic oscillator.

sure force induces random motion in the mirror, that masks the displacement to be detected (Braginsky and Khalili (1992); Caves (1980, 1981)) by e.g. a gravitational wave, an effect now referred to as the *quantum backaction* of the measurement. While the Moscow group devoted many decades in the development of parametric transducers for gravity wave detection, it was not possible to observe the dynamical backaction cooling or amplification, though pioneering attempts (Braginskii et al. (1970)) were made by the Moscow group in 1969.

Interest in optomechanics reemerged in the 1990 in the context of quantum optics, resulting in a variety of proposals exploring quantum effects in these systems, ranging from proposal for quantum non-demolition measurements of the light intensity or single quadrature measurements of the mechanical displacement (Braginsky et al. (1977, 1980); Braginsky and Khalili (1996); Heidmann et al. (1997)), as well as the generation of narrow-band squeezed light using the mechanical oscillator as an effective third-order-nonlinearity (Fabre et al. (1994); Mancini and Tombesi (1994)). Later work has studied in great detail the possibility to generate non-classical states of motion (Bose et al. (1997)), including superposition states (Marshall et al. (2003)), entangled states of several oscillators (Mancini et al. (2002); Zhang et al. (2003); Pinard et al. (2005); Bhattacharya et al. (2008b)), or motional states entangled with optical degrees of freedom (Vitali et al. (2007); Bhattacharya et al. (2008a)). As a special quantum state, it has also been suggested to cool the mechanical degree of freedom to its quantum ground state using cooling by dynamical

backaction (Wilson-Rae et al. (2007); Marquardt et al. (2007); Bhattacharya and Meystre (2007); Genes et al. (2008); Dantan et al. (2008)).

Observing such phenomena *experimentally* however, had been severely complicated by several experimental challenges. First, optomechanical coupling by radiation pressure is usually weak—the momentum transfer of a single reflected photon changes the velocity of a (free) gram-scale mass by some 10^{-24} m/s only. At the same time, the oscillator displacements associated with quantum effects are typically on the scale of its zero-point fluctuations $x_{\text{ZPF}} = \sqrt{\hbar/2m\Omega_m}$, where m and Ω_m are its mass and the resonance frequency, respectively. For gram-scale oscillators, such as a small end mirror in an interferometer, this motion is almost ten orders of magnitude smaller than the fluctuations of a trapped atom or ion—usually at the sub-attometer scale. Dedicated experiments (Bocko and Onofrio (1996); Tittonen et al. (1999); Hadjar et al. (1999); Caniard et al. (2007a)) have been approaching such sensitivities, but another challenge persists in all room-temperature experiments: Thermal noise tends to mask quantum signatures (caused e. g. by quantum backaction) as long as the thermal energy $k_B T$ largely exceeds the energy scale $\hbar\Omega_m$ of the motional quantum (k_B is the Boltzmann, and \hbar the reduced Planck constant).

In recent years, the tremendous progress in micro- and nanofabrication technologies has provided novel opportunities to engineer optomechanical devices. For example, toroidal whispering-gallery mode optical microresonators were shown to exhibit optomechanical coupling to mechanical modes of the structure (Kippenberg et al. (2005); Rokhsari et al. (2005)). The high quality factors of their optical and mechanical modes allowed observing radiation pressure amplification and coherent oscillations for the first time in 2005 (Kippenberg et al. (2005); Rokhsari et al. (2005)). A wide variety of other optomechanical systems has since emerged, ranging from the nano- to the macroscale. With the advent of these new optomechanical systems, interest in observing their quantum mechanical properties (Schwab and Roukes (2005)) revived, an effort pursued predominantly with electronic transducers up to that point. The new research field, now widely referred to as *cavity (quantum) optomechanics* (Kippenberg and Vahala (2007, 2008)), uses a remarkably diverse set of experimental systems as depicted in table 1, which summarizes the properties of optomechanical systems studied in the last ten years, reflecting also the enormous parameter range covered.

Within this work, we have developed optomechanical systems based on silica whispering-gallery mode (WGM) microresonators. Their compactly co-located high-quality optical and mechanical modes render microresonators a very favorable system for the study of radiation-pressure induced optomechanical coupling. Indeed, we show here that basically all experimental challenges for the observation of quantum effects can be successfully addressed with this system, providing a route to ground state cooling of a mechanical oscillator or

Table 1: Key parameters of recently studied optomechanical systems. Earlier results are summarized in ref. (Bocko and Onofrio (1996)).

System	Resonance frequency (Hz)	Quality factor ^a	Effective mass (g)	Displacement sensitivity ^b (m/ $\sqrt{\text{Hz}}$)	References ^c
Internal modes of a silica mirror	$1.86 \cdot 10^6$	40,000	$230 \cdot 10^{-3}$		(Cohadon et al. (1999))(Pinard et al. (2000); Caniard et al. (2007b); Verlot et al. (2008))
Silicon torsional oscillator	$26 \cdot 10^3$	$4,300,000^d$	$10 \cdot 10^{-3}$	$2.0 \cdot 10^{-16}$	(Tittonen et al. (1999))(Hahtela et al. (2004))
AFM cantilevers (thermal)	$7.28 \cdot 10^3$	2,000			(Höhberger Metzger and Karrai (2004))(Ludwig et al. (2008b))
Silicon micromirror	$0.81 \cdot 10^6$	10,000	$190 \cdot 10^{-6}$	$2.0 \cdot 10^{-18}$	(Arcizet et al. (2006b))(Arcizet et al. (2006a, 2008))
Free standing Bragg mirror	$278 \cdot 10^3$	9,000	$400 \cdot 10^{-9}$	$\sim 10^{-16}$	(Böhm et al. (2006)) (Gigan et al. (2006)); Gröblacher et al. (2008); Cole et al. (2008))
Dielectric micromirror on silicon cantilever	$12.5 \cdot 10^3$	18,000	$24 \cdot 10^{-9}$	$1 \cdot 10^{-13}$	(Kleckner and Bouwmeester (2006))(Kleckner et al. (2006))
Silica microtoroids	$40.6 \cdot 10^6$	$31,000^e$	$10 \cdot 10^{-9}$	$1.0 \cdot 10^{-18}$	(Schliesser et al. (2006, 2008a, 2009))
Spiky silica microtoroids	$38.0 \cdot 10^6$	$80,000^f$			(Anetsberger et al. (2008))
Silica microspheres	$87.2 \cdot 10^6$	15,600			(Ma et al. (2007))(Park and Wang (2007))
Chip-based silica microsphere	$1.08 \cdot 10^9$				(Carmon and Vahala (2007))
Big suspended mirrors	173	3,200	1		(Corbitt et al. (2007a)); (Corbitt et al. (2007b))
Ultrasoft silicon cantilever	$3.3 \cdot 10^3$	$44,200^g$	$140 \cdot 10^{-12}$	$1 \cdot 10^{-12}$	(Poggio et al. (2007))
Silicon cantilever	$7 \cdot 10^3$	20,000	$2.4 \cdot 10^{-6}$		(Brown et al. (2007))
Silicon nitride membrane	$135 \cdot 10^3$	$12,000,000^h$	$40 \cdot 10^{-9}$	$4.5 \cdot 10^{-16}$	(Thomson et al. (2008))(Zwickl et al. (2008))
Gold-coated silicon micropaddle	$547 \cdot 10^3$	1,060	$11 \cdot 10^{-12}$		(Favero et al. (2007))
Silica nanowire	193^i		$26 \cdot 10^{-9}$		(Eichenfield et al. (2007))
Mirror on a flexure mount	85	44,500	0.69	$3 \cdot 10^{-15}$	(Mow-Lowry et al. (2008))
Nanomechanical resonator coupled to SCMWR ^j	$1.53 \cdot 10^6$	300,000	$6.2 \cdot 10^{-12}$	$45 \cdot 10^{-15}$	(Teufel et al. (2008))(Regal et al. (2008); Hertzberg et al. (2009); ?)
Resonant-bar gravitational wave detector ^k	865	1,200,000	$1.1 \cdot 10^{+6}$		(Vinante et al. (2008))
Silicon photonic circuit	$8.87 \cdot 10^6$	1,850		$18 \cdot 10^{-15}$	(Li et al. (2008))
Silicon nitride "zipper" cavity	$8.2 \cdot 10^6$	~ 100	$43 \cdot 10^{-12}$	$2 \cdot 10^{-15}$	(Eichenfield et al. (2009a))
Suspended mirrors in LIGO ^l	140		$2.7 \cdot 10^{+3}$	$2 \cdot 10^{-19}$	(LIGO Scientific Collaboration (2009))
Ta ₂ O ₅ /SiO ₂ Bragg mirror on Si ₃ N ₄ beam	$945 \cdot 10^3$	30,000 ^m	$43 \cdot 10^{-9}$	$1 \cdot 10^{-16}$	(Gröblacher et al. (2009b))
e ⁻ -beam deposited nanorod	$1.9 \cdot 10^6$	6,500		$1 \cdot 10^{-13}$	(Favero et al. (2009))
Silica double-disk resonator	$8.5 \cdot 10^6$	4,070		$2 \cdot 10^{-15}$	(Lin et al. (2009))
Silicon optomechanical crystal	$2.3 \cdot 10^9$	1,300	$330 \cdot 10^{-15}$		(Eichenfield et al. (2009b))
Silicon nitride nanoresonator	$10.7 \cdot 10^6$	53,000	$3.6 \cdot 10^{-12}$	$6.4 \cdot 10^{-16}$	(Anetsberger et al. (2009))
Trapped ion	$71 \cdot 10^3$		$4.0 \cdot 10^{-23}$		(Vahala et al. (2009))
CaF ₂ WGM resonator	$1.06 \cdot 10^6$	136,000	0.5		(Hofer et al. (2009))

^aat room temperature unless noted otherwise, ^bexperimental value, including all noise except for the mechanical mode of interest, ^cquoted numbers are from the references printed in bold, ^dat 2K, at room temperature 250,000, ^eat room temperature, for values at cryogenic temperatures see ref. (Arcizet et al. (2009)), ^fat 410 K, at room temperature 32,000, ^gat 4.2 K, at room temperature 16,000, ^hat 300 mK, at room temperature 1,100,000, ⁱthe device is operated at d.c., ^jsuperconducting microwave resonator, ^kthe resonance is a combined mechanical and electronic resonance, ^llaser interferometer gravitational wave interferometer. The resonance frequency is increased by electronic feedback on actuators controlling the mirror position, ^mat 5.3 K, at room temperature 5,000

measurement of its zero point motion. As a key enabling step towards these studies, it has been possible for the first time to demonstrate radiation-pressure cooling of a mesoscopic mechanical oscillator based on optically induced dynamical backaction (Schliesser et al. (2006)). Adapting, in addition, advanced quantum optical and cryogenic techniques to this setting, we show experimentally that these systems are capable of closely approaching fundamental quantum limits—both in terms of the quality of the displacement sensitivity, reaching an imprecision below that at the SQL—and the occupation of the mechanical oscillator.

2 Theory of optomechanical interactions

2.1 Classical description and elementary phenomenology

To begin the discussion of cavity optomechanics, it is useful to review some basic underlying physical concepts and simple limiting cases. Consider the generic optomechanical system depicted in figure 3(a). The impinging field $s_{\text{in}}(t)$ drives the cavity mode amplitude $a(t)$. Part of the boundary of this mode—in the simplest case, one of the end mirrors of a Fabry-Perot cavity—is free to move, and its displacement is described by the one-dimensional variable $x(t)$. Irrespective of the spatial structure of both the optical mode and the mechanical displacement pattern, we assume that the displacement $x(t)$ shifts the resonance frequency of the optical mode in a linear fashion,

$$\omega'_c(t) = \omega_c + g_0 x(t), \quad (1)$$

where ω_c is the cavity resonance frequency for $x = 0$ and

$$g_0 \equiv \frac{\partial \omega'_c}{\partial x} \quad (2)$$

is the optomechanical coupling constant. For the cases depicted in figure 3, $g_0 = -\omega_c/L$ for a Fabry-Perot cavity of length L , and $g_0 = -\omega_c/R$ for a WGM resonator of radius R .

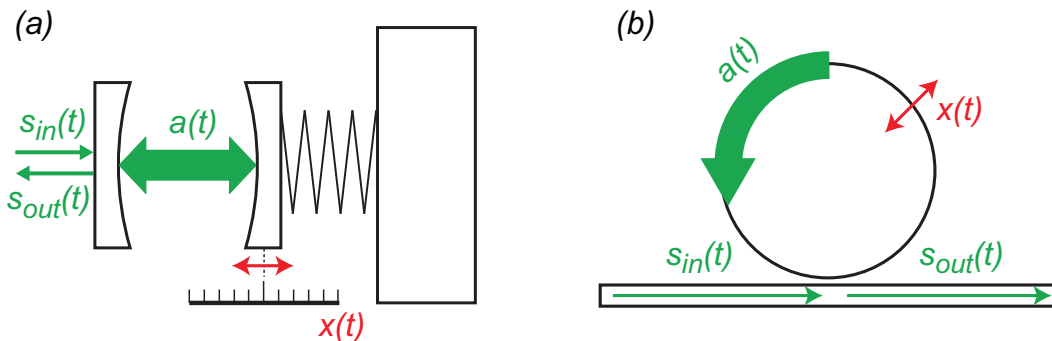


Fig. 3. Schematic of two generic geometries of optomechanical systems. (a) Linear Fabry-Perot-type cavity with a movable mirror, pumped through a partially transparent mirror. (b) Whispering-gallery mode resonator pumped by evanescent coupling to a waveguide. In both cases, an incoming field $s_{\text{in}}(t)$ drives the intracavity field $a(t)$. The cavity resonance frequency depends on the displacement $x(t)$ of a cavity boundary from its equilibrium position.

2.1.1 A moving cavity boundary

We will first discuss the effect of a moving cavity boundary on the optical mode, and neglect the backaction (radiation pressure) of the light. For a monochromatic pump wave $\bar{s}_{\text{in}}e^{-i\omega_1 t}$, the resulting equation of motion for the intracavity field amplitude reads (following the notation of (Haus (1984)))

$$\dot{a}(t) = \left(-i(\omega_c + g_0 x(t)) - \frac{\kappa}{2} \right) a(t) + \sqrt{\eta_c \kappa} \bar{s}_{\text{in}} e^{-i\omega_1 t} \quad (3)$$

Here, $a(t)$ and $\bar{s}_{\text{in}}(t)$ are the amplitudes of the field in the cavity, and the driving field, respectively, normalized such that $|a(t)|^2$ is the intracavity photon number and $|\bar{s}_{\text{in}}(t)|^2$ the photon flux impinging on the cavity. Furthermore, ω_1 is the laser field angular frequency, κ the cavity energy decay rate, and $\eta_c \equiv \tau_0/(\tau_0 + \tau_{\text{ex}}) \in [0 \dots 1]$ describes the degree of overcoupling, τ_0 and τ_{ex} being the cavity photon lifetimes due to intrinsic losses of the cavity and coupling to the taper waveguide, respectively. As one of the simplest cases, we analyze the response of the driven cavity to a sinusoidal oscillation in the mechanical degree of freedom. For $x(t) = x_0 \sin(\Omega_m t)$, the solution for the mode amplitude reads

$$a(t) = \sqrt{\eta_c \kappa} \bar{s}_{\text{in}} \sum_{n=-\infty}^{+\infty} \frac{i^n J_n(\beta)}{-i(\omega_1 + n\Omega_m - \omega_c) + \kappa/2} e^{-i(\omega_1 + n\Omega_m)t - i\beta \cos(\Omega_m t)} \quad (4)$$

after all transients have decayed within a timescale of κ^{-1} (Schliesser et al. (2008b)). Here, the J_n are the Bessel functions of the first kind and $\beta = g_0 x_0 / \Omega_m$ is the modulation index. For small amplitudes x_0 , so that $|\beta| \ll 1$, the intracavity field can be approximated to

$$a(t) \approx a_0(t) + a_1(t) + \mathcal{O}(\beta^2) \quad (5)$$

$$a_0(t) = \frac{\sqrt{\eta_c \kappa} \bar{s}_{\text{in}}}{-i\Delta + \kappa/2} e^{-i\omega_1 t} \quad (6)$$

$$a_1(t) = \frac{g_0 x_0}{2} \frac{\sqrt{\eta_c \kappa} \bar{s}_{\text{in}}}{-i\Delta + \kappa/2} \left(\underbrace{\frac{e^{-i(\omega_1 + \Omega_m)t}}{-i(\Delta + \Omega_m) + \kappa/2}}_{\text{anti-Stokes}} - \underbrace{\frac{e^{-i(\omega_1 - \Omega_m)t}}{-i(\Delta - \Omega_m) + \kappa/2}}_{\text{Stokes}} \right), \quad (7)$$

where $\Delta = \omega_1 - \omega_c$ is the laser detuning. Evidently, the moving boundary acts as a modulator, building up a pair of sidebands a_1 in the cavity, with weights proportional to the cavity Lorentzian evaluated at the frequencies $\omega_1 + \Omega_m$ and $\omega_1 - \Omega_m$ for the upper and lower sideband, respectively. These sidebands, schematically shown in figure 4, are also often referred to as anti-Stokes and Stokes sidebands (Kippenberg et al. (2005)).

The presence of these sidebands corresponds to a modulation of the intracavity

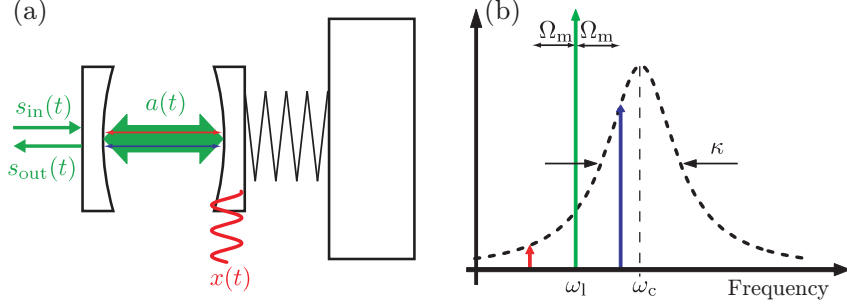


Fig. 4. Response of a driven cavity to an oscillating end mirror (a), which leads to the generation of anti-Stokes and Stokes sidebands at frequencies $\omega_1 + \Omega_m$ and $\omega_1 - \Omega_m$, weighted by the cavity Lorentzian (b).

photon number $|a(t)|^2$, and it is easy to show that

$$\begin{aligned}
 |a(t)|^2 &\approx |a_0(t)|^2 + a_0(t)a_1^*(t) + a_0^*(t)a_1(t) = \\
 &= \frac{\eta_c \kappa |\bar{s}_{\text{in}}|^2}{\Delta^2 + (\kappa/2)^2} \left(1 + \right. \\
 &\quad g_0 x_0 \left(\frac{\Delta + \Omega_m}{(\Delta + \Omega_m)^2 + (\kappa/2)^2} + \frac{\Delta - \Omega_m}{(\Delta - \Omega_m)^2 + (\kappa/2)^2} \right) \sin(\Omega_m t) + \\
 &\quad \left. g_0 x_0 \left(\frac{\kappa/2}{(\Delta + \Omega_m)^2 + (\kappa/2)^2} - \frac{\kappa/2}{(\Delta - \Omega_m)^2 + (\kappa/2)^2} \right) \cos(\Omega_m t) \right). \tag{8}
 \end{aligned}$$

The intracavity optical photon number is modulated at the oscillation frequency Ω_m , however, the modulation does not necessarily occur in phase with the mechanical oscillation as is evident from the cosine-term. In fact, the phase lag depends in a non-trivial manner on the laser detuning Δ , oscillation frequency Ω_m and the cavity buildup time κ^{-1} , a simple calculation yields for the phase lag

$$\phi_{\text{lag}} = \arg \left(g_0 \Delta (\Delta^2 + (\kappa/2)^2 - \Omega_m^2 - i\Omega_m \kappa) \right), \tag{10}$$

which is shown in figure 5. The quadrature component ($\propto \cos(\Omega_m t)$) can become significant if the cavity buildup time κ^{-1} is comparable or larger than the oscillation period Ω_m^{-1} , leading to a viscous radiation pressure force as detailed below. Both in-phase and quadrature components are shown in the parametric plot in figure 6.

2.1.2 Radiation-pressure backaction: static phenomena

So far, only the effect of the mechanical on the optical degree of freedom has been considered. However, the richness of optomechanical phenomena arises only when the *mutual* coupling of optical and mechanical degrees of freedom is taken into account. The physical origin of the “back-action” of light on the

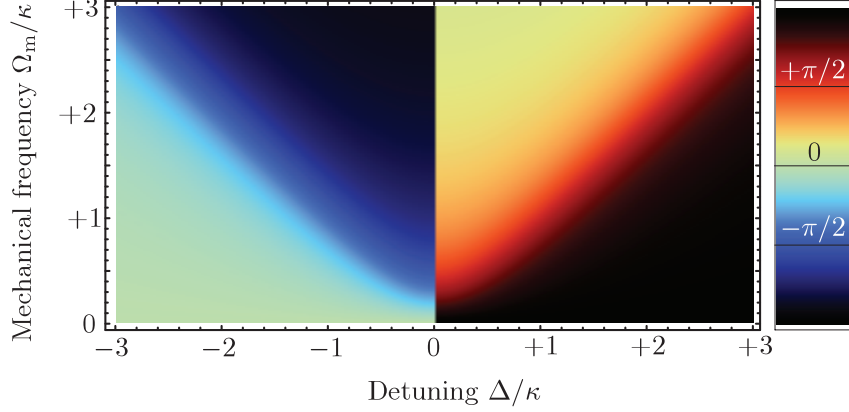


Fig. 5. Phase lag ϕ_{lag} between the oscillation of the mechanical degree of freedom and the stored optical energy (or circulating power) in the cavity, assuming $g_0 < 0$. For $\pm\Delta = \Omega_m \gg \kappa$ the phase lag is exactly $\mp\pi/2$. The phase jump at $\Delta = 0$ is due to a zero crossing of the oscillation amplitude of the stored optical energy.

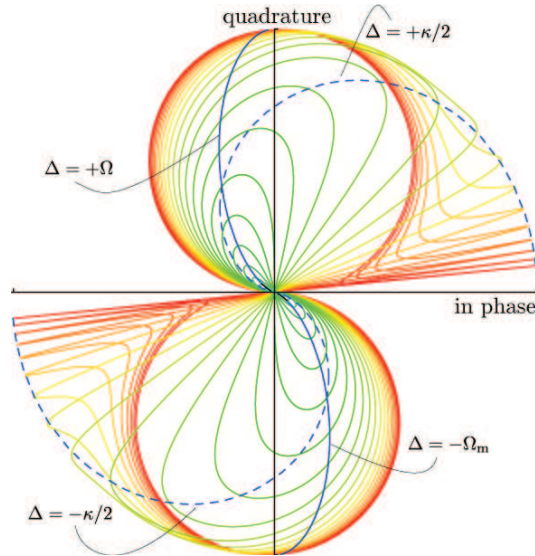


Fig. 6. In-phase and quadrature component of the intracavity energy (or circulating power) modulation when the detuning is varied (colored curves). Different colors represent different choices of the cavity linewidth κ , which was changed from $\Omega_m/10$ (green) to $10\Omega_m$ (red) in logarithmic steps. In the blue curves, a fixed detuning was chosen (as indicated by the labels), and the cavity linewidth was varied from $\Omega_m/10$ to $10\Omega_m$.

movable cavity boundary is due to radiation pressure. In the simple case of a Fabry-Perot cavity, the force arises from the momentum flips of the photons reflected from the movable mirror, and thus

$$F_{\text{rp}}(t) = |a(t)|^2 \frac{c}{2L} 2\hbar k = \frac{|a(t)|^2 \hbar \omega_1}{L} = -\hbar g_0 |a(t)|^2, \quad (11)$$

where $\hbar k$ with $k = \omega_1/c$ is the momentum of the photons.

The relation $F_{\text{rp}}(t) = -\hbar g_0 |a(t)|^2$ is of general validity and also applies to the WGM resonators, as will be derived in section 3.3. If the cavity boundary is free to move, the coupled equations describing the optomechanical system will read (in a frame rotating at the laser frequency)

$$\dot{a}(t) = (i(\Delta - g_0 x(t)) - \kappa/2) a(t) + \sqrt{\eta_c \kappa} s_{\text{in}}(t) \quad (12)$$

$$\ddot{x}(t) + \Gamma_m \dot{x}(t) + \Omega_m^2 x(t) = -\hbar g_0 \frac{|a(t)|^2}{m_{\text{eff}}}, \quad (13)$$

where, for the mechanical oscillation, a resonance frequency Ω_m , viscous damping at a rate Γ_m , and an effective mass m_{eff} (cf. section 3.3) are assumed. For a constant drive amplitude \bar{s}_{in} , these coupled nonlinear equations can be analyzed in a first step by finding stable solutions $a(t) = \bar{a}$, $x(t) = \bar{x}$ in which all time derivatives ($\dot{a}(t)$, $\dot{x}(t)$, $\ddot{x}(t)$) vanish, requiring simultaneously

$$\bar{a} = \frac{1}{-i(\Delta - g_0 \bar{x}) + \kappa/2} \sqrt{\eta_c \kappa} \bar{s}_{\text{in}} \quad \text{and} \quad (14)$$

$$m_{\text{eff}} \Omega_m^2 \bar{x} = -\hbar g_0 |\bar{a}|^2. \quad (15)$$

Equations (14) and (15) can be both understood as functions mapping the displacement \bar{x} to an intracavity photon number $|\bar{a}|^2$, as shown in figure 7. The self-consistent, physically possible solutions are given by the intersections of the two curves.¹ Evidently, the system has at least one solution for arbitrary parameters. For sufficiently high power or finesse, and/or floppy enough mechanical oscillators, two additional solutions are physically possible. The condition for their appearance is given by

$$|\bar{s}_{\text{in}}|^2 \geq \frac{\sqrt{3} \Omega_m^2 m_{\text{eff}} \kappa^2}{9 \eta_c \hbar g_0^2}, \quad (16)$$

which is derived in a straightforward manner from the requirement that the maximum slope $3\sqrt{3}|\bar{s}_{\text{in}}|^2 \eta_c |g_0|/\kappa^2$ of the Lorentzian square modulus of (14) must exceed the slope $m_{\text{eff}} \Omega_m^2/\hbar |g_0|$ corresponding to (15). Above this threshold, the optomechanical system displays a well-known bistable behavior, resulting, for example, in a hysteretic transmission behavior upon the variation of the input power. This effect was observed in a pioneering experiment (Dorsel et al. (1983)) at the Max-Planck-Institute of Quantum Optics (MPQ) as early as 1983 and is referred to as optical bistability. Reports in the microwave domain followed soon thereafter (Gozzini et al. (1985)).

¹ Note that the phase of the complex entity \bar{a} can always be adjusted to fulfill (14), as it does not affect (15).

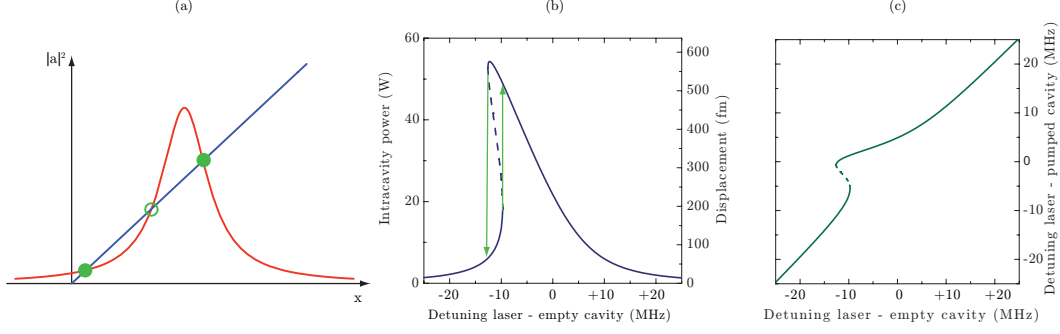


Fig. 7. (a) Graphical representation of the self-consistent solutions of the coupled equations (14) (red) and (15) (blue) for the intracavity photon number $|\bar{a}|^2$ and the radiation-pressure induced displacement \bar{x} of the cavity radius. Intersections of the curves indicate possible stable (full circles) and unstable (empty circles) solutions. (b) Plot of numerical solutions for the power $|\bar{a}|^2/\tau_{\text{rt}}$ circulating in the cavity and the radiation-pressure induced displacement for typical parameters of a silica microtoroidal optomechanical oscillator ($R = 25 \mu\text{m}$, $\kappa = 2\pi 8 \text{ MHz}$, $\Omega_{\text{m}} = 2\pi 50 \text{ MHz}$, $m_{\text{eff}} = 20 \text{ ng}$, $\omega_{\text{c}} = 2\pi 380 \text{ THz}$, $|\bar{s}_{\text{in}}|^2 = 1 \text{ mW}$). The dashed line indicates the unstable solutions. (c) The actual detuning $\Delta - g_0\bar{x}$ as a function of the detuning Δ of the laser from the undriven cavity resonance.

2.1.3 Radiation-pressure backaction: dynamical effects

Quantitatively novel behavior occurs when analyzing the dynamical response of the system around an equilibrium (\bar{a}, \bar{x}) . As first pointed out by Braginsky and co-workers in 1967 (Braginskii and Manukin (1967); Braginsky et al. (2001); Braginsky and Vyatchanin (2002)), the dynamics of fluctuations around the equilibrium not only display new physical effects, but are also of experimental relevance, in particular in the most sensitive gravitational wave interferometers. Keeping with the simple illustrative approach of this section, let us assume the system is in a stable equilibrium if $a = \bar{a}$ and $x = \bar{x}$ and analyze the dynamics of small excursions $\delta a(t)$ and $\delta x(t)$ if a small external force $\delta F(t)$ is applied to the mechanical oscillator. Substituting $a(t) = \bar{a} + \delta a(t)$, $x(t) = \bar{x} + \delta x(t)$ into (12)–(13) and introducing the equilibrium detuning

$$\bar{\Delta} \equiv \omega_1 - (\omega_{\text{c}} + g_0\bar{x}), \quad (17)$$

one finds the linearized equations

$$\dot{\delta a}(t) = (+i\bar{\Delta} - \kappa/2)\delta a(t) - ig_0\bar{a}\delta x(t) \quad (18)$$

$$m_{\text{eff}}\left(\ddot{\delta x}(t) + \Gamma_{\text{m}}\dot{\delta x}(t) + \Omega_{\text{m}}^2\delta x(t)\right) = -\hbar g_0\bar{a}(\delta a(t) + \delta a^*(t)) + \delta F(t), \quad (19)$$

where (14) and (15) were used, and second-order terms $\propto \delta a(t)\delta x(t)$ or $\propto |\delta a(t)|^2$ were dropped, as we assume $|\delta a| \ll |\bar{a}|$. Furthermore, without loss of generality, we have assumed real $\bar{a} = \bar{a}^*$, which can always be attained by adjusting the (physically irrelevant) phase of the incoming driving wave \bar{s}_{in} .

This equation system is most easily solved in the frequency domain, by applying a Fourier transformation to all involved time-dependent variables.² One then obtains

$$-i\Omega\delta a(\Omega) = (+i\bar{\Delta} - \kappa/2)\delta a(\Omega) - ig_0\bar{a}\delta x(\Omega) \quad (20)$$

$$-i\Omega\delta a^*(\Omega) = (-i\bar{\Delta} - \kappa/2)\delta a^*(\Omega) + ig_0\bar{a}\delta x(\Omega) \quad (21)$$

$$m_{\text{eff}}\left(-\Omega^2 - i\Gamma_m\Omega + \Omega_m^2\right)\delta x(\Omega) = -\hbar g_0\bar{a}(\delta a(\Omega) + \delta a^*(\Omega)) + \delta F(\Omega), \quad (22)$$

where $\delta a^*(\Omega) = (\delta a(-\Omega))^*$ was used. Analogous to the previous section which considered a moving boundary, we now find that a non-zero displacement amplitude $\delta x(\Omega)$ at Fourier frequency Ω induces anti-Stokes and Stokes sidebands of amplitudes

$$\delta a(\Omega) = \frac{-ig_0\bar{a}}{-i(\bar{\Delta} + \Omega) + \kappa/2}\delta x(\Omega) \quad (23)$$

$$\delta a^*(\Omega) = \frac{+ig_0\bar{a}}{+i(\bar{\Delta} - \Omega) + \kappa/2}\delta x(\Omega), \quad (24)$$

respectively. As a result, the intracavity energy is modulated, giving rise to an oscillating force of magnitude

$$\begin{aligned} \delta F_{\text{rp}}(\Omega) &= -\hbar g_0\bar{a}(\delta a(\Omega) + \delta a^*(\Omega)) = \\ &= -\hbar g_0^2\bar{a}^2\left(\frac{\bar{\Delta} + \Omega}{(\bar{\Delta} + \Omega)^2 + (\kappa/2)^2} + \frac{\bar{\Delta} - \Omega}{(\bar{\Delta} - \Omega)^2 + (\kappa/2)^2}\right)\delta x(\Omega) \\ &\quad + i\hbar g_0^2\bar{a}^2\left(\frac{\kappa/2}{(\bar{\Delta} + \Omega)^2 + (\kappa/2)^2} - \frac{\kappa/2}{(\bar{\Delta} - \Omega)^2 + (\kappa/2)^2}\right)\delta x(\Omega). \end{aligned} \quad (25)$$

The real and imaginary parts of the radiation pressure force in this representation are identified as being due to the in-phase and quadrature modulation of the circulating power in the cavity. The additional force acting on the mechanical oscillator changes its dynamical behavior, in particular its response to the external perturbation. This effect is known as *dynamical backaction* (Braginskii and Manukin (1967)).

Specifically, substituting (25) back into (22), a modified response of the oscillator to an external force is found,

$$\delta x(\Omega) = \chi_{\text{eff}}(\Omega)\delta F(\Omega) \quad (27)$$

² We choose the convention $f(\Omega) = \int_{-\infty}^{+\infty} f(t)e^{+i\Omega t} dt$.

with the effective susceptibility $\chi_{\text{eff}}(\Omega)$,

$$\chi_{\text{eff}}(\Omega)^{-1} = m_{\text{eff}} \left(-\Omega^2 - i(\Gamma_{\text{m}} + \Gamma_{\text{dba}}(\Omega))\Omega + \left(\Omega_{\text{m}}^2 + \frac{k_{\text{dba}}(\Omega)}{m_{\text{eff}}} \right) \right). \quad (28)$$

The damping and spring constant induced by dynamical backaction are given by

$$\Gamma_{\text{dba}} = \frac{\hbar g_0^2 \bar{a}^2}{m_{\text{eff}} \Omega} \left(\frac{\kappa/2}{(\bar{\Delta} + \Omega)^2 + (\kappa/2)^2} - \frac{\kappa/2}{(\bar{\Delta} - \Omega)^2 + (\kappa/2)^2} \right) \quad (29)$$

$$k_{\text{dba}} = \frac{\hbar g_0^2 \bar{a}^2}{m_{\text{eff}}} \left(\frac{\bar{\Delta} + \Omega}{(\bar{\Delta} + \Omega)^2 + (\kappa/2)^2} + \frac{\bar{\Delta} - \Omega}{(\bar{\Delta} - \Omega)^2 + (\kappa/2)^2} \right). \quad (30)$$

If the induced changes of the mechanical oscillator's dynamics are small, the oscillator still behaves as a damped harmonic oscillator with effective damping and resonance frequency (Kippenberg et al. (2005); Schliesser et al. (2006))

$$\Gamma_{\text{eff}} \approx \Gamma_{\text{m}} + \frac{\hbar g_0^2 \bar{a}^2}{m_{\text{eff}} \Omega_{\text{m}}} \left(\frac{\kappa/2}{(\bar{\Delta} + \Omega_{\text{m}})^2 + (\kappa/2)^2} - \frac{\kappa/2}{(\bar{\Delta} - \Omega_{\text{m}})^2 + (\kappa/2)^2} \right) \quad (31)$$

$$\Omega_{\text{eff}} \approx \Omega_{\text{m}} + \frac{\hbar g_0^2 \bar{a}^2}{2m_{\text{eff}} \Omega_{\text{m}}} \left(\frac{\bar{\Delta} + \Omega_{\text{m}}}{(\bar{\Delta} + \Omega_{\text{m}})^2 + (\kappa/2)^2} + \frac{\bar{\Delta} - \Omega_{\text{m}}}{(\bar{\Delta} - \Omega_{\text{m}})^2 + (\kappa/2)^2} \right). \quad (32)$$

2.2 Formal framework: quantum Langevin equations

A more general formulation of optomechanical interactions than the simple but illustrative considerations in the previous section is possible within the framework of a quantum Langevin approach. This enables the full description of the quantum dynamics of an optomechanical system. In particular, effects related to the quantum nature of light can be treated in an adequate manner.

2.2.1 Hamiltonian of cavity optomechanics

Starting point of the analysis is a Hamiltonian formulation of a generic optomechanical system (Law (1995)). If the mechanical oscillation frequency is much smaller than the free spectral range of the cavity, such that a only a single optical mode has to be considered, the system Hamiltonian can be written

as

$$\hat{H} = \hat{H}_{\text{mech}} + \hat{H}_{\text{opt}} + \hat{H}_{\text{int}} + \hat{H}_{\text{drive}} \quad (33)$$

$$\hat{H}_{\text{mech}} = \frac{\hat{p}^2}{2m_{\text{eff}}} + \frac{1}{2}m_{\text{eff}}\Omega_{\text{m}}^2\hat{x}^2 \quad (34)$$

$$\hat{H}_{\text{opt}} = \hbar\omega_{\text{c}} \left(\hat{a}^\dagger\hat{a} + \frac{1}{2} \right) \quad (35)$$

$$\hat{H}_{\text{int}} = \hbar g_0 \hat{x} \hat{a}^\dagger \hat{a} \quad (36)$$

$$\hat{H}_{\text{drive}} = i\hbar \sqrt{\eta_{\text{c}}\kappa} \left(\bar{s}_{\text{in}}\hat{a}^\dagger e^{-i\omega_{\text{l}}t} - \bar{s}_{\text{in}}^*\hat{a}e^{+i\omega_{\text{l}}t} \right) \quad (37)$$

where \hat{x} and \hat{p} are the mechanical displacement and momentum operators, and \hat{a}^\dagger and \hat{a} are the creation and annihilation operators of the considered optical mode, i. e. $\hat{n} = \hat{a}^\dagger\hat{a}$ is the intracavity photon operator, and correspondingly, the drive amplitude \bar{s}_{in} is now normalized to photon flux at the input of the cavity $|\bar{s}_{\text{in}}|^2 = P_{\text{in}}/\hbar\omega_{\text{l}}$. Evidently, this Hamiltonian reproduces the optical resonance frequency shift upon mechanical displacement, as

$$\hat{H}_{\text{opt}} + \hat{H}_{\text{int}} = \hbar(\omega_{\text{c}} + g_0\hat{x})\hat{a}^\dagger\hat{a}, \quad (38)$$

and simultaneously describes the radiation pressure force, with

$$\hat{F}_{\text{rp}} = -\frac{\partial\hat{H}_{\text{int}}}{\partial\hat{x}} = -\hbar g_0\hat{a}^\dagger\hat{a}. \quad (39)$$

2.2.2 Quantum Langevin equations

From the Hamiltonian, the time evolution of the operators of interest can be derived. In addition to the conservative dynamics described by (33), dissipation of both the optical and mechanical modes, and the corresponding fluctuations are taken into account by the following set of quantum Langevin equations (QLEs) (Giovannetti and Vitali (2001)) (in a frame rotating at ω_{l})

$$\frac{d}{dt}\hat{a}(t) = \left(+i\Delta - \frac{\kappa}{2} \right) \hat{a}(t) - ig_0\hat{x}(t)\hat{a}(t) + \frac{(\bar{s}_{\text{in}} + \delta\hat{s}_{\text{in}}(t))}{\sqrt{\tau_{\text{ex}}}} + \frac{\delta\hat{s}_{\text{vac}}(t)}{\sqrt{\tau_0}} \quad (40)$$

$$\frac{d}{dt}\hat{x}(t) = \frac{\hat{p}(t)}{m_{\text{eff}}} \quad (41)$$

$$\frac{d}{dt}\hat{p}(t) = -m_{\text{eff}}\Omega_{\text{m}}^2\hat{x}(t) - \hbar g_0\hat{a}^\dagger(t)\hat{a}(t) - \Gamma_{\text{m}}\hat{p}(t) + \delta\hat{F}_{\text{th}}(t) \quad (42)$$

where the noise terms $\delta\hat{s}_{\text{in}}$, $\delta\hat{s}_{\text{vac}}$, and $\delta\hat{F}_{\text{th}}$ were introduced. They fulfill the commutation relations (Gardiner and Zoller (2004))

$$[\delta\hat{s}_{\text{in}}(t), \delta\hat{s}_{\text{in}}^\dagger(t')] = [\delta\hat{s}_{\text{vac}}(t), \delta\hat{s}_{\text{vac}}^\dagger(t')] = \delta(t - t') \quad (43)$$

and the quantities

$$\langle \delta \hat{s}_{\text{in}}(t) \delta \hat{s}_{\text{in}}^\dagger(t') \rangle = \langle \delta \hat{s}_{\text{vac}}(t) \delta \hat{s}_{\text{vac}}^\dagger(t') \rangle = \delta(t - t') \quad (44)$$

are the only non-zero correlation functions for the quantum vacuum entering the cavity from its two ports: the one through which it is pumped ($\delta \hat{s}_{\text{in}}$), and the second port ($\delta \hat{s}_{\text{vac}}$) representing all other loss channels. Here, zero thermal excitation of the optical mode has been assumed which is valid in the optical domain. In order to adequately describe the mirror undergoing Brownian motion the correlation function of the mechanical driving term can be shown (Giovannetti and Vitali (2001)) to have the form

$$\langle \delta \hat{F}_{\text{th}}(t) \delta \hat{F}_{\text{th}}(t') \rangle = \hbar m_{\text{eff}} \Gamma_{\text{m}} \int e^{-i\Omega(t-t')} \Omega \left(\coth \left(\frac{\hbar \Omega}{2k_{\text{B}} T} \right) + 1 \right) \frac{d\Omega}{2\pi} \quad (45)$$

As in the previous subsection, the QLEs are simplified in the first place by considering static and the dynamical effects separately. To this end, the unitary transformations $\hat{a}(t) = \bar{a} + \delta \hat{a}(t)$ and $\hat{x}(t) = \bar{x} + \delta \hat{x}(t)$ with $\langle \delta \hat{a}(t) \rangle = \langle \delta \hat{x}(t) \rangle = 0$ yields again the requirements (14)–(15) for the steady state values of intra-cavity field amplitude \bar{a} and displacement \bar{x} .

2.2.3 Dynamics of the fluctuations

Assuming (\bar{a}, \bar{x}) to be known as a stable solution of the system (which can, for example, be tested for using the Routh-Hurwitz criterion, see (Fabre et al. (1994))), the Heisenberg equation of motion for the fluctuations $\delta \hat{a}$, $\delta \hat{a}^\dagger$ and $\delta \hat{x}$ can be derived. Choosing again the phase of the input field \bar{s}_{in} such that \bar{a} is real and positive, and assuming again a strong coherent drive

$$\bar{a} \gg 1 \quad (46)$$

it is possible to derive linearized quantum Langevin equations for the fluctuations by dropping terms $\propto \delta \hat{a} \delta \hat{x}$, $\delta \hat{a}^\dagger \delta \hat{x}$ or $\delta \hat{a}^\dagger \delta \hat{a}$, yielding

$$\frac{d}{dt} \delta \hat{a}(t) = \left(+i\bar{\Delta} - \frac{\kappa}{2} \right) \delta \hat{a}(t) - ig_0 \bar{a} \delta \hat{x}(t) + \frac{\delta \hat{s}_{\text{in}}(t)}{\sqrt{\tau_{\text{ex}}}} + \frac{\delta \hat{s}_{\text{vac}}(t)}{\sqrt{\tau_0}} \quad (47)$$

$$\frac{d}{dt} \delta \hat{a}^\dagger(t) = \left(-i\bar{\Delta} - \frac{\kappa}{2} \right) \delta \hat{a}^\dagger(t) + ig_0 \bar{a} \delta \hat{x}(t) + \frac{\delta \hat{s}_{\text{in}}^\dagger(t)}{\sqrt{\tau_{\text{ex}}}} + \frac{\delta \hat{s}_{\text{vac}}^\dagger(t)}{\sqrt{\tau_0}} \quad (48)$$

$$\frac{d^2}{dt^2} \delta \hat{x}(t) + \Gamma_{\text{m}} \frac{d}{dt} \delta \hat{x}(t) + \Omega_{\text{m}}^2 \delta \hat{x}(t) = -\frac{\hbar g_0}{m_{\text{eff}}} \bar{a} \left(\delta \hat{a}(t) + \delta \hat{a}^\dagger(t) \right) + \frac{\delta \hat{F}_{\text{th}}(t)}{m_{\text{eff}}} \quad (49)$$

where the Hermitian property $\delta\hat{x}(t) = \delta\hat{x}^\dagger(t)$ was used. This set of equations is most easily solved in the Fourier domain:

$$\left(-i(\bar{\Delta} + \Omega) + \kappa/2\right) \delta\hat{a}(\Omega) = -ig_0\bar{a}\delta\hat{x}(\Omega) + \frac{\delta\hat{s}_{\text{in}}(\Omega)}{\sqrt{\tau_{\text{ex}}}} + \frac{\delta\hat{s}_{\text{vac}}(\Omega)}{\sqrt{\tau_0}} \quad (50)$$

$$\left(+i(\bar{\Delta} - \Omega) + \kappa/2\right) \delta\hat{a}^\dagger(\Omega) = +ig_0\bar{a}\delta\hat{x}(\Omega) + \frac{\delta\hat{s}_{\text{in}}^\dagger(\Omega)}{\sqrt{\tau_{\text{ex}}}} + \frac{\delta\hat{s}_{\text{vac}}^\dagger(\Omega)}{\sqrt{\tau_0}} \quad (51)$$

$$m_{\text{eff}}\left(\Omega_{\text{m}}^2 - \Omega^2 - i\Gamma_{\text{m}}\Omega\right) \delta\hat{x}(\Omega) = -\hbar g_0\bar{a}\left(\delta\hat{a}(\Omega) + \delta\hat{a}^\dagger(\Omega)\right) + \delta\hat{F}_{\text{th}}(\Omega). \quad (52)$$

In the frequency domain,

$$\langle\delta\hat{s}_{\text{in}}(\Omega)\delta\hat{s}_{\text{in}}^\dagger[\Omega']\rangle = 2\pi\delta(\Omega + \Omega') \quad (53)$$

$$\langle\delta\hat{s}_{\text{vac}}(\Omega)\delta\hat{s}_{\text{vac}}^\dagger[\Omega']\rangle = 2\pi\delta(\Omega + \Omega') \quad (54)$$

and

$$\langle\delta\hat{F}_{\text{th}}(\Omega)\delta\hat{F}_{\text{th}}[\Omega']\rangle = 2\pi\delta(\Omega + \Omega')\hbar m_{\text{eff}}\Gamma_{\text{m}}\Omega\left(\coth\left(\frac{\hbar\Omega}{2k_{\text{B}}T}\right) + 1\right) \quad (55)$$

are the only non-zero correlation functions. Together with the input-output relations for the fluctuations

$$\delta\hat{s}_{\text{out}}(\Omega) = \delta\hat{s}_{\text{in}}(\Omega) - \sqrt{\eta_c\kappa}\delta\hat{a}(\Omega) \quad (56)$$

$$\delta\hat{s}_{\text{out}}^\dagger(\Omega) = \delta\hat{s}_{\text{in}}^\dagger(\Omega) - \sqrt{\eta_c\kappa}\delta\hat{a}^\dagger(\Omega) \quad (57)$$

these equations constitute the theoretical description of the most important effects in cavity optomechanics.

3 Whispering gallery-mode microresonators as optomechanical systems

Optical microcavities are dielectric structures that confine light to small volumes for extended amounts of time. In 1989 Braginsky and co-workers in Moscow discovered that small dielectric microspheres from glass exhibit optical whispering gallery modes that exhibit giant photon lifetimes, corresponding to ultra high Q-factors exceeding 10^9 (Braginsky et al. (1989); Collot et al. (1993); Vernooy et al. (1998b)). The ultra high Q of microspheres were subsequently investigated for a variety of applications, including laser stabilization (Vassiliev et al. (1998)), cavity Quantum Electrodynamics (cQED) (Vernooy et al. (1998a); Aoki et al. (2006)), narrow linewidth lasers (Sandoghdar et al. (1996)), nonlinear optics at ultra low light powers (Chang and Campillo (1996); Spillane et al. (2002)) and biophysical sensing (Vollmer et al. (2002, 2009)). That optical microresonators also exhibit mechanical modes that are

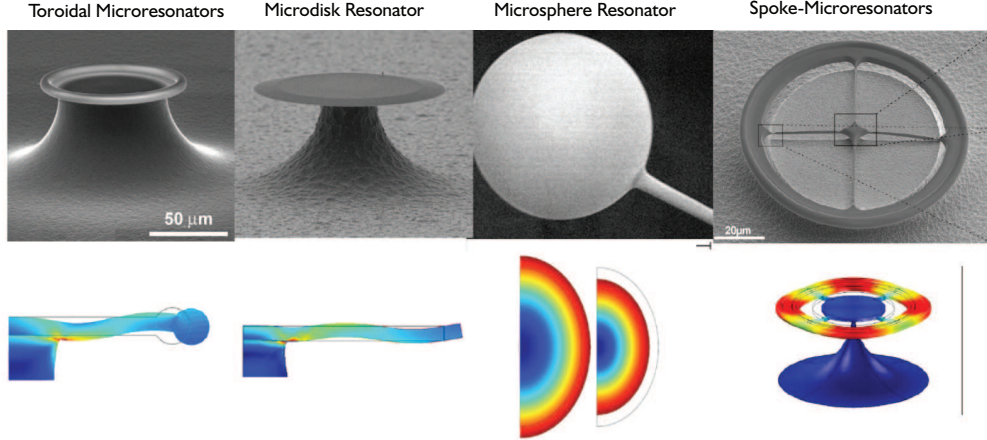


Fig. 8. Optomechanical systems based on WGM optical microresonators. Top row shows scanning electron micrographs of four different systems studied experimentally. The corresponding panels in the bottom row depict the displacement patterns of mechanical modes which couple to the optical modes particularly strongly. The mechanical modes are simulated using the finite-element method (first three panels: 2-dimensional cross-section, last panel: full 3-dimensional simulation).

co-located in the same structure and are coupled via radiation pressure, was only realized in 2005, in toroidal microresonators (Kippenberg et al. (2005); Rokhsari et al. (2005)). It became immediately evident that optomechanical coupling in this manner pertains to virtually any optical microresonator (Kippenberg and Vahala (2007)) and has been demonstrated in a variety of microresonator geometries, including microspheres (Ma et al. (2007)) and microdisks or optimized optomechanical resonators (Schliesser et al. (2008b); Anetsberger et al. (2008)) as shown in figure 8. In this section, prior to discussing the optomechanical phenomena that can occur in optical whispering gallery mode microresonators, we analyze the mechanical modes of WGM microresonators, discuss their mechanical eigenfrequencies and address the question of the sources of mechanical dissipation and other relevant optomechanical properties.

3.1 Optical properties of WGM silica microresonators

An essential precondition to render the weak effects of radiation pressure experimentally accessible is a high optical finesse. In a cavity of finesse \mathcal{F} , the circulating power—and thus also the radiation pressure force—is enhanced by a factor of $\sim \mathcal{F}/\pi$ compared to the launched power. Silica microresonators can achieve finesse on the order of 10^6 , exceeding even the best results achieved with Fabry-Perot cavities for cavity QED (Vernooy et al. (1998b)).

At the same time, in order to reveal dynamical effects of radiation-pressure coupling, the photon storage time should be on the order of—or ideally exceed—the period of the mechanical oscillator coupled to the resonator. In spite of the very short round-trip time of about 1 ps, the storage time can amount to several hundreds of nanoseconds owing to the high finesse. This is about 10 times longer than the oscillation period of the mechanical modes in these structures. To ensure well-controlled optomechanical interaction, the optical mode spectrum must be well understood.

3.2 Optomechanical coupling in silica WGM resonators

3.2.1 Silica microspheres

The mechanical degree(s) of freedom coupled parametrically to the WGMs in silica microresonators are given simply by the intrinsic acoustic modes of the structure. Each of the eigenmodes can be viewed, to a good approximation, as a damped harmonic oscillator, driven by thermal forces. In the following, the nature of these modes, in particular, their eigenfrequency, the damping mechanisms, (effective) mass, mode shapes, and coupling to the optical degrees of freedom will be discussed for two canonical systems; silica microspheres and silica microtoroids.

3.2.2 Acoustic modes in silica microresonators

The deformation induced by mechanical modes is described by a vector field $\vec{u}(\vec{r}, t)$, which denotes the displacement of an (infinitesimally small) cubic volume element at position \vec{r} and time t from its initial position. In an isotropic homogenous medium, to which no external forces are applied, the equation of motion for the displacement field reads (Landau and Lifshitz (1970))

$$\rho \ddot{\vec{u}}(\vec{r}, t) = (\lambda + \mu) \vec{\nabla}(\vec{\nabla} \cdot \vec{u}(\vec{r}, t)) + \mu \vec{\nabla}^2 \vec{u}(\vec{r}, t) \quad (58)$$

where the density ρ and the Lamé constants

$$\lambda = \frac{\sigma E}{(1 + \sigma)(1 - 2\sigma)} \quad (59)$$

$$\mu = \frac{E}{2(1 + \sigma)}, \quad (60)$$

with σ Poisson's ratio and E Young's modulus, characterize the elastic properties of the material.

While for an infinitely extended medium, a continuum of solutions for equa-

tion (58) are obtained, for a finite-size body such as a silica sphere or toroid, the boundary conditions lead to a discrete spectrum of solutions, such that the total displacement $\vec{u}(\vec{r}, t)$ can be decomposed into modes oscillating harmonically at a set of frequencies Ω_n ,

$$\vec{u}(\vec{r}, t) = \sum_n \vec{u}_n(\vec{r}, t) = \sum_n c_n(t) \vec{u}_n^0(\vec{r}) = \sum_n \bar{c}_n \vec{u}_n^0(\vec{r}) e^{-i\Omega_n t}, \quad (61)$$

where $c_n(t)$ is the displacement amplitude of a mode with index n , Ω_n its eigenfrequency and $\vec{u}_n^0(\vec{r})$ is the spatial displacement pattern of the mode, normalized such that

$$\frac{\int_V \vec{u}_n^0(\vec{r}) \vec{u}_{n'}^0(\vec{r}) d^3r}{\int_V d^3r} = \delta_{nn'}. \quad (62)$$

For more sophisticated geometries (e. g. a silica toroid supported by a silicon pillar), it is difficult to obtain analytical solutions for the mode shapes and frequencies.³ In this case, equation (58) with suitable boundary conditions is solved using the finite-element method (FEM). As an illustrative example, and to validate the accuracy of the FEM results, an analytical solution available for spheres is developed in the following (Love (1906); Ma et al. (2007)). In spherical coordinates, equation (58) is solved in a homogeneous medium by functions of the form

$$\vec{u}(\vec{r}, t) = \vec{\nabla} \phi_0(\vec{r}, t) + \vec{\nabla} \times \vec{\Phi}_1(\vec{r}, t) + \vec{\nabla} \times \vec{\nabla} \times \vec{\Phi}_2(\vec{r}, t) \quad (63)$$

derived from a scalar potential ϕ_0 and two vector potentials $\vec{\Phi}_1 = (r\phi_1, 0, 0)$ and $\vec{\Phi}_2 = (r\phi_2, 0, 0)$ with

$$\phi_q(\vec{r}, t) = \sum_{l,m} A_{qnlm} j_l \left(\frac{\Omega_{nlm}}{v_q} r \right) Y_l^m(\theta, \varphi) e^{-i\Omega_{nlm} t} \quad (64)$$

where $q = 0, 1, 2$; j_l denotes the spherical Bessel function, Y_l^m is the spherical harmonic function, $v_0 = \sqrt{(\lambda + 2\mu)/\rho}$ is the longitudinal sound velocity, and $v_1 = v_2 = \sqrt{\mu/\rho}$ is the transverse sound velocity. The acoustic modes are characterized by an angular momentum mode number l ($l = 0, 1, 2, \dots$), an azimuthal mode number m ($-l \leq m \leq l$) and a radial mode number n ($n = 1, 2, \dots$). Here, $n = 1$ corresponds to the surface mode, $n \geq 2$ to inner modes and Ω_{nlm} denotes the frequency of the vibration characterized by the mode numbers (n, l, m) .

We focus now on the fundamental spheroidal mode $(n, l, m) = (1, 0, 0)$, for higher-order modes, cf. (Ma et al. (2007)) and references therein. In particular,

³ For simple cylinders, approximate solutions have been developed (Hutchinson (1979, 1980); Tamura (2009)).

the displacement vector field is purely radial,

$$\vec{u}_{1,0,0}^0(\vec{r}) = A_{0,1,0,0} \frac{\sin(k_{1,0,0}r) - k_{1,0,0}r \cos(k_{1,0,0}r)}{r^2} \vec{e}_r, \quad (65)$$

where $k_{1,0,0} = \Omega_{1,0,0}/v_0$, $A_{0,1,0,0}$ is a normalization constant, and \vec{e}_r the radial unit vector. In the following, we drop the mode index $(1, 0, 0)$ for better legibility, and an index to a vector field now denotes one of its components in a given coordinate system.

To determine the allowed values of k (and therefore Ω), the strain tensor

$$\varepsilon_{ij} = \frac{1}{2} \left(\frac{\partial u_i}{\partial x_j} + \frac{\partial u_j}{\partial x_i} \right) \quad (66)$$

is evaluated in a spherical coordinate system. For the considered mode, all non-diagonal elements vanish, and the diagonal elements read⁴

$$\varepsilon_{rr} = \frac{\partial u_r}{\partial r} = c(t) A \frac{(k^2 r^2 - 2) \sin(kr) + 2kr \cos(kr)}{r^3} \quad (67)$$

$$\varepsilon_{\theta\theta} = \frac{u_r}{r} = c(t) A \frac{\sin(kr) - kr \cos(kr)}{r^3} \quad (68)$$

$$\varepsilon_{\varphi\varphi} = \frac{u_r}{r} = c(t) A \frac{\sin(kr) - kr \cos(kr)}{r^3}, \quad (69)$$

where $c(t)$ is the excitation amplitude of the mode. The stress is related to the strain by Hooke's law, which in a lossless isotropic medium is given by

$$\sigma_{ij} = 2\mu\varepsilon_{ij} + \lambda\delta_{ij} \sum_k \varepsilon_{kk} \quad (70)$$

rendering in this case the stress tensor σ_{ij} diagonal as well,

$$\sigma_{rr} = c(t) A \frac{((\lambda + 2\mu)k^2 r^2 - 4\mu) \sin(kr) + 4\mu kr \cos(kr)}{r^3} \quad (71)$$

$$\sigma_{\theta\theta} = c(t) A \frac{(\lambda k^2 r^2 + 2\mu) \sin(kr) - 2\mu kr \cos(kr)}{r^3} \quad (72)$$

$$\sigma_{\varphi\varphi} = c(t) A \frac{(\lambda k^2 r^2 + 2\mu) \sin(kr) - 2\mu kr \cos(kr)}{r^3}. \quad (73)$$

Applying the boundary conditions for a freely oscillating sphere of radius R leads to the requirement that the stress is zero at its boundary ($r = R$),

⁴ For the definitions of the strain tensor in spherical coordinates see (Landau and Lifshitz (1970)).

leading to the characteristic equation

$$\left(1 - \frac{1}{4} \frac{v_0^2}{v_1^2} k^2 R^2\right) \frac{\tan(kR)}{kR} - 1 = 0. \quad (74)$$

For the parameters of fused silica, this equation is solved for $kR \approx 2.4005 \dots$ or

$$\frac{\Omega_m}{2\pi} \approx \frac{2280 \text{ m/s}}{R}, \quad (75)$$

corresponding to a resonance frequency of 91.2 MHz for a 50- μm diameter sphere. Finite element modeling yields the same result within less than 1%, testifying to the integrity of our employed numerical simulation.

Another interesting physical entity is the potential energy stored in the deformation. It given by

$$U = \sum_{i,j} \int_V \frac{1}{2} \sigma_{ij} \varepsilon_{ij} d^3r. \quad (76)$$

The diagonal form of strain and stress tensors for a sphere again facilitates the analytical evaluation of this integral simple yielding

$$U \approx 8.69 \cdot 10^{11} \frac{\text{J}}{\text{m}^3} \cdot R \cdot x^2 \quad (77)$$

where $x = \vec{u}(R, \theta, \varphi) \cdot \vec{e}_r = c(t) A(\sin(kR) - kR \cos(kR))/R^2$ is the radial displacement of the boundary, with $A \approx 0.427R^2$ for silica. Figure 9 shows displacement, strain, stress and strain energy density of a silica sphere when the fundamental mode is excited. Results from analytic calculations and the FEM agree very well.

Figure 10 compares experimentally measured resonance frequencies of several silica microspheres with diameters between 30 and 100 μm with analytical calculations. Again, very good agreement is obtained.

3.2.3 Silica microtoroids

Toroidal silica resonators, attached a silicon pillar, have fewer symmetries than spheres. This structure must be parameterized by several parameters, at least by the major and minor radii of the silica torus, the radius of the silicon pillar, the thickness of the silica disk, and the offset of the symmetry planes of the disk and torus along the z -axis (Kippenberg et al. (2005)). The shape of the silicon pillar is assumed to be rotationally symmetric, and to constitute a quarter circle in the r - z -plane. The radius of this circular arch is another degree of freedom, but is usually assumed to be similar to the difference of toroid and pillar radii (figure 11) due to the isotropic nature of the silicon

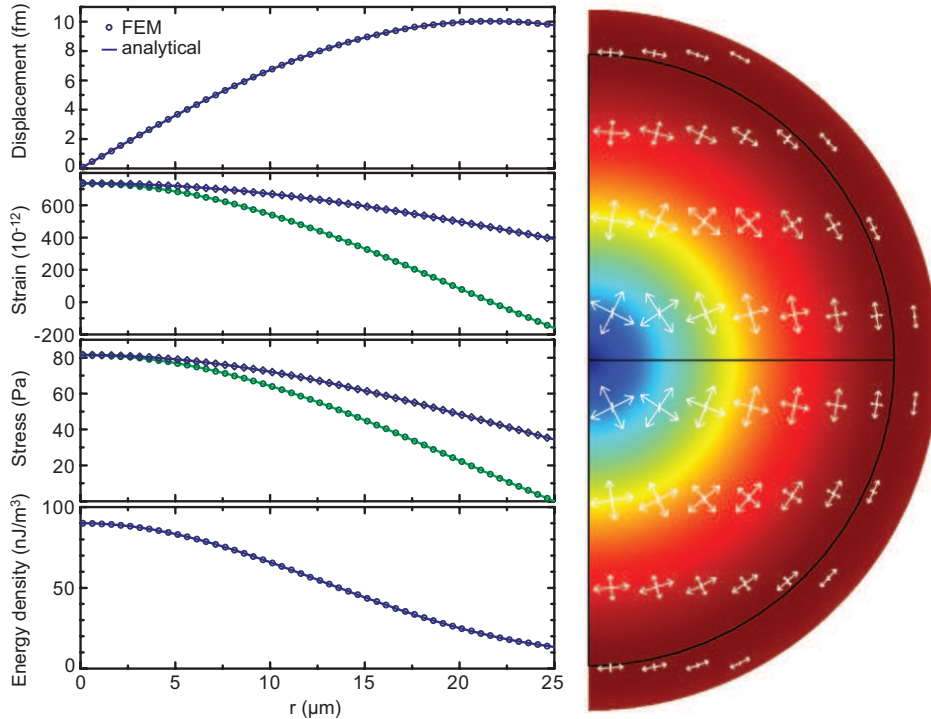


Fig. 9. The $(n, l, m) = (1, 0, 0)$ mode of a silica sphere. Left panels show (from top to bottom) the radial displacement $\vec{u}(r, \theta, \varphi) \cdot \vec{e}_r$, the strains ε_{rr} (green) and $\varepsilon_{\theta\theta} = \varepsilon_{\varphi\varphi}$ (blue), stresses σ_{rr} (green) and $\sigma_{\theta\theta} = \sigma_{\varphi\varphi}$ (blue), and the strain energy density $\frac{1}{2} \sum_{ij} \sigma_{ij} \varepsilon_{ij}$. Symbols are results of finite-element modeling and lines are derived from the analytical calculations, showing excellent agreement. The given magnitudes correspond to a $50 \mu\text{m}$ -diameter sphere containing a total strain energy of $k_B(300 \text{ K})/2$. The right panel shows the exaggerated displacement profile (original sphere outlined in black), and magnitude (color coded) as well as the principal stresses (indicated by arrow lengths).

etch.

The complex boundary conditions (all surfaces free, except for the bottom of the silicon pillar) render an analytical solution prohibitively difficult. We therefore use a commercial finite-element software to solve equation (58) on a discrete mesh consisting typically of more than 10,000 nodes which are automatically distributed in the simulation volume. Simulations can be run both assuming rotational symmetry for the modes, and in full three dimensions. Figure 12 shows the obtained displacement patterns for the 19 lowest-frequency modes of a toroid of major radius $23.0 \mu\text{m}$, pillar radius $13.23 \mu\text{m}$, minor radius $2.63 \mu\text{m}$, disk thickness $2 \mu\text{m}$ and no offset, in a three-dimensional simulation. As shown in figure 13, the simulation can reproduce the frequencies measured on a real toroid to a very high accuracy (Schliesser et al. (2008a)). Indeed, the average deviation between measured and simulated frequency is, on average, below 2%. This emphasizes the reliability of the FEM. Note also that probing of the modal displacement patterns using a scanning probe technique

Fig. 10. Resonance frequencies of silica microspheres for the $(n, l) = (1, 0)$ (upper branch) and $(n, l) = (1, 2)$ (lower branch) spheroidal resonance modes (Ma et al. (2007)). Curves are expected resonance locations for free boundary conditions, following an inverse dependence on the sphere radius with $\Omega_m/2\pi \approx 2280 \text{ m/s}/R$ for the $l = 0$ and $\Omega_m/2\pi \approx 1580 \text{ m/s}/R$ for the $l = 2$ mode. Symbols represent measured spheres. The panels on the right show the corresponding displacement patterns as obtained from the FEM. The left and right halves of the sphere show the displacement of the volume elements at two different times separated by half the oscillation period.

has confirmed the shape expected from simulations in an earlier experiment (Kippenberg et al. (2006)).

Various mode families with qualitatively different displacement patterns are recognized. Some modes involve mainly motion of the silicon pillar (number 6, 13 and 18 in figure 12) and therefore couple only negligibly to the optical mode, rendering it irrelevant for the purpose of cavity optomechanics. A torsional mode (number 4) is also observed, but it couples only weakly to the optical

modes (cf. section 3.3). Modes number 1, 3, 5, 7, 11 and 16 are characterized by an n -fold symmetry under rotation by an angle π/n , where $n = 1 \dots 6$ in this case. These modes, which we refer to as “crown” modes, involve mainly sinusoidal oscillation of the toroid in the z -direction. They typically follow a quadratic dispersion relation, that is, their eigenfrequency is proportional to the square of the number of nodes along the circumference (Schliesser et al. (2008a)). Modes of this family are doubly frequency degenerate as for each mode in this family there exists a second mode in which the positions of nodes and antinodes are swapped. In measurements on real toroids, this degeneracy is often lifted due to small deviations from perfect rotational symmetry of the structure, leading to a splitting into a resonance doublet.

In the context of cavity optomechanics, the most interesting modes coupling strongly to the optical field are the ones with (nearly) radially symmetric

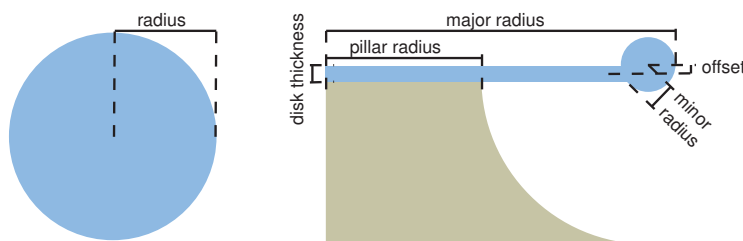


Fig. 11. Geometric parameters required to describe a sphere (right) and a toroidal WGM resonator, where silica is shown in blue and silicon in grey.

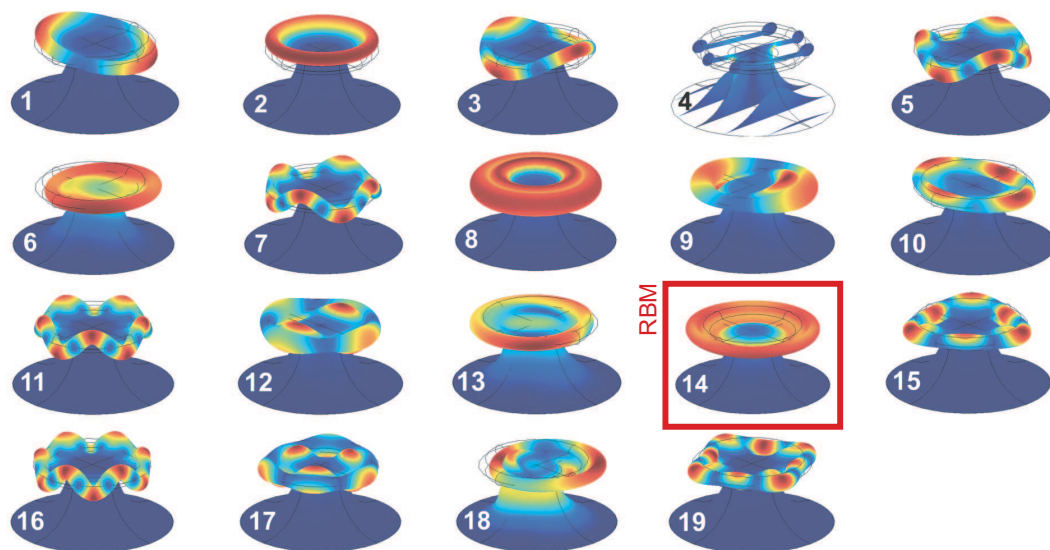


Fig. 12. Displacement patterns of the 19 lowest-frequency modes (see text) of a toroidal microresonator as calculated using the FEM, indicated both as the deformed shape and in the color code (increasing displacement from dark blue to dark red). Mode number 4 involves mainly torsional motion, which is illustrated by plotting the displacement of originally parallel slices through the structure. Figure from ref. (Schliesser et al. (2008a)).

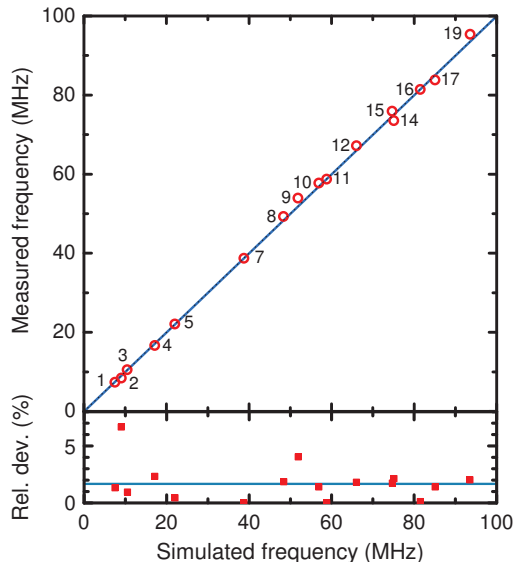


Fig. 13. Comparison of simulated and measured frequencies of a toroidal silica microresonator. The relative deviation is below 2% on average. Figure from ref. (Schliesser et al. (2008a)).

displacement patterns (number 2, 8, and 14). One usually distinguishes flexural modes, in which the displacement is mainly along the z -axis (number 2 and 8), and the radial modes involving mainly radial displacement. Strongest coupling is caused by the fundamental radial mode, which we refer to as the radial breathing mode (RBM) with number 14 in figure 12. The RBM in the measured toroid has a frequency of 75.1 MHz, and usually lies between 30 and 120 MHz for typical toroidal geometries.

3.2.4 Mechanical dissipation

Another very important property of the RBM is its damping rate. As in the case of the optical modes, different dissipation mechanisms lead to a release of mechanical energy stored in the RBM to other degrees of freedom. The mechanical damping rate Γ_m quantifies the rate at which this takes place, and is again expressed in terms of a quality factor

$$Q_m = \Omega_m / \Gamma_m. \quad (78)$$

The different damping mechanisms all contribute to the total damping, and the resulting quality factor can be written

$$Q_m^{-1} = Q_{\text{gas}}^{-1} + Q_{\text{clamp}}^{-1} + Q_{\text{TLS}}^{-1} + Q_{\text{other}}^{-1} \quad (79)$$

with contributions by the surrounding gas (Q_{gas}^{-1}), by clamping losses (Q_{clamp}^{-1}), by two-level systems (Q_{TLS}^{-1}) and by other damping mechanisms (Q_{other}^{-1}).

In the initial optomechanical experiments with silica microtoroids the mechanical quality factors reached values of 3,000 (Kippenberg et al. (2005); Schliesser et al. (2006)). By replacing the surrounding nitrogen gas with helium (which has lower viscosity η and molecular mass M), the quality factors rose beyond 5,000, clearly indicating that the losses were dominated by gas damping. From the known drag on a sphere oscillating in a viscous fluid (Landau and Lifshitz (1987)) one can expect a scaling $Q_{\text{gas}} \propto (\eta p M)^{-1/2}$ in this regime. Reducing the pressure p of the ambient gas should therefore raise Q_{gas} . Indeed, at pressures above 10 mbar the quality factor was observed to increase as $Q_{\text{gas}} \propto p^{-1/2}$, indicative of the viscous regime, while for lower pressures, in the molecular regime, $Q_{\text{gas}} \propto p^{-1}$ was observed (Anetsberger et al. (2008)). At pressures below 1 mbar, gas damping becomes irrelevant ($Q_{\text{gas}} \gg Q_{\text{m}}$) and the quality factor is observed to converge towards a saturation value at lower pressures. Among different toroids, there are significant variations in the range between 1,000 and 30,000 for this value. This is due to clamping losses, which strongly depend on the geometry of the sample as is detailed below.

To study this effect of clamping losses more systematically, a toroidal resonator was underetched in several steps, to reduce the radius of the silicon pillar, and thereby increase the relative undercut, which we define as

$$\text{relative undercut} = 1 - \frac{\text{silicon pillar radius}}{\text{silica toroid major radius}}. \quad (80)$$

The quality factors and resonance frequencies of the RBM of six toroidal resonators on the chip were measured for each etching step (figure 14). Strikingly, while the resonance frequency reduces monotonically, the quality factors vary in a non-monotonic manner, with a distinct minimum for an undercut of approximately 0.7. This behavior was highly reproducible and observed for different independent samples.

A series of simulations with increasing undercut reveals that the resonance frequencies of the RBM and a radially symmetric flexural mode are crossing each other for this undercut, as they have a different undercut dependence. However, the actual resonance frequencies of the structure exhibit an avoided crossing. At the same time, the modal shapes of the RBM and flexural mode hybridize in the crossing region. These two facts imply a normal mode coupling between the RBM and the flexural mode.

To corroborate this conjecture experimentally, the undercut in a different sample was again systematically increased. For each etching step, a highly sensitive measurement technique (polarization spectroscopy, cf. section 4) allowed the determination of the frequencies of both the RBM (Ω_{R}) and also the adjacent flexural (Ω_{F}) mode. Indeed, the measured frequencies and quality factors can be simultaneously reproduced using a simple model of two coupled harmonic oscillators, the intrinsic frequencies Ω_{R} and Ω_{F} and quality factors Q_{R} and

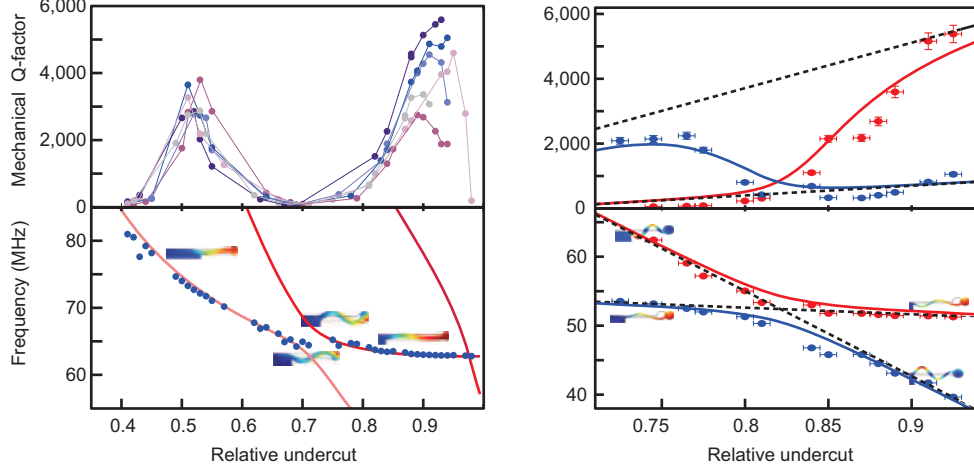


Fig. 14. Normal mode coupling between the RBM and a flexural mode. Left panels: Measured quality factors of the RBM of six samples on the same chip as a function of relative undercut, and the resonance frequencies of one of the samples (dots). Lines in the lower panel are results of simulations, and show not only the frequency of the RBM, but also of radially symmetric flexural modes. In the region where the frequencies are similar, for a relative undercut of ~ 0.7 , the quality factors are strongly reduced. Right panels: Evidence of normal mode coupling between the RBM and a flexural mode in another sample. The frequencies Ω_{\pm} and quality factors Q_{\pm} of the experimentally observed modes (dots) can be reproduced using a model of two coupled harmonic oscillators (red and blue lines). The frequencies and quality factors of the uncoupled modes, corresponding to a pure RBM and flexural mode are assumed to depend only linearly on the relative undercut (dashed lines). Adapted from (Anetsberger et al. (2008)).

Q_F of which are linearly dependent on the undercut. The frequencies Ω_{\pm} and quality factors Q_{\pm} of the new eigenmodes are given by (Anetsberger et al. (2008))

$$\Omega_{\pm} + \frac{i}{2} \frac{\Omega_{\pm}}{Q_{\pm}} = \frac{1}{2} (\Omega_R + \Omega_F) + \frac{i}{4} \left(\frac{\Omega_R}{Q_R} + \frac{\Omega_F}{Q_F} \right) \pm \sqrt{\left(\frac{1}{2} (\Omega_R + \Omega_F) + \frac{i}{4} \left(\frac{\Omega_R}{Q_R} - \frac{\Omega_F}{Q_F} \right) \right)^2 + \frac{g_{\text{im}}^4}{4\Omega_R\Omega_F}} \quad (81)$$

where the intermode coupling g_{im} is an adjustable parameter (figure 14). The data in figure 14 can be fit using $g_{\text{im}}/2\pi = 14$ MHz. This rather strong coupling is attributed to the asymmetry of the structure in the axial direction due to both the offset of the toroid from the disk (Kippenberg et al. (2005)), and the fact that the silicon pillar supports the disk only from below.

Summarizing the previous observations, we conclude that the admixture of a flexural displacement pattern to the RBM reduces the quality factor of the latter. This can be explained by noting that the flexural modes induce axial displacement also in the region where the silica disk is supported by

the silicon pillar. The periodic oscillation in axial direction launches acoustic waves into the pillar, through which the energy of the mode is dissipated, thereby deteriorating the quality factor.

This qualitative understanding is quantitatively supported by an analytical model (Anetsberger et al. (2008)), in which the acoustic energy loss is estimated as the power radiated by a membrane of area A_p (area of the silicon pillar) oscillating with an axial displacement $\Delta z(\vec{r})$ at frequency Ω_m

$$P_{\text{mech}} = v\rho\Omega_m^2 \int_{A_p} |\Delta z(\vec{r})|^2 d^2r, \quad (82)$$

where v is the sound velocity and ρ the density. For geometry parameters close to the modal crossing, it was indeed found experimentally that

$$Q_{\text{clamp}} \propto \frac{\Omega_m E_{\text{mech}}}{P_{\text{mech}}}, \quad (83)$$

where E_{mech} is the total mechanical energy of the mode. Advantageously, both E_{mech} and P_{mech} can be simulated using FEM (Anetsberger et al. (2008)). As an aside we note that an expression similar to (82) and (83) was obtained in a rigorous theoretical analysis based on a phonon tunneling approach (Wilson-Rae (2008)). To reduce P_{mech} , two strategies are immediately evident: Either the clamping area A_p is minimized, or the axial displacement $\Delta z(\vec{r})$ in this region is reduced. Minimizing the clamping area is possible, for example, by fabricating toroids with a very strong undercut, as shown in figure 15, in which the silica disk is supported by a “needle pillar” of sub-micrometric diameter (Schliesser et al. (2008b)).

Alternatively, by introducing spokes into the silica disk, it was possible to strongly reduce the coupling of the radial motion to an axial displacement in the clamping region (Anetsberger et al. (2008)). Both presented approaches yield good results with quality factors exceeding 30,000 at frequencies around 40 MHz (Schliesser et al. (2008b); Anetsberger et al. (2008)).

In figure 16 we show an overview of mechanical quality factors achieved in typical samples with different major diameters, all strongly undercut ($> 90\%$) and measured in vacuum. A clear trend to higher quality factors for larger cavity sizes (and therefore lower frequencies) is observed. The scatter in the data of neighboring toroids (with very similar reflow preform and final pillar shapes) indicates that clamping losses depend sensitively on geometry parameters. Finally, we note that we have consistently observed higher quality factors in disks than in toroids. This is attributed to a reduced offset (figure 11) of the oscillating mass, which, in toroids, mediates the coupling of the RBM to radially symmetric flexural modes with strong dissipation to the pillar.

The highest quality factors which were experimentally achieved at room tem-

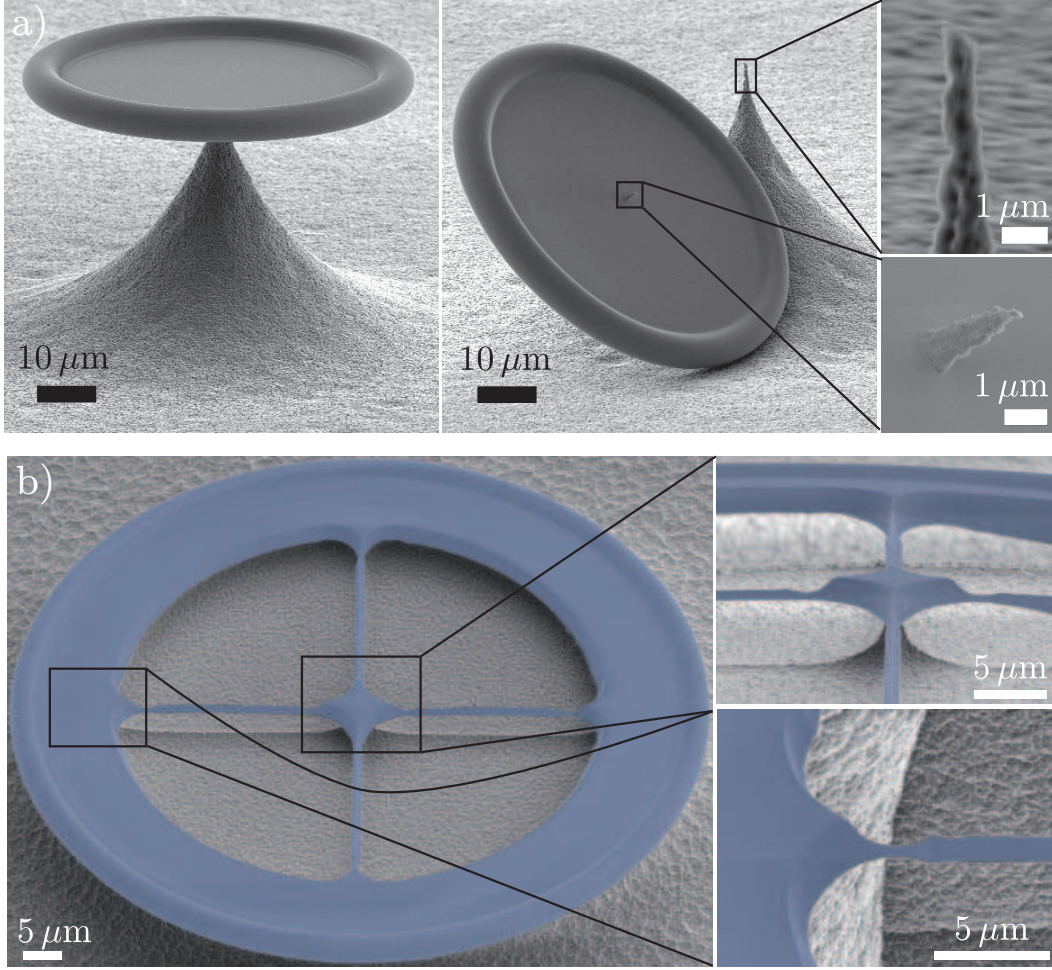


Fig. 15. Silica toroidal resonators with ultralow mechanical damping. a) Reduced clamping loss by supporting the silica disk with a “needle” pillar. The central and right panels show the tip of an intentionally broken pillar, which has a sub-micron diameter. A quality factor of 30,000 is reached with such structures for a 40 MHz-RBM (Schliesser et al. (2008b)). b) Reducing clamping loss by engineering the axial displacement in the clamping region using a “spokes” design. Such resonators achieved mechanical quality factors up to 32,000 at 38 MHz, and 50,000 at 24 MHz at room temperature (Anetsberger et al. (2008)) limited by TLS losses.

perature are $Q_m \sim 50,000$ above 20 MHz. For these structures however, simulations clearly indicate $Q_{\text{clamp}} \gg Q_m$ according to equation (83), indicating that a different dissipation mechanism must now be dominant. A strong temperature dependence of the quality factor (allowing for values up to 80,000 at 110°C) suggests a temperature-dependent dissipation mechanism (Anetsberger et al. (2008)).

Indeed, the intrinsic damping of acoustic excitations in glass is known to follow a universal behavior observed in many amorphous solids (Pohl et al. (2002)). This effect is attributed to the coupling of strain fields to structural defects in the material. While the microscopic nature of these defects is not precisely

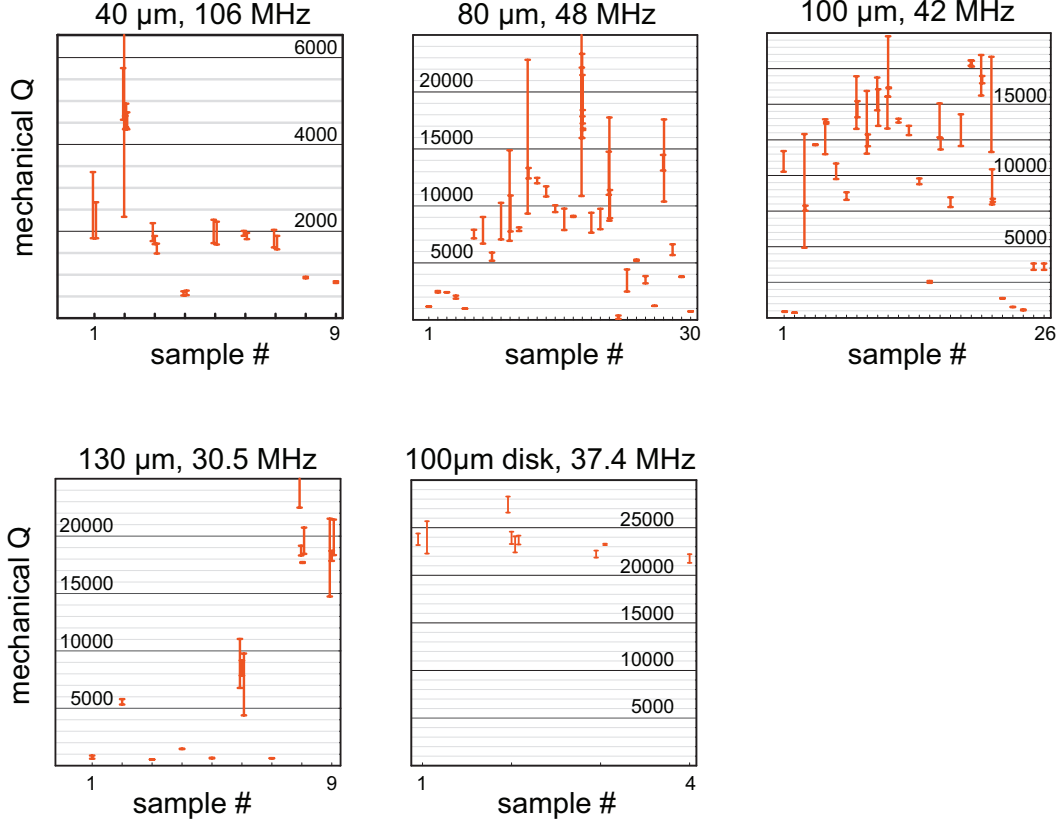


Fig. 16. Overview of mechanical quality factors of the RBM measured in typical toroids. Major diameters of the pre-reflow disk and the approximate resonance frequency are indicated in the figure captions. Each bracket indicates the span within which the mechanical quality factor was found in a pair of measurements, in which the probing laser was red and blue detuned (dynamical backaction modifies the measured effective mechanical quality factor in opposite directions in the two cases). Groups of brackets belong to the same toroid. The last panel shows measurements taken on silica disks prior to the reflow.

known, it can be successfully modeled by a distribution of effective two-level systems (TLS) with two stable equilibria, represented by a particle in an asymmetric double-well potential (Jäckle (1972)). These potentials are characterized by the energy asymmetry Δ of the ground states in both potentials (the two levels involved), and the height V of the energy barrier separating the two wells as shown in figure 17. Oscillating strain fields associated with an acoustic excitation modulate the energy asymmetry Δ between the two potential minima, and thereby couple to the TLS.

To a very good approximation, the resulting Debye relaxation of acoustic excitations leads to a quality factor given by (Vacher et al. (2005))

$$Q_{\text{TLS}}^{-1} = \frac{\gamma^2}{\rho v^2 k_B T} \int_{-\infty}^{+\infty} \int_0^{+\infty} P(\Delta, V) \operatorname{sech}^2\left(\frac{\Delta}{2k_B T}\right) \frac{\Omega \tau}{1 + \Omega^2 \tau^2} dV d\Delta, \quad (84)$$

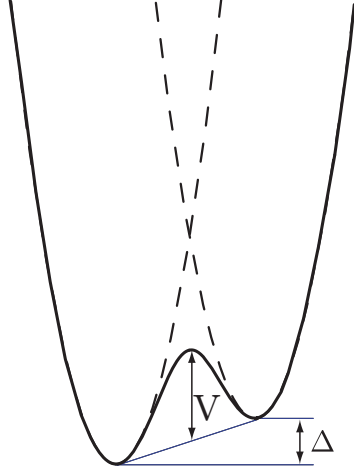


Fig. 17. Double-well potential used to model the structural defects in glass. The two individual wells (dashed lines) are usually assumed to be identical, but to have a ground-state energy that differs by an energy asymmetry Δ . The two stable equilibria are separated by a barrier of height V .

where $\gamma = \frac{1}{2}\partial\Delta/\partial\varepsilon$ is the change of the potential asymmetry as a function of strain ε , ρ is the density, v sound velocity, and $P(\Delta, V)$ is the distribution of TLS in the energy parameters Δ and V in the sense that $P(\Delta, V)dVd\Delta$ is a volume density of defects.

At room temperature, the relaxation between the two stable states is dominated by thermally activated processes. The relaxation time is thus given by an Arrhenius-type law

$$\tau^{-1} = \tau_0^{-1} e^{-V/k_B T} \cosh\left(\frac{\Delta}{2k_B T}\right). \quad (85)$$

Following the arguments given in reference (Vacher et al. (2005)), a sensible choice of the distribution function $P(\Delta, V)$ yields eventually a quality factor of

$$Q_{\text{TLS}}^{-1} = C \cdot \text{erf}\left(\frac{\sqrt{2}k_B T}{\Delta_c}\right) \frac{1}{k_B T} \int_0^\infty \left(\frac{V}{V_0}\right)^{-\zeta} e^{-V^2/2V_0^2} \frac{\Omega\tau_0 e^{V/k_B T}}{1 + \Omega^2\tau_0^2 e^{2V/k_B T}} dV \quad (86)$$

reproducing the experimental data over four orders of magnitude in frequency (11 kHz . . . 200 MHz) and two orders of magnitude in temperature (from a few Kelvin to above room temperature) for the parameters $V_0 = (667 \pm 21) \text{ K} \cdot k_B$, $\zeta = 0.28 \pm 0.03$, $\log_{10}(\tau_0/\text{s}) = -12.2 \pm 0.18$ and $V_0/\Delta_c = 7.7 \pm 0.7$.

While usually measured as the attenuation of large-amplitude acoustic waves in bulk material, the very same temperature dependence of the quality factor was found for the RBM of spokes toroids with sufficiently low clamping losses (Arcizet et al. (2009)). Figure 18 shows the measured quality factor of the RBMs of two samples at frequencies of 36 and 63 MHz. Simultaneously with

the damping, relaxation of the TLS also leads to a change in the sound velocity, giving rise to a frequency shift of the mechanical modes (Vacher et al. (2005)),

$$\left(\frac{\delta\Omega_m}{\Omega_m}\right) = -\frac{C}{2} \cdot \operatorname{erf}\left(\frac{\sqrt{2}k_B T}{\Delta_c}\right) \frac{1}{k_B T} \int_0^\infty \left(\frac{V}{V_0}\right)^{-\zeta} e^{-V^2/2V_0^2} \frac{1}{1 + \Omega^2\tau_0^2 e^{2V/k_B T}} dV, \quad (87)$$

which is also shown in figure 18. At temperatures above 10 K, the damping can be accurately described by equation (86), with a peak damping at about 50 K leading to a minimum quality factor of $Q_{\text{TLS}} \approx 500$.

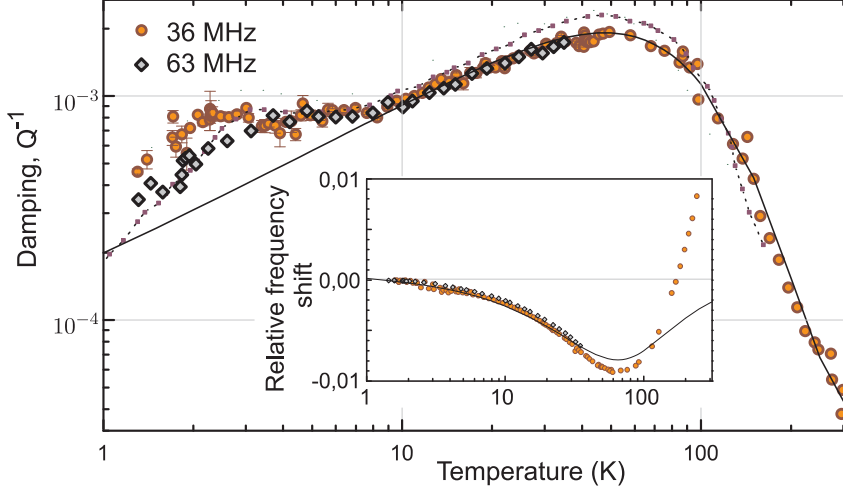


Fig. 18. Quality factor of the RBMs of two samples which are dominated by the damping due to coupling to structural defects in glass. Solid line is a fit using equation (86), and the dashed lines are experimental data from an acoustic wave attenuation experiment at 40 MHz (Bartell and Hunklinger (1982)). The inset shows the relative frequency shift of the RBM induced by the relaxation of TLS. From ref. (Arcizet et al. (2009)).

Below 10 K, the relaxation is dominated by tunneling processes between the two equilibria (Jäckle (1972); Tielbürger et al. (1992)), instead of the thermally-activated relaxation. The tunneling relaxation is responsible both for the low-temperature plateau ($Q_m \approx 1200$ at 5 K) and the roll-off at very low temperatures with $Q_{\text{TLS}}^{-1} \propto T^3/\Omega$. For completeness, we note that apart from damping via relaxation, at sufficiently low temperatures, direct absorption of acoustic waves by the TLS also leads to damping, which saturates at high enough amplitudes (Jäckle (1972); Hunklinger et al. (1973)).

Other damping mechanisms, as described by Q_{other} , include thermoelastic damping (Zener (1937, 1938)), damping by anharmonicity (Vacher et al. (2005)), and surface effects (Ekinici and Roukes (2005)). For silica microtoroids or spheres, these effects are individually estimated to lead to limiting quality factors on the order of 10^5 or more. In particular when operating the resonators at cryogenic temperatures—as required for advanced experiments in cavity optomechanics—these damping mechanisms can be safely neglected

compared with the damping due to TLS.

3.3 Optomechanical coupling

In order to describe optomechanical coupling in microspheres and microtoroids introduced in the previous section, it is advantageous to map the mechanical modes of interest to an effective one-dimensional mechanical oscillator, described by a displacement x , which parametrically modulates the optical resonance frequency through a non-zero $g_0 = d\omega_c/dx$. For optomechanical devices which host optical and mechanical modes with complex three-dimensional mode distributions such as silica microtoroidal resonators (figure 19), this mapping can be non-trivial.

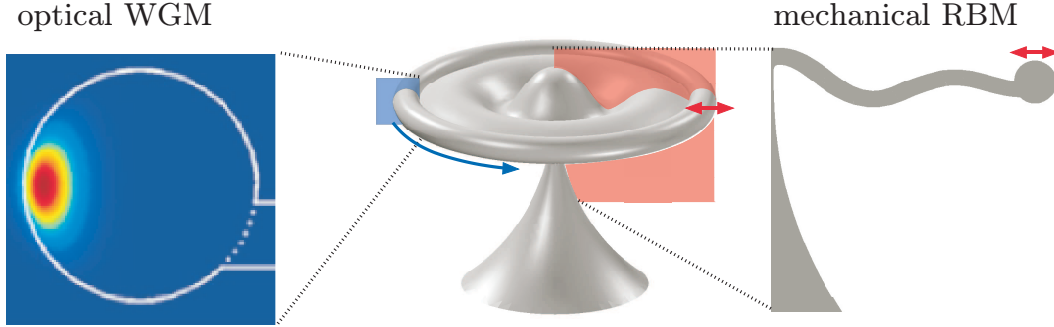


Fig. 19. Mode shapes of optical and mechanical modes in a silica microtoroidal resonator (FEM simulations), which have to be taken into account to quantify the strength of optomechanical interaction.

3.3.1 Mapping to a scalar displacement

To formally describe this mapping, a weighting function $\vec{w}(\vec{r})$ is introduced, mapping the displacement field $u(\vec{r}, t)$ to a scalar displacement x according to

$$x(t) = \int_V \vec{w}(\vec{r}) \cdot \vec{u}(\vec{r}, t) d^3r = \sum_n c_n(t) \int_V \vec{w}(\vec{r}) \cdot \vec{u}_n^0(\vec{r}) d^3r \quad (88)$$

$$\equiv \sum_n c_n(t) \langle \vec{w}, \vec{u}_n^0 \rangle, \quad (89)$$

where the decomposition of the displacement pattern \vec{u} as presented in eq. (61) is used. For each mechanical mode, the overlap integral $\langle \vec{w}, \vec{u}_n^0 \rangle$ determines the relative strength of the transduction of the n -th mode amplitude $c_n(t)$ into the optically sampled displacement $x(t)$. The *global* normalization of $\vec{w}(\vec{r})$ is, in principle, arbitrary, as it can be compensated by an adequate choice of $g_0 = d\omega_c/dx$. For example, it can be chosen such that the displacement of a particular part of one mode's displacement pattern (such as the antinode of a beam's fundamental mode) directly corresponds to x (Eichenfield et al. (2009b)).

For the most generic optomechanical systems, there are other obvious choices.

For example, for a Fabry-Perot cavity, the normalization is chosen such that x corresponds to the center-of-mass mirror movement if it was displaced as a whole. Thus, if the laser spot on a mirror at $z = z_0$, which contains the mechanical modes, is given by a rotationally symmetric Gaussian with a waist of w_0 , the weighting function reads (Pinard et al. (1999); Braginsky et al. (2001))

$$\vec{w}(\vec{r}) = \frac{2}{\pi w_0^2} e^{-2r^2/w_0^2} \delta(z - z_0) \vec{e}_z. \quad (90)$$

With this weighting function, the physically correct frequency shift is obtained using the coupling constant $g_0 = -\omega_c/L$, where L is the total length of the cavity.

In the case of silica WGM resonators, with their three-dimensional distributions of optical and mechanical fields, the calculation of the effective displacement is more difficult. A sensible approximation may be obtained by considering the mechanical displacement as a perturbation, which does not modify the optical fields, but only displaces polarizable matter within the optical field distribution. The resulting relative frequency shift equals the relative change in the electromagnetic energy stored in the mode, as the number of stored photons, each of energy $\hbar\omega_c$, is conserved in the cavity (Arnold et al. (2003)). The resulting frequency shift is

$$\frac{\delta\omega_c}{\omega_c} = \frac{\delta E_{\text{em}}}{E_{\text{em}}} = \frac{\int \frac{1}{2} E^2(\vec{r}) \vec{\nabla} \varepsilon(\vec{r}) \cdot \vec{u}(\vec{r}) d^3r}{2 \int \frac{1}{2} E^2(\vec{r}) \varepsilon(\vec{r}) d^3r}, \quad (91)$$

where $E^2(\vec{r})$ is the squared magnitude of the electric field, and the factor 2 in the denominator is due to the fact that equal amounts of energy are stored in both the electric and magnetic fields. Note however that the magnetic energy does not shift upon a displacement of the boundary, as the magnetic permeability of glass is very close to unity. For a resonator made out of a homogeneous dielectric material, the integral in the nominator is essentially a surface integral over the boundary, as $\vec{\nabla} \varepsilon(\vec{r})$ is zero everywhere except for the surface. We use the coupling constant $g_0 = -\omega_c/R$, expressing the frequency shift as a consequence of an effective radius change. One then finally obtains

$$\vec{w}(\vec{r}) = -\frac{R}{E_{\text{em}}} \cdot \frac{1}{2} E^2(\vec{r}) \vec{\nabla} \varepsilon(\vec{r}). \quad (92)$$

As equation (92) is difficult to analytically evaluate in complex geometries, a useful approximation is given by

$$\vec{w}(\vec{r}) \approx \frac{1}{2\pi R} \delta(z - z_0) \delta(r - R) \vec{e}_r. \quad (93)$$

where R is the major radius and $z = z_0$ the plane of the equator of the toroid. This weighting function essentially considers the transverse size of the

optical mode as negligibly small compared to the scales of the displacement patterns, and the resulting displacement x corresponds to the change of the cavity radius, which is sampled by the optical mode. In this work, equation (93) is applied to derive the displacement induced by the excitation of a particular WGM from the results of FEM simulations.

We finally note that in a dielectric resonator, it is important to also consider strain-optical effects, that is, a strain-dependent refractive index leading to additional resonance frequency shifts for a given excitation of the mechanical mode. This effect was found to dominate the optomechanical coupling in a cryogenic sapphire microwave WGM resonator (Locke and Tobar (2004)). To assess the relative contribution in silica WGM microresonators, we may use the analytic expressions for the strain field (67)–(69) in a *microsphere* to calculate the corresponding change in the refractive index as experienced by the optical mode. Due to the homogeneity of the strain fields on the scale of the optical mode cross section, it can be well approximated by just evaluating the strain fields at the edge of the sphere using (Ilchenko et al. (1998))

$$\delta \left(n^{-2} \right)_{\text{TE}} = p_2 \varepsilon_{rr} + p_1 \varepsilon_{\theta\theta} + p_2 \varepsilon_{\phi\phi} \quad (94)$$

$$\delta \left(n^{-2} \right)_{\text{TM}} = p_1 \varepsilon_{rr} + p_2 \varepsilon_{\theta\theta} + p_2 \varepsilon_{\varphi\varphi}, \quad (95)$$

where the required coefficients of the photo-elastic tensor are given by $p_1 = 0.121$ and $p_2 = 0.270$ (Dixon (1967)). This leads to an extra frequency shift of about 30% (TE modes) and 50% (TM modes), as compared to the shift induced by the displacement of the boundary alone. Evaluation of the strain-optical coupling in a toroid is not possible analytically. For typical torus geometries as used in this work, however, we can extract an extra frequency shift of less than 20% from FEM simulations, in agreement with an earlier estimate (Kippenberg et al. (2005)).

3.3.2 *Effective mass*

As a global coupling coefficient g_0 is used to quantify the coupling strength of an effective displacement x to the resonance frequency ω_c of the cavity, it is necessary to absorb the different coupling strengths of different mechanical modes into another parameter. This parameter is referred to as the *effective mass* of the individual mechanical modes (Gillespie and Raab (1995); Pinard et al. (1999)).

An operational definition of the effective mass of one particular mode (labeled in the following with an index n) can be derived from its potential energy U_n

which can be recast from equation (76) to

$$U_n = \frac{1}{2} M_n \Omega_n (c_n(t))^2 \quad (96)$$

using the free-boundary conditions (Pinard et al. (1999)) and the definition of the moving mass

$$M_n = \int_V \rho |\vec{u}_n^0(\vec{r})|^2 d^3r. \quad (97)$$

As $c_n(t)$ is experimentally not accessible, we want to express the potential energy in terms of the measured displacement of the mode,

$$x_n(t) = \int_V \vec{w}(\vec{r}) \cdot \vec{u}_n(\vec{r}, t) d^3r = c_n(t) \langle \vec{w}, \vec{u}_n^0 \rangle, \quad (98)$$

and therefore require

$$U_n = \frac{1}{2} m_{\text{eff},n} \Omega_n^2 (x_n(t))^2. \quad (99)$$

This immediately leads to the formal definition

$$m_{\text{eff},n} \equiv \frac{M_n}{\langle \vec{w}, \vec{u}_n^0 \rangle^2}. \quad (100)$$

In practice, equation (99) is used to calculate the effective masses from experimental data (where, for a given g_0 , x is directly measured, and $U_n \approx k_B T/2$) or FEM simulations, from which x_n and U_n can be simultaneously extracted.

The effective masses of the fundamental sphere modes can be calculated analytically, as both the potential energy (77) and the resonance frequency (75) as a function of the radius R are known, yielding the numeric relation $m_{\text{eff}} = 8470 \text{ kg/m}^3 \cdot R^3$ for silica, i. e. approximately 30 ng for a 30 μm -diameter sphere. The numerical values for the RBMs in silica microtoroids are lower, in the range of 3 to 20 ng for the typical dimensions used.

3.3.3 Forces acting on the mechanical modes

To calculate the radiation pressure force acting on the mechanical modes, it is necessary to assess the momentum transfer from the optical mode to the dielectric medium. The fundamental starting point for such an analysis in a complex geometry such as a silica WGM resonator is the flux of momentum density of the electromagnetic field in the medium (Landau and Lifshitz (1984); Pfeifer et al. (2007))

$$T_{ij} = -E_i D_j - H_i B_j + \frac{1}{2} \delta_{ij} \left(\sum_k E_k D_k + \sum_k H_k B_k \right), \quad (101)$$

where E , D , H and B denote the usual electric and magnetic fields, indices i and j denote the cartesian components of vectors and tensors, and δ_{ij} is the Kronecker-delta. In vacuum, the entity T_{ij} is usually referred to as Maxwell's stress tensor. The body force \vec{f} , that is, the force density acting on the medium, is given by the divergence of this flux, plus a contribution from a temporal change of the flux density

$$f_i = - \sum_j \frac{\partial T_{ij}}{\partial x_j} - \frac{\partial}{\partial t} \frac{1}{c^2} S_i \quad (102)$$

where

$$\vec{S} = \vec{E} \times \vec{H} \quad (103)$$

is the real-valued Poynting vector. With $\vec{D} = \epsilon \vec{E}$ and $\vec{B} = \mu \vec{H}$ we can write this as

$$\vec{f} = -\frac{1}{2} \vec{E} \vec{E} \vec{\nabla} \epsilon - \frac{1}{2} \vec{H} \vec{H} \vec{\nabla} \mu + \left(\frac{\epsilon \mu}{\epsilon_0 \mu_0} - 1 \right) \frac{1}{c^2} \frac{\partial}{\partial t} (\vec{E} \times \vec{H}) \quad (104)$$

where Maxwell's equations $\vec{\nabla} \cdot \vec{D} = 0$, $\vec{\nabla} \cdot \vec{B} = 0$, $\vec{\nabla} \times \vec{E} = -\mu \partial \vec{H} / \partial t$ and $\vec{\nabla} \times \vec{H} = +\epsilon \partial \vec{E} / \partial t$ were used (Landau and Lifshitz (1984)). We will disregard in the following the last term, the so-called Abraham force⁵ as it is usually small, and oscillates at the optical carrier frequency, so that it averages out on the timescale of a mechanical oscillation. Furthermore, we neglect the second term due to the close-to-unity magnetic permeability of normal glass and obtain finally

$$\vec{f}(\vec{r}) \approx -\frac{1}{2} E^2(\vec{r})^2 \vec{\nabla} \epsilon(\vec{r}). \quad (105)$$

This body force can be recast to

$$\vec{f}(\vec{r}) = \vec{w}(\vec{r}) \frac{E_{\text{em}}}{R} \equiv \vec{w}(\vec{r}) F_{\text{rp}} \quad (106)$$

using equation (92) and the scalar radiation pressure force from equation (39)

$$F_{\text{rp}} = -g_0 \frac{E_{\text{em}}}{\omega}. \quad (107)$$

Note that equation (106) also holds for the simplified assumptions leading to the simplified weighting function (93): If all optical power is concentrated to the rim of the toroid, an estimate for the force density can be derived from a simple consideration: A line element $R d\varphi$ contains the fraction $d\varphi/2\pi$ of the total number of $E_{\text{em}}/\hbar\omega$ intracavity photons, where E_{em} is the total electromagnetic energy stored in the resonator. Within the time $nR d\varphi/c$,

⁵ The nature of this force has also remained a contentious issue for decades (Pfeifer et al. (2007)).

each photon transfers a fraction of $\sin d\varphi \approx d\varphi$ of its momentum $\hbar k$ to the wall, yielding eventually

$$\vec{f}(\vec{r}) = \frac{1}{R} \frac{d\varphi}{d\varphi} \frac{E_{\text{em}}}{2\pi} \frac{\hbar k}{\hbar\omega} \frac{d\varphi}{nR d\varphi/c} \delta(z - z_0) \delta(r - R) \vec{e}_r = \vec{w}(\vec{r}) \frac{E_{\text{em}}}{R}. \quad (108)$$

Irrespective of the detailed form of the weighting function, the energy of the mechanical system is (Pinard et al. (1999))

$$H = \sum_n \frac{1}{2} M_n (\dot{c}_n(t))^2 + \frac{1}{2} M_n \Omega_n^2 (c_n(t))^2 - \langle \vec{f}, \vec{u} \rangle \quad (109)$$

where strain-optical effects are neglected for simplicity. This leads to the following equations of motion for the mechanical mode amplitudes

$$\ddot{c}_n + \Omega_n^2 c_n = \frac{1}{M_n} \langle \vec{f}, \vec{u}_n^0 \rangle \quad (110)$$

or, in the Fourier domain,

$$c_n(\Omega) = \frac{1}{M_n(\Omega_n^2 - \Omega^2 - i\Omega\Gamma_n)} \cdot \left(\langle \vec{f}(\Omega), \vec{u}_n^0 \rangle + \delta F_{\text{T},n}(\Omega) \right) \quad (111)$$

where the damping Γ_n and the corresponding fluctuational force δF_T have been introduced as well. As only the projection x_n of the excitation of the mechanical mode is measured, one obtains

$$\begin{aligned} x_n(\Omega) &= \langle \vec{w}, \vec{u}_n^0 \rangle c_n(\Omega) = \frac{\langle \vec{w}, \vec{u}_n^0 \rangle}{M_n(\Omega_n - \Omega^2 - i\Omega\Gamma_n)} \cdot \left(\langle \vec{f}(\Omega), \vec{u}_n^0 \rangle + \delta F_{\text{T},n}(\Omega) \right) \\ &= \frac{\langle \vec{w}, \vec{u}_n^0 \rangle^2}{M_n(\Omega_n - \Omega^2 - i\Omega\Gamma_n)} \left(F_{\text{rp}}(\Omega) + \frac{\delta F_{\text{T},n}(\Omega)}{\langle \vec{w}, \vec{u}_n^0 \rangle} \right) \\ &= \frac{1}{m_{\text{eff},n}(\Omega_n - \Omega^2 - i\Omega\Gamma_n)} \left(F_{\text{rp}}(\Omega) + \frac{\delta F_{\text{T},n}(\Omega)}{\langle \vec{w}, \vec{u}_n^0 \rangle} \right). \end{aligned} \quad (112)$$

The fluctuational thermal force $\delta F_{\text{T},n}$ used here obeys $\langle \delta F_{\text{T},n}(\Omega) \delta F_{\text{T},n}(\Omega') \rangle \propto M_n$, but the commonly employed approach is to introduce an effective thermal force $\delta F_{\text{th},n}$ with M_n replaced by $m_{\text{eff},n}$ leading to the form (55), and yielding finally

$$x_n(\Omega) = \frac{1}{m_{\text{eff},n}(\Omega_n - \Omega^2 - i\Omega\Gamma_n)} (F_{\text{rp}}(\Omega) + \delta F_{\text{th},n}(\Omega)) \quad (113)$$

the one-dimensional description used in section 2.

As an illustration of the influence of the effective mass, figure 20 shows the spectrum $\bar{S}_{xx}(\Omega)$ of the fluctuations of $x = \sum_n x_n$ for a toroid driven by thermal noise according to equation (113). Data were extracted from FEM

simulations for toroids the major radius of which has been continuously swept from 35 to 100 μm . Frequencies are a direct simulation result, and the effective masses were extracted using equation (93). All quality factors were, for simplicity, assumed to equal 5000. Clearly, the strong signature of the RBM can be discerned for its low effective mass, on top of the background of weaker flexural modes. At a major diameter of $\sim 75 \mu\text{m}$, the avoided crossing discussed in section 3.2.4 is also apparent.

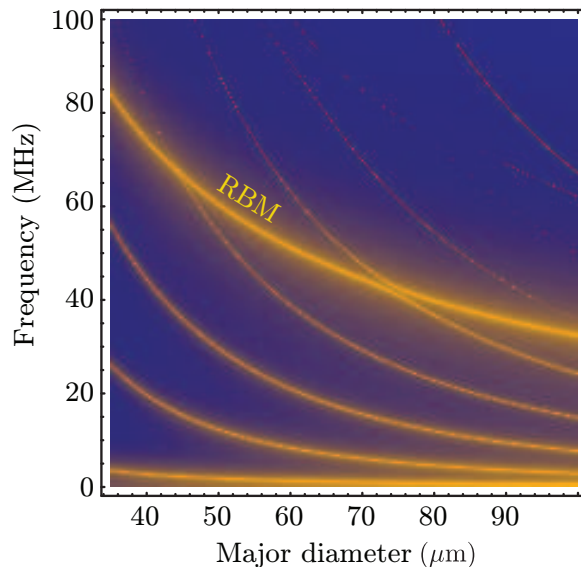


Fig. 20. Color-coded displacement noise spectrum of a toroid with a 1 μm thick silica disk, a 4 μm minor diameter, 90% undercut and a varying major diameter, as simulated using FEM. The strong signature is from the RBM, the other traces are from flexural modes.

4 Ultrahigh-sensitivity interferometric motion transduction

As a first application of optomechanical coupling present in WGM resonators, we consider monitoring of mechanical displacements using the optical degree of freedom. While in early work the separation of two resonators was measured in this manner (Ilchenko et al. (1994)), we focus here on the measurement of displacements related to the internal mechanical modes of WGM resonators (Schliesser et al. (2008a)). The principal idea of such a measurement is illustrated in figure 21. In the following, the theoretical limits, possible experimental implementations, and experimental results will be presented.

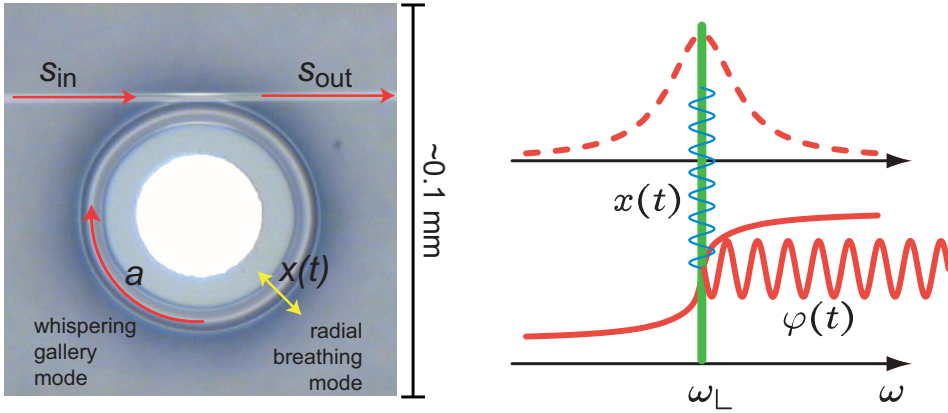


Fig. 21. High-sensitivity displacement sensing using optomechanical coupling. Left panel: an input field s_{in} is launched into the taper and resonantly coupled to the WGM. The properties of the intracavity field a and the field s_{out} coupled back to the fiber taper are modified by the displacement $x(t)$ of the RBM. Right panel: the launched field at frequency ω_l (green line) acquires a phase shift that depends on the mutual detuning of laser and cavity resonance frequency (lower red curve, dashed red curve indicates the WGM Lorentzian as a reference). If the displacement $x(t)$ modulates the WGM resonance frequency, the phase $\varphi(t)$ of the emerging field s_{out} is also modulated. This phase modulation can be detected with quantum-limited sensitivity by comparison with an optical phase reference.

4.1 Theoretical limits of displacement sensing

We first explore the theoretical limits in the sensitivity of the measurement, and restrict ourselves to the simple case of resonant probing $\bar{\Delta} = 0$ (for a more general discussion, see section 7). In this case, the *dynamical properties* of the mechanical oscillator are not affected by the presence of the light in the cavity, that is $\Gamma_{\text{dba}} = \Omega_{\text{dba}} = 0$ in equations (29) and (30). Still, the light can be used as a sensitive probe for the mechanical mode; in the following we discuss the performance and theoretical limitations of this method.

4.1.1 Quantum noise

To analyze the fundamental quantum limits, we directly calculate from equations (50)–(57) the noise in the light field at the output

$$\delta\hat{s}_{\text{out}}(\Omega) = \delta\hat{s}_{\text{in}}(\Omega) - \frac{\sqrt{\eta_c\kappa}}{-i\Omega + \kappa/2} \left(-ig_0\bar{a}\delta\hat{x}(\Omega) + \frac{\delta\hat{s}_{\text{in}}(\Omega)}{\sqrt{\tau_{\text{ex}}}} + \frac{\delta\hat{s}_{\text{vac}}(\Omega)}{\sqrt{\tau_0}} \right) \quad (114)$$

with an analogous equation for $\delta\hat{s}_{\text{out}}^\dagger(\Omega)$. For resonant probing, the mean field at the cavity output is real, and therefore the phase quadrature is directly given by

$$\delta\hat{q}_{\text{out}}(\Omega) = i \left(-\delta\hat{s}_{\text{out}}(\Omega) + \delta\hat{s}_{\text{out}}^\dagger(\Omega) \right). \quad (115)$$

For the symmetrized noise spectral density⁶ of the phase quadrature at the output, defined by

$$\bar{S}_{qq}^{\text{out}}(\Omega) \equiv \frac{1}{2} \left(S_{qq}^{\text{out}}(+\Omega) + S_{qq}^{\text{out}}(-\Omega) \right) \quad (116)$$

with

$$2\pi\delta(\Omega + \Omega')S_{qq}^{\text{out}}(\Omega) = \langle \delta\hat{q}_{\text{out}}(\Omega)\delta\hat{q}_{\text{out}}^\dagger(\Omega') \rangle \quad (117)$$

we obtain

$$\bar{S}_{qq}^{\text{out}}(\Omega) = 1 + \frac{4\bar{a}^2g_0^2\eta_c\kappa}{\Omega^2 + (\kappa/2)^2}\bar{S}_{xx}(\Omega) \quad (118)$$

with the correlation functions from equations (53)–(54). Evidently, the noise spectrum of the phase quadrature contains information on the mechanical displacement spectrum \bar{S}_{xx} , but also a background term (in this normalization equal to 1) which is due to the quantum noise. This background constitutes the fundamental imprecision of the measurement, and is given by

$$S_{xx}^{\text{im,qn}}(\Omega) = \frac{\Omega^2 + (\kappa/2)^2}{4\bar{a}^2g_0^2\eta_c\kappa} \quad (119)$$

if expressed as an equivalent displacement noise. In other words, the imprecision is the *apparent* displacement noise measured in such an experiment, due to the inevitable quantum noise in the measurement of the probing light's phase quadrature.

Recast to experimentally more accessible parameters, equation (119) determines the smallest possible displacement $\delta x_{\text{min}}(\Omega)$ which can be measured

⁶ Note that double-sided spectral densities are calculated in this chapter.

using a WGM resonator (Schliesser et al. (2008a)),

$$\frac{\delta x_{\min}(\Omega)}{\sqrt{\Delta f}} = \sqrt{\bar{S}_{xx}^{\text{im,qn}}(\Omega)} = \frac{\lambda}{16\pi\mathcal{F}\eta_c\sqrt{P_{\text{in}}/\hbar\omega_1}} \sqrt{1 + \left(\frac{\Omega}{\kappa/2}\right)^2}, \quad (120)$$

where λ is the wavelength in the medium and Δf the measurement bandwidth. Written this way, the importance of high-finesse cavities is directly evident: The smallest displacement that can be measured is roughly given by the wavelength, divided by the cavity finesse and the square root of the number of photons accumulated in the measurement time (inverse bandwidth). The term $\sqrt{1 + 4\Omega^2/\kappa^2}$ is due to a less efficient transduction of the motion into phase shift for Fourier frequencies beyond the cavity cutoff (which can, in principle, be avoided using multiple cavity modes (Dobrindt and Kippenberg (2009))).

As an aside, we remark that the same result can be obtained by considering the classical transduction of a displacement into the phase of the light exiting the cavity and comparing the result with the shot noise in the measurement process of the light phase (Schliesser et al. (2008b)). Importantly, equations (119) and (120) are independent of the particular strategy used to detect the light's phase, as long as it can be achieved in a quantum-limited manner. Two strategies to accomplish this, namely homodyne and polarization spectroscopy, are described in section 4.2.

As first discussed by Braginsky (Braginsky and Khalili (1992)), it is inevitable that the measurement of the oscillator's position disturbs it ("measurement backaction"). In the case of an optomechanical system, this is due to the fluctuations of intracavity radiation pressure (Caves (1980)), which can be written as

$$\delta\hat{F}_{\text{rp}}(\Omega) = -\hbar g_0 \bar{a} \left(\delta\hat{a}(\Omega) + \delta\hat{a}^\dagger(\Omega) \right) \quad (121)$$

in equation (50). Again from the known correlation functions, we obtain here

$$\bar{S}_{FF}^{\text{ba,qn}}(\Omega) = \frac{\bar{a}^2 g_0^2 \kappa \hbar^2}{\Omega^2 + (\kappa/2)^2}, \quad (122)$$

if the input noise is again only quantum noise. In this case, the force noise (122) is referred to as *quantum backaction*. Evidently, equations (119) and (122) fulfill the quantum-mechanically required inequality of the imprecision-backaction product (Braginsky and Khalili (1992))

$$\bar{S}_{xx}^{\text{im,qn}}(\Omega) \cdot \bar{S}_{FF}^{\text{ba}}(\Omega) = \frac{\hbar^2}{4\eta_c} \geq \frac{\hbar^2}{4}. \quad (123)$$

By causing *additional* displacement fluctuations in the mechanical oscillator,

backaction noise also impedes the determination of the oscillator’s displacement. The total uncertainty in the measurement is therefore given by

$$\bar{S}_{xx}^{\text{tot}}(\Omega) = \bar{S}_{xx}^{\text{im,qn}}(\Omega) + |\chi(\Omega)|^2 \bar{S}_{FF}^{\text{ba,qn}}(\Omega), \quad (124)$$

where

$$\chi(\Omega) = \frac{1}{m_{\text{eff}}(\Omega_m^2 - \Omega^2 - i\Omega\Gamma_m)} \quad (125)$$

is the susceptibility of the mechanical oscillator. Obviously, a tradeoff in terms of the “strength” $\propto g_0^2 \bar{a}^2$ of the measurement has to be made, as imprecision reduces, but backaction increases for “stronger” measurements (Caves (1980, 1981)), as illustrated in figure 22. Optimum measurement conditions are reached for

$$\bar{a}^2 = \bar{a}_{\text{SQL}}^2 = \frac{m_{\text{eff}}\Gamma_m\Omega_m}{2g_0^2\hbar\kappa\sqrt{\eta_c}}(\Omega_m^2 + (\kappa/2)^2), \quad (126)$$

or, equivalently an input power of $P_{\text{SQL}} = \hbar\omega\kappa\bar{a}_{\text{SQL}}^2/4\eta_c$. In this case, one obtains a total uncertainty of (Schliesser et al. (2008a))

$$\bar{S}_{xx}^{\text{SQL}}(\Omega) = \frac{\hbar|\chi(\Omega)|}{\sqrt{\eta_c}} = \frac{\hbar}{m_{\text{eff}}\sqrt{\eta_c}((\Omega_m^2 - \Omega^2)^2 + \Gamma_m^2\Omega^2)}, \quad (127)$$

called the *standard quantum limit* (Braginsky and Khalili (1992); Caves (1980)) in the case $\eta_c = 1$. Its peak value is calculated at Ω_m ,

$$\bar{S}_{xx}^{\text{SQL}}(\Omega_m) = \frac{1}{\sqrt{\eta_c}} \frac{\hbar}{m_{\text{eff}}\Gamma_m\Omega_m}. \quad (128)$$

In this calculation we have explicitly considered the effect of the coupling conditions to the cavity, which can—as a unique feature—be varied continuously in the experiment by adjusting the gap between the coupling waveguide and the WGM resonator. The SQL is approached most closely in the overcoupled limit $\tau_{\text{ex}} \ll \tau_0$. It is noteworthy that the fibre-taper coupling technique to microtoroids can deeply enter this regime, and $100 \cdot \tau_{\text{ex}} < \tau_0$ ($\eta_c = 99\%$) has been demonstrated (Spillane et al. (2003)).

4.1.2 Laser technical noise

The previous derivation deals with the fundamental sensitivity limits. A frequent *technical* limitation is due to excess (beyond the fundamental) noise of the laser used for probing. Frequency noise in the laser, characterized by a power spectral density $\bar{S}_{\omega\omega}(\Omega)$, corresponds to a higher level of fluctuations in

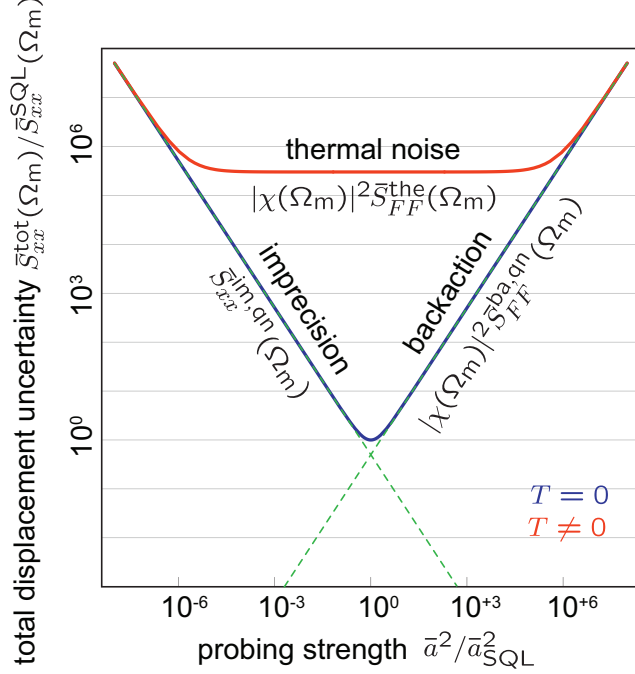


Fig. 22. Quantum limits in the measurement of mechanical displacements (blue line). For weak probing $\bar{a}^2 < \bar{a}_{\text{SQL}}^2$, measurement imprecision dominates the total uncertainty, while for stronger probing $\bar{a}^2 > \bar{a}_{\text{SQL}}^2$, the noise in the mechanical oscillator induced by quantum backaction dominates the uncertainty. For optimum measurements with $\bar{a}^2 = \bar{a}_{\text{SQL}}^2$, the uncertainty is at the standard quantum limit $\bar{S}_{xx}^{\text{SQL}}(\Omega_m) = \hbar/m_{\text{eff}}\Gamma_m\Omega_m$. Under laboratory conditions, thermal noise is additionally present (red line).

the input phase quadrature,

$$\bar{S}_{qq}^{\text{in}}(\Omega) = 1 + \frac{4|\bar{s}_{\text{in}}|^2}{\Omega^2} \bar{S}_{\omega\omega}(\Omega), \quad (129)$$

raising the background on top of which the displacement spectrum has to be observed. Note also that most schemes to measure the phase of the light rely on a phase reference. If this reference is noisy, because it is derived from the same noisy laser, the imprecision in the displacement measurement is given by

$$\bar{S}_{xx}^{\text{im,fn}}(\Omega) = \frac{\bar{S}_{\omega\omega}(\Omega)}{g_0^2} \quad (130)$$

if the frequency noise overwhelms quantum noise in the measurement.

4.1.3 Thermorefractive noise

Another important source of noise potentially preventing the measurement of mechanical displacements with quantum-limited sensitivity is fluctuation of the resonance frequency of the WGM (Gorodetsky and Grudinin (2004); Matsko et al. (2007)) which are not related to the mechanical oscillators. For a dielectric resonator as silica microspheres or -toroids, the dominant effect to be considered here are fluctuations of the refractive index due to temperature fluctuations. At any finite mean temperature \bar{T} , the actual average temperature T_V in a volume V fluctuates according to (Landau and Lifshitz (1980))

$$\langle (T_V - \bar{T})^2 \rangle = \frac{k_B \bar{T}^2}{c_p V \rho}, \quad (131)$$

where ρ is the material density, and c_p the specific heat capacity. This applies in particular also to the mode volume, within which the WGM samples the temperature-dependent refractive index.

To calculate the frequency spectrum of the resulting fluctuations, Gorodetsky and Grudinin (Gorodetsky and Grudinin (2004)) have used a Langevin approach, introducing fluctuational driving terms into the dynamic equations of temperature diffusion (Braginsky et al. (1999, 2000)). As a result, the imprecision due to thermorefractive noise in a silica WGM resonator can be estimated to amount to

$$\begin{aligned} \bar{S}_{xx}^{\text{im,tr}}(\Omega) &= R^2 \bar{S}_{\delta n/n}(\Omega) \approx \\ &\approx \frac{k_B T^2 k R}{\pi^{5/2} n^2 \rho^2 c_p^2} \frac{1}{\sqrt{d^2 - b^2}} \left(\frac{dn}{dT} \right)^2 \int_0^{+\infty} \frac{q^2 e^{-\frac{q^2 b^2}{2}}}{D^2 q^4 + \Omega^2} \frac{dq}{2\pi}, \end{aligned} \quad (132)$$

where k is heat conductivity, R the cavity radius, and d and b the transverse mode dimensions. At low frequency ($\lesssim 10$ MHz), this noise indeed can dominate the measurement imprecision (cf. section 4.3).

4.2 Experimental techniques

4.2.1 Homodyne spectroscopy

A commonly employed technique for quantum-limited phase measurement is a balanced homodyne receiver (Yuen and Chan (1983)), which has been used in earlier optomechanical experiments (Hadjar et al. (1999); Briant et al. (2003); Caniard et al. (2007a)). One possible adaptation of this technique to the ring topology of a WGM resonator is shown in figure 23. The probing (or signal) beam and a phase reference beam, referred to as the local oscillator (LO) are derived from the same laser, in this case a monolithic Nd:YAG laser operating

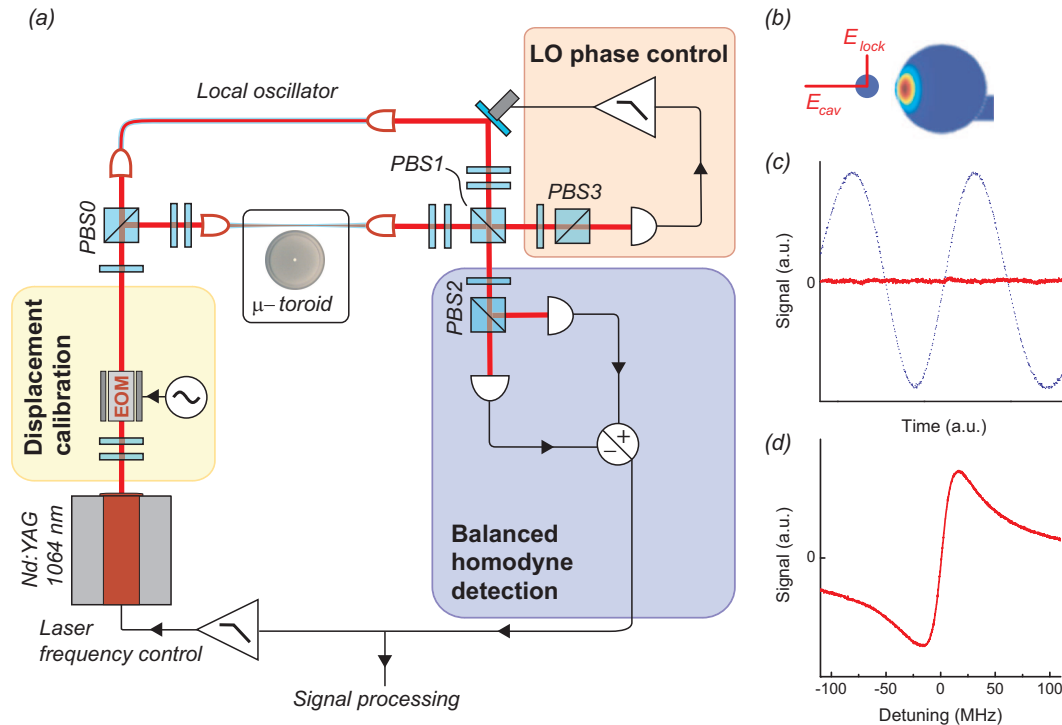


Fig. 23. (a) Optical interferometric displacement transducer based on homodyne spectroscopy of light transmitted past the cavity (“ μ -toroid”). The phase of the local oscillator is actively stabilized (“LO phase control”). Details are given in the text. PBS0-PBS3, polarizing beam splitters. (b) Cross section through the fiber taper and the toroidal rim in the coupling region. The polarization in the taper is slightly mismatched with the polarization of the cavity mode. Thus only the part E_{cav} of the total field couples to the WGM, the other component E_{lock} can be used for the stabilization of the local oscillator phase. The components E_{cav} and E_{lock} are separated in PBS1. (c) Signal in the balanced receiver for a scanning local oscillator (dotted, blue) at low power, and for the locked LO (red). The shown locked trace was recorded for about 5 seconds. (d) Typical experimental error signal in the balanced receiver when the laser is scanned over a cavity resonance with the local oscillator locked to the appropriate phase. Figure from ref. (Schliesser et al. (2008a)).

at $\lambda = 1064$ nm. This source exhibits quantum-limited amplitude and phase noise at Fourier frequencies $\Omega/2\pi \gtrsim 5$ MHz and power levels $P_{LO} + P \lesssim 5$ mW of interest. As tuning speed and range of this laser are limited, it was found advantageous to use a home-built external-cavity diode laser for pre-characterization of several samples until a suitable toroid was found. The probing beam is sent through the coupling taper and interacts with the WGM of the studied toroid. The LO travels in the reference arm of a Mach-Zehnder interferometer over the same distance. It is finally recombined with the signal beam at a polarizing beam splitter (PBS1). Spatial mode matching of the incident beams is enhanced by using single-mode fiber as mode filter on the local oscillator. After spatial recombination, interference is enforced using a retarder plate and another polarizing beam splitter (PBS2).

As the relative phase of the two interfering beams is also subject to drifts and fluctuations, due to, for example, temperature drift of the fiber in which the reference beam propagates, active stabilization is necessary here. In one possible implementation, this is accomplished by purposely introducing a small polarization mismatch between the light in the taper region and the either predominantly TE- or TM-like WGM modes of the microcavity. The polarization component of the probing beam which does not interact with the WGM resonance can then be used to stabilize the phase of the LO (see figure 23). In this case, a dispersive signal,

$$h(\Delta) = \frac{2\eta_c\kappa\Delta}{\Delta^2 + (\kappa/2)^2} \sqrt{P_{\text{cav}}P_{\text{LO}}}, \quad (133)$$

is obtained at the output of the balanced receiver comparing the other polarization component (which is coupled to the WGM) with the LO. Here P_{cav} and P_{LO} are the powers of the probing and local oscillator beams and $h(\Delta)$ is the power difference measured between the two employed receivers. Figure 23 shows an example of an experimental trace obtained when scanning the laser detuning. Evidently, due to its dispersive shape, the d.c.-component of this signal can be used to lock the laser frequency to the WGM resonance frequency using electronic feedback.

In this way, the mean detuning can be stabilized to $\bar{\Delta} = 0$ and with $\Delta = \bar{\Delta} - g_0\delta\hat{x}(\Omega)$ the signal is directly given by

$$h_{\bar{\Delta}=0}(\delta x, \Omega) \approx -\frac{8\eta_c g_0 \delta x(\Omega)}{\kappa} \sqrt{\frac{P_{\text{cav}}P_{\text{LO}}}{1 + (\Omega/(\kappa/2))^2}}, \quad (134)$$

where the reduced signal strength for Fourier frequencies Ω beyond the cavity cutoff can be viewed as a consequence of the reduced buildup of intracavity sidebands (7)⁷. For a strong local oscillator $P_{\text{LO}} \gg P_{\text{cav}}$, the detection noise is given by shot noise caused by the local oscillator beam, and the fluctuations in the detected differential power are simply $\delta h \approx \sqrt{P_{\text{LO}} \hbar\omega_1}$. Comparison with the signal (134) induced by displacements δx then directly give the sensitivity derived in equation (119).

Furthermore, as equation (133) evidently only depends on the mutual detuning of laser and WGM resonance, frequency fluctuations of the laser are indistinguishable from fluctuations due to mechanical displacement. In the case of frequency noise of the laser, this leads directly to the imprecision described by equation (130). On the other hand, an intentional frequency modulation of controlled modulation depth of the laser can be utilized to calibrate the measured signals: a frequency modulation of $\delta\omega$ corresponds to a displace-

⁷ A more detailed calculation is presented in the supplementary information of ref. (Schliesser et al. (2008b)).

ment of amplitude $g_0\delta x$, independent of the detuning and coupling conditions⁸ (Tittonen et al. (1999); Hadjar et al. (1999); Gorodetsky and Grudinin (2004); Schliesser et al. (2008b)). With the calibration at one particular modulation frequency Ω_{mod} , the measured spectra can be absolutely calibrated at all Fourier frequencies, taking into account the reduced sensitivity beyond the cavity cutoff at $\kappa/2$.

4.2.2 Polarization spectroscopy (Hänsch-Couillaud method)

A simplified setup may be obtained by copropagating the local oscillator field in the same spatial, but orthogonal polarization mode as compared to the signal beam (Schliesser et al. (2008b)). Since the WGM modes have predominantly TE or TM character and are not degenerate, this guarantees that the local oscillator is not affected by the cavity. Due to common-mode rejection of many sources of noise in the relative phase between signal and LO (for example, frequency noise in the optical fiber), the passive stability is sufficiently enhanced to enable operation without active stabilization (figure 24).

Enforcing interference between local oscillator and signal beams then corresponds to polarization analysis of the light (comprising both signal and LO) emerging from the cavity. While novel in the present context of a tapered fibre coupled microcavity, this is a well established technique to derive a dispersive error signal from the light reflected from a Fabry-Perot type reference cavity, named after their inventors Hänsch and Couillaud (Hänsch and Couillaud (1980)).

If fiber birefringence is adequately compensated, the error signal is

$$h(\Delta) = \frac{2\eta_c\kappa\Delta}{\Delta^2 + (\kappa/2)^2} \sqrt{P_{\text{cav}}P_{\text{LO}}}, \quad (135)$$

identical to (133), and a typical trace is shown in figure 24(c). This is used to lock the laser at resonance $\bar{\Delta} = 0$ with a bandwidth of about 10 kHz. Calibration of the spectra may be performed as described in the previous section.

While this approach obviously allows one to reduce the complexity of the experiment, this arrangement proved more sensitive to slow temperature drifts in the polarization mode dispersion of the fibers employed, due to the large ratio of signal and LO powers, the magnitudes of which are only defined by the polarization state of the light in the fiber taper region. Improved stabil-

⁸ We emphasize that for this relation to be valid for arbitrary modulation frequencies, it is necessary that the lengths of the two arms of the Mach-Zehnder interferometer are equal.

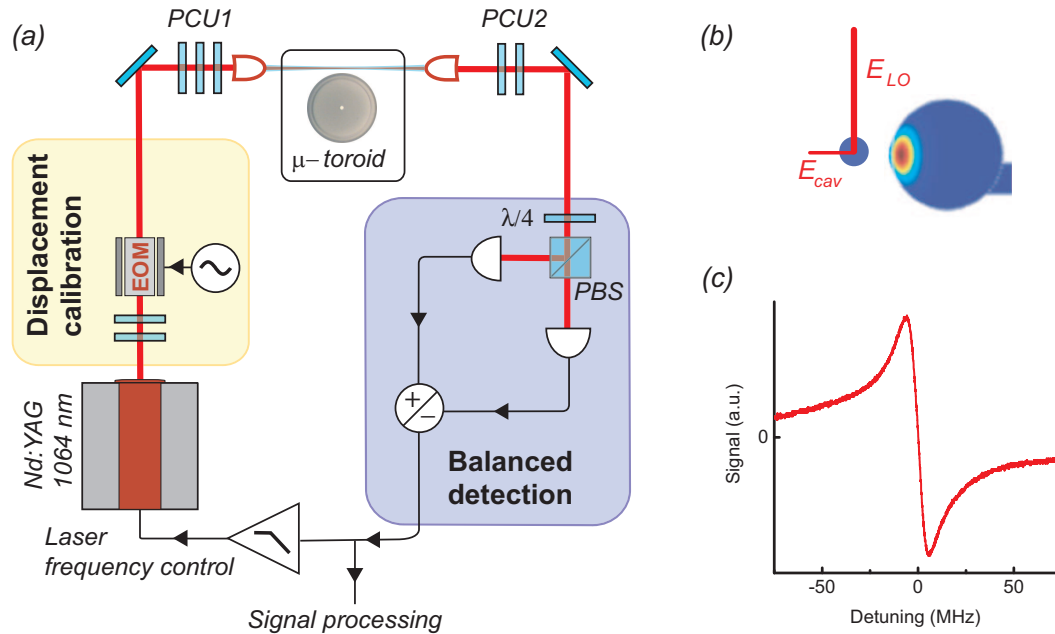


Fig. 24. Optical interferometric displacement transducer based on polarization spectroscopy of light transmitted in the taper past the cavity (“ μ -toroid”). (a) After phase modulation with an electro-optic modulator, the polarization is prepared with a first polarization control unit (PCU1). The cavity WGM defines signal and LO polarizations. A second polarization control unit (PCU2) compensates for fibre birefringence. Polarization analysis using a $\lambda/4$ plate and a polarizing beam splitter enforces interference of the signal and LO fields. (b) Due to the polarization non-degeneracy of the WGM in the cavity, only one polarization component of the light interacts with the mode. (c) Typical error signal obtained when the laser is scanned over a cavity resonance. Figure from ref. (Schliesser et al. (2008a)).

ity may be obtained by reducing the fiber length to its minimum of value of approximately 0.5 m. For reasons of flexibility and convenience, the actual fiber length totaled to several meters in our experiment. Nonetheless, sensitivities of $10^{-18} \text{ m}/\sqrt{\text{Hz}}$ are achieved in toroids using this method (Schliesser et al. (2008b)). The intrinsic polarization selectivity of WGM renders the introduction of an additional polarizer, mandatory in the original implementation (Hänsch and Couillaud (1980)), obsolete. In an earlier experiment with a Fabry-Perot cavity (Hahtela et al. (2004)), the losses associated with an intracavity polarization element limited the finesse, and therefore the attained sensitivity to $\sim 10^{-14} \text{ m}/\sqrt{\text{Hz}}$.

4.2.3 Frequency modulation spectroscopy (Pound-Drever-Hall method)

Another possible method to experimentally determine the detuning of laser and WGM resonance is frequency modulation spectroscopy as introduced by Pound, Drever and Hall (Drever et al. (1983)) and discussed in great detail by Black (Black (2001)). Figure 25 shows a possible application of this scheme

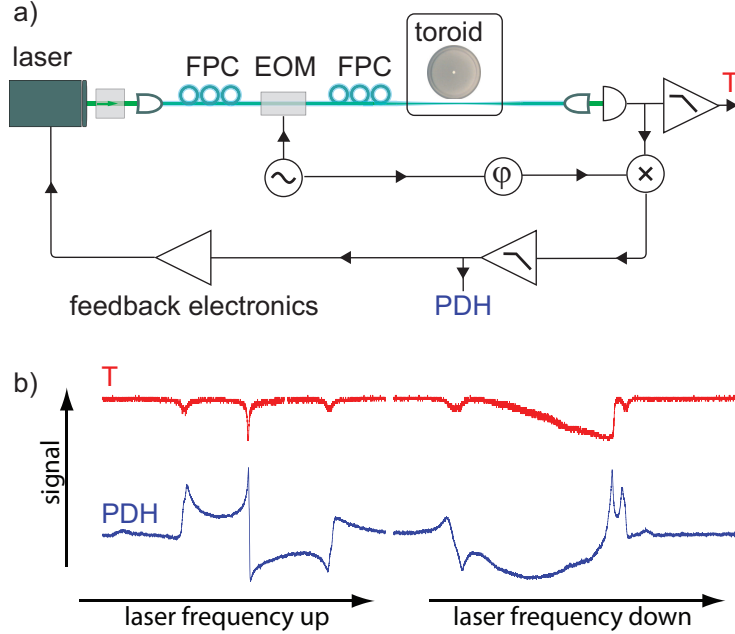


Fig. 25. Displacement measurement using the Pound-Drever-Hall method (Drever et al. (1983)). a) The phase of the probing laser is phase-modulated at a radio-frequency of typically 50–100 MHz using a fiber-coupled electro-optic modulator (EOM). After interaction with the WGM, the detected signal is demodulated at the same frequency. The demodulation quadrature is chosen by adjusting the phase φ of the radio-frequency wave. In the simplest case, this can be accomplished by adjusting the length of the cable carrying the signal. The demodulated signal is low-pass filtered at a bandwidth well below the modulation signal. The resulting signal “PDH” can be used to monitor the detuning of laser and WGM resonance, and is also suited to electronically stabilize the laser frequency to the WGM. In addition, the transmission “T” of the WGM can be directly monitored. FPC, fiber polarization controller. b) Typical traces of transmission and PDH signals obtained with a silica toroidal WGM upon a laser frequency scan in the presence of thermal bistability. The satellite dips in the transmission signal appear when the modulation sidebands are scanned over the WGM frequency.

to WGM resonators. The dispersive shape of the signal can be used to lock the laser to the WGM resonance using electronic feedback. Fluctuations of the Pound-Drever-Hall (PDH) signal beyond the feedback bandwidth then indicate fluctuations of the WGM resonance frequency with respect to the laser frequency, and can therefore be used to monitor displacements.

While both homodyne and polarization spectroscopy can attain the fundamental quantum-limited displacement sensitivity (119), the sensitivity of the

PDH method is reduced by a factor $1 + \eta_c + (1 - 2\eta_c)^2/2J_1^2(\beta)$, where β is the phase modulation depth and J_1 a Bessel function of the first kind (Arcizet (2007)). Note that even for a maximally overcoupled cavity with $\eta_c \rightarrow 1$ this yields $2 + 1/2J_1^2(\beta)$. In practice, the displacement sensitivity using this method is often limited by electronic noise in the detector. As essentially all light used in this scheme interacts with the WGM (there is no phase reference beam in a different spatial or polarization mode), the total power levels must be kept low in order to prevent strong thermal nonlinearities. These light levels (typically a few microwatts) are not sufficient to overwhelm the electronic noise of broadband light receivers. If available at the particular wavelength of interest, a low-noise optical amplifier such as an erbium-doped fiber amplifier (EDFA) can however ameliorate this drawback (Arcizet et al. (2009)) at the expense of a higher noise figure.

4.3 Observation and analysis of quantum and thermal noises

Figure 26 shows data obtained using homodyne spectroscopy on a toroid of about $45 \mu\text{m}$ radius. As long as the taper is retracted from the WGM evanescent field, quantum shot noise is observed to exceed the electronic detector noise. Note that while the detected shot noise (due to the local oscillator) is spectrally flat (white noise) to a good approximation, the equivalent displacement noise plotted in figure 26 exhibits a calculated $\sqrt{1 + \Omega^2/(\kappa/2)^2}$ frequency dependence beyond the cavity cutoff at $\kappa/2 \approx 2\pi \cdot 17 \text{ MHz}$ due to the Fourier frequency-dependent transduction (134).

Approaching the taper to the resonator, and locking the laser to the WGM resonance, a substantially different spectrum is observed (figure 26). The equivalent displacement noise is calibrated in absolute terms using an *a priori* known phase modulation at 36 MHz, as explained in subsection 4.2.1, taking also the cavity cutoff into account. While the background due to quantum measurement imprecision is at a level of $10^{-19} \text{ m}/\sqrt{\text{Hz}}$ at low Fourier frequency, a significantly higher equivalent displacement noise level is observed when coupling the laser to the WGM.

The broad background particularly strong at low frequency can be quantitatively reproduced by the model for thermorefractive noise (equation (132)), when no parameters except b and the absolute magnitude are adjusted by factors of order 2. This is justified considering the approximations made in the derivation, and the incomplete knowledge on the transverse mode shape of the WGM probed in this experiment. We note here as an aside that thermorefractive noise, measured here for the first time in a toroidal microresonator, is an important limitation for the generation of Kerr squeezing in these devices (Rehbein et al. (2005)).

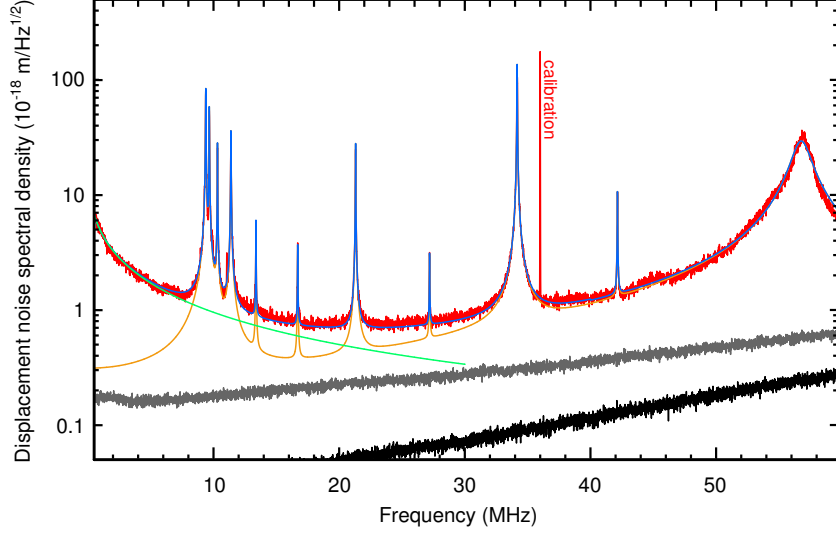


Fig. 26. Equivalent displacement noise measured in a $\sim 90 \mu\text{m}$ -diameter silica toroidal cavity. Red, measured trace with laser coupled to a cavity resonance, including a peak at 36 MHz due to phase modulation for calibration purposes. Gray, measured shot noise with taper retracted from the cavity and black, detector noise. Models for mechanical noise (orange line) and thermorefractive noise (green line), and sum of the two models plus the shot noise background (blue line) are also shown. Figure from ref. (Schliesser et al. (2008a)).

On top of these backgrounds, a sparse spectrum of peaks is observed, which are due to different mechanical modes in the spectrum. In this measurement at room temperature, the thermal Langevin force largely dominates over radiation pressure force fluctuations. Therefore, each individual mode is driven by a random thermal force according to equation (113), and the thermal displacement noise spectra of the individual modes add up to the total measured equivalent displacement noise

$$\bar{S}_{xx}^{\text{tot}}(\Omega) \approx \bar{S}_{xx}^{\text{im,qn}}(\Omega) + \bar{S}_{xx}^{\text{im,tr}}(\Omega) + \sum_n |\chi_n(\Omega)|^2 \bar{S}_{FF}^{\text{th},n}(\Omega), \quad (136)$$

where the symmetrized spectrum of the Langevin force is given, from equation (55), by

$$\bar{S}_{FF}^{\text{th},n}(\Omega) = \hbar m_{\text{eff},n} \Gamma_n \Omega \coth\left(\frac{\hbar\Omega}{2k_{\text{B}}T}\right) \approx 2m_{\text{eff},n} \Gamma_n k_{\text{B}}T, \quad (137)$$

where the second relation is valid as long as $k_{\text{B}}T \gg \hbar\Omega$ for the frequencies of interest.

Figure 27 shows another example of a highly sensitive measurement, using the Hänsch-Couillaud technique in this case. Beyond the clear signatures of the RBM at around 73 MHz, fifteen other peaks related to mechanical modes are observed. Zooming in on the individual peaks reveals that some are split,

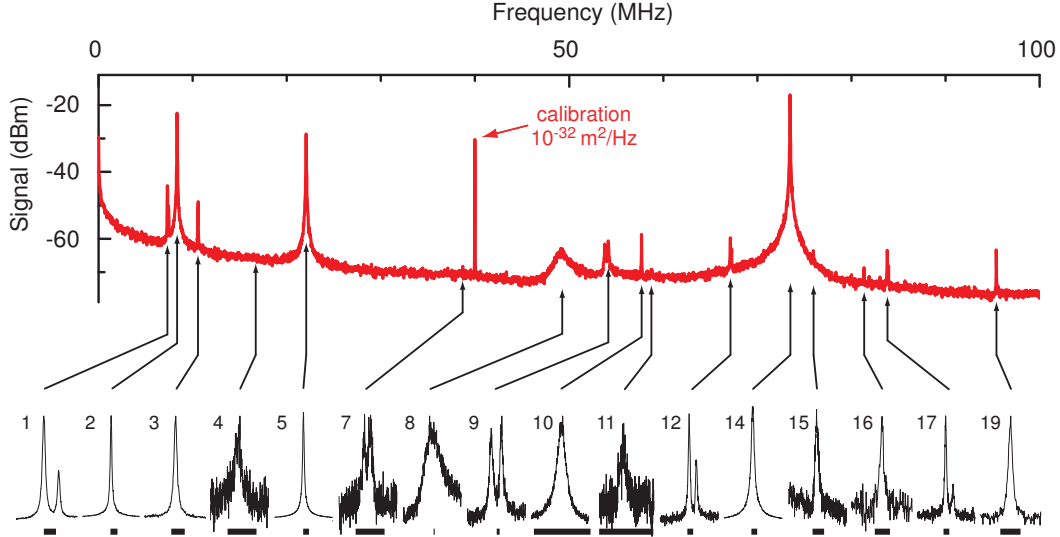


Fig. 27. Broadband displacement noise spectrum recorded using the Hänsch-Couillaud technique (top panel). Zooming in on the individual peaks (lower panels) reveals the precise frequency and linewidth of the modes (scale bar corresponds to a 100 kHz frequency span), some of which are split due to a lifted degeneracy. All observed peaks could be attributed to mechanical modes using finite element modeling (section 3.2.2). Figure from ref. (Schliesser et al. (2008a)).

typically in modes whose degeneracy is lifted by residual asymmetry of the sample. The mode frequencies can be reproduced very accurately using finite element modeling; the peaks shown in this figure correspond to the modes discussed in section 3.2.2 (cf. also figures 12 and 13).

Finally, in figure 28, we zoom in on a frequency interval that has the signature of a radial breathing mode (RBM) of a larger sample ($R = 38 \mu\text{m}$). The measurement achieves a signal-to-background ratio of nearly 60 dB determined by measurement imprecision due to detection shot noise. This dynamic range exceeds the ratio

$$\frac{|\chi(\Omega_m)|^2 \bar{S}_{FF}^{\text{the}}(\Omega_m)}{\bar{S}_{xx}^{\text{SQL}}(\Omega_m)} \approx 2\langle n \rangle. \quad (138)$$

We can therefore conclude that the imprecision background, at a level of $1.1 \text{ am}/\sqrt{\text{Hz}}$, is *below* the standard quantum limit, calculated to $\sqrt{\bar{S}_{xx}^{\text{SQL}}(\Omega_m)} = 2.2 \text{ am}/\sqrt{\text{Hz}}$ for this sample with $\Omega_m/2\pi = 40.6 \text{ MHz}$, $\Gamma_m/2\pi = 1.3 \text{ kHz}$ and $m_{\text{eff}} = 10 \text{ ng}$. We emphasize however, that this does not imply that measurements with a better *total* uncertainty than the standard quantum limit are possible. Quantum backaction-induced fluctuations in the mechanical displacement increase the position uncertainty, but are masked by thermal noise in this measurement.

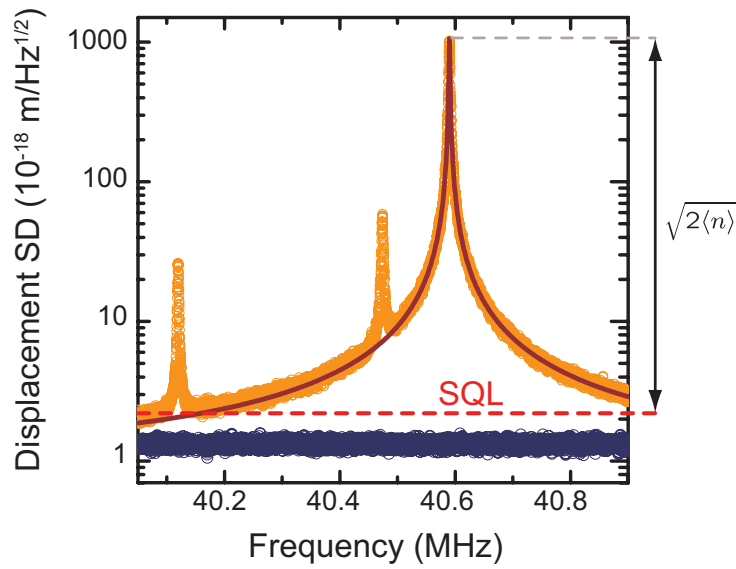


Fig. 28. High sensitivity-measurement of the RBM of a larger sample using the Hänsch-Couillaud technique. Orange circles represent measured data, revealing also the signatures of two neighboring modes. The red line is a Lorentzian fit. Blue circles are the recorded measurement imprecision due to detection shot noise. An excellent signal-to-background ratio of nearly 60 dB is attained, corresponding to a measurement imprecision of $1.1 \text{ am}/\sqrt{\text{Hz}}$, which is well below the standard quantum limit at $2.2 \text{ am}/\sqrt{\text{Hz}}$.

5 Observation of dynamical backaction

In contrast to the resonant probing scenario discussed in the previous section, the dynamics of the mechanical oscillator is modified by radiation-pressure backaction if the optical mode is pumped in a detuned manner. This so-called “dynamical backaction” not only modifies the effective damping and spring constant of the mechanical oscillators, but, as we will show in the following, also leads to an energy exchange between optical and mechanical modes.

Predicted as early as the 1960s by Braginsky (Braginskii and Manukin (1967)), dynamical backaction has been observed early on in mechanical devices coupled to microwave resonators (Braginskii et al. (1970); Braginsky and Manukin (1977); Blair et al. (1995); Cuthbertson et al. (1996); Locke et al. (1998)). In the optical domain, dynamical backaction induced by radiation pressure has been first observed by the Vahala group in 2005 in the form of an oscillatory instability and studied in great detail (Kippenberg et al. (2005); Carmon et al. (2005); Rokhsari et al. (2005, 2006); Hossein-Zadeh et al. (2006)).

Here, we present a systematic study of dynamical backaction as observed in silica microresonators, in particular its dependence on the relevant frequencies κ , Ω_m and $\bar{\Delta}$, and briefly introduce the oscillatory instability described above. In the second part, we focus on the case of negative detuning $\bar{\Delta} < 0$. In this case, the light field extracts energy from the mechanical mode, leading to the cooling of the latter. This effect was first reported by our group at the MPQ in Garching (Schliesser et al. (2006)) and groups in Paris (Arcizet et al. (2006a)) and Vienna (Gigan et al. (2006)). Finally, we rule out thermal nonlinearities as the origin of optomechanical interactions in silica microtoroids.

5.1 *Optical spring and optical damping*

For a detuned optical pump, we have found in section 2.1.3 that the presence of light modifies the dynamics of the mechanical degree of freedom when it responds to an external force. In an intuitive picture, this can be understood as the consequence of the in-phase and quadrature response of the radiation-pressure force, when the mechanical oscillator is driven by the external force. The same result is formally attained using the quantum Langevin approach. Disregarding, in a first step, the quantum fluctuations of the light ($\delta\hat{s}_{\text{in}} =$

$\delta\hat{s}_{\text{vac}} \rightarrow 0$)⁹, the radiation pressure force fluctuations in Fourier space are

$$\delta\hat{F}_{\text{rp}}(\Omega) = i\hbar g_0^2 \bar{a}^2 \delta\hat{x}(\Omega) \left(\frac{1}{-i(\bar{\Delta} + \Omega) + \kappa/2} - \frac{1}{+i(\bar{\Delta} - \Omega) + \kappa/2} \right), \quad (139)$$

equivalent to equation (25). As a consequence, the mechanical oscillator reacts to the thermal Langevin force with the effective susceptibility already derived in equation (27).

To confirm these predictions, a series of measurements was taken using the setup described in figure 29. A 980 nm-wavelength diode laser was locked to a resonance of the silica microtoroid, simply using the transmission signal as an error signal, from which an offset can be subtracted to control the detuning. Moderate optical quality factors ($Q < 10^7$) and low optical powers ($P_{\text{in}} \sim 200 \mu\text{W}$) ensure that thermal nonlinearities are weak enough to still allow stable locking.

Applying this procedure to both the red ($\bar{\Delta} < 0$) and blue ($\bar{\Delta} > 0$) wing of the optical resonance by changing the sign of the error signal, a detuning series can be recorded. From the transmission signal level with the laser locked to the side of the fringe, the relative detuning $\bar{\Delta}/\kappa$ can be determined. At the same time, the fluctuations of the transmitted power, as recorded by the spectrum analyzer, reflect the position fluctuations of the mechanical modes.

Driven predominantly by the thermal Langevin force with its essentially frequency-independent spectrum (137), the measured displacement spectrum directly reveals the effective susceptibility of the mechanical mode. It is therefore possible to extract the effective damping and resonance frequency of the mode using the fit model (27). Figure 30 shows the data obtained from the 56.5 MHz-RBM of a silica microtoroid together with fits by the models (32) and (31). The measured changes in both damping and resonance frequency agree well with expectation.

The resonance frequency shift is often referred to as “optical spring” effect (Sheard et al. (2004)), as it originates from an optical restoring force proportional to the displacement of the resonator. It is interesting to note that this optical force can even exceed the natural restoring force of the mechanical oscillator, and thereby totally dominate the mechanical resonance frequency (Corbitt et al. (2007a)). For silica microresonators, due to the stiffness of the structure, this is typically not the case. In these devices however, another interesting effect occurs for narrow optical resonances ($\kappa < \Omega_m$): in this case, the optical spring force changes its sign for small detunings, turning a restoring into an anti-restoring force and vice versa (Schliesser et al. (2006)), an effect

⁹ This simplification is justified as long as the thermal Langevin force largely exceeds force fluctuations due to the quantum nature of the light.

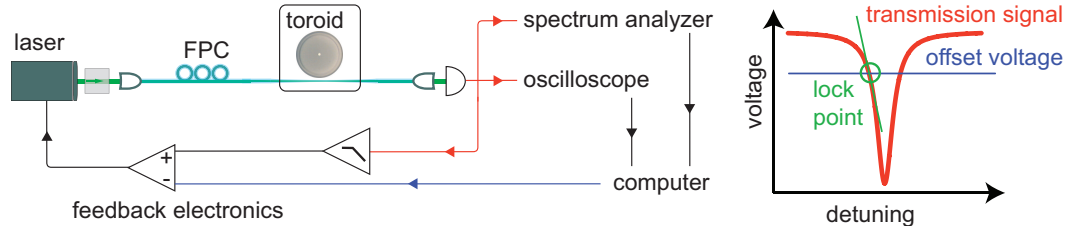


Fig. 29. Schematic illustration of the setup used for the measurement of dynamical backaction. A diode laser is locked to the side of the optical fringe by applying an electronic, computer-controlled offset to the transmission signal. This differential signal is used as an error signal in a feedback loop actuating the laser frequency by regulating both the position of the grating in the laser cavity, and the current pumping the laser diode. Once the laser is locked, the detuning is varied in small steps by adjusting the electronic offset. For each detuning, a trace from the oscilloscope (to determine the actual residual transmission) and a noise spectrum from the electronic spectrum analyzer are taken. FPC stands for fiber polarization controller.

not observed in other systematic studies of dynamical backaction (Arcizet et al. (2006a); Hossein-Zadeh and Vahala (2007)).

The optically induced damping can provide both positive and negative damping. For positive detuning $\bar{\Delta} > 0$, the total damping can reach zero. In this case, the mechanical mode, initially driven by thermal noise, starts to oscillate regeneratively. Specifically, solving $\Gamma_{\text{eff}} = 0$ for a threshold power, one obtains

$$P_{\text{thresh}} = \Gamma_m \frac{\bar{\Delta}^2 + (\kappa/2)^2}{\eta_c \kappa} \frac{\omega_c m_{\text{eff}} \Omega_m}{g_0^2} \times \left(\frac{\kappa/2}{(\bar{\Delta} - \Omega_m)^2 + (\kappa/2)^2} - \frac{\kappa/2}{(\bar{\Delta} + \Omega_m)^2 + (\kappa/2)^2} \right)^{-1} \quad (140)$$

for this optically driven mechanical oscillation to occur. This effect, often referred to as parametric oscillatory instability (POI), has been reported for various systems, including silica microspheres (Ma et al. (2007)) with mechanical modes at up to GHz-frequencies (Carmon and Vahala (2007)). For light powers largely exceeding the threshold, nonlinearities neglected in the linearized models presented in this work lead to complex behavior such as multistability (Marquardt et al. (2006)) and chaos (Carmon et al. (2007)). For an in-depth theoretical discussion of the oscillatory instability, including also quantum effects, we refer the reader to references (Vahala (2008); Ludwig et al. (2008a)).

As an aside we note that in the regime $\kappa \ll \Omega_m = \bar{\Delta}$ discussed in greater detail in section 6, one finds the interesting relation

$$P_{\text{thresh}} = 4\sqrt{\eta_c} P_{\text{SQL}}. \quad (141)$$

This universally relevant power scale (for both dynamical and quantum back-

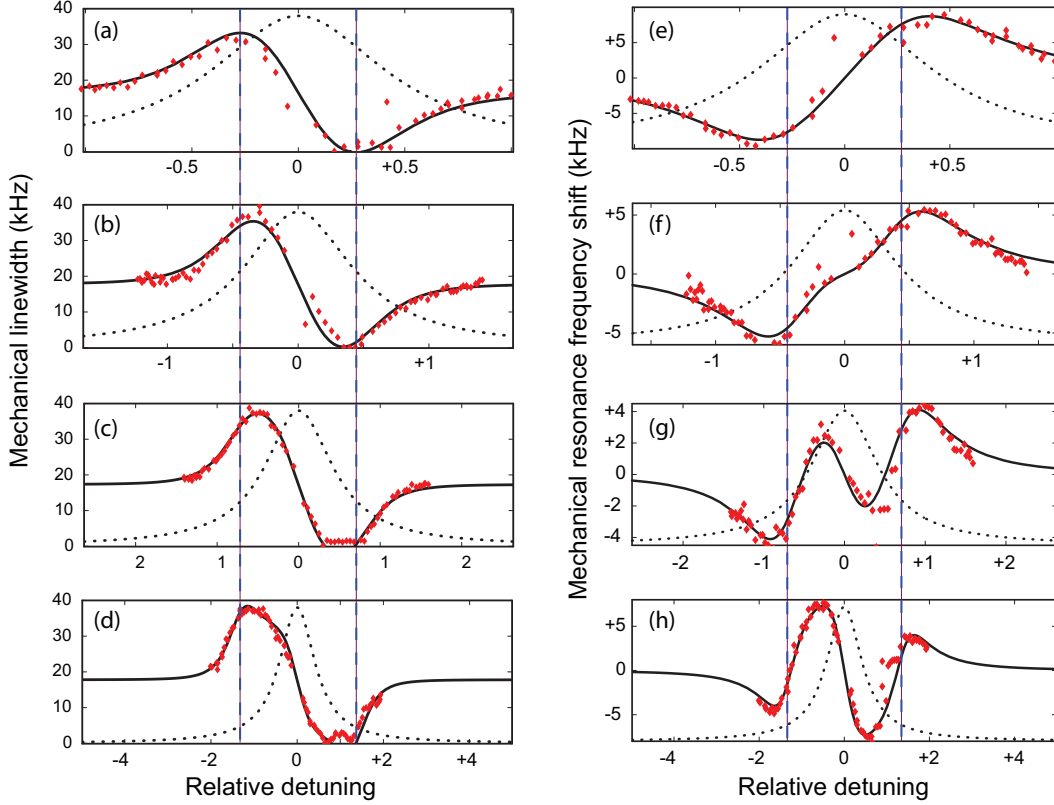


Fig. 30. Linewidth (a–d) and mechanical resonance frequency shift (e–h) of the mechanical mode as a function of relative laser detuning $\bar{\Delta}/\kappa$ for optical resonance linewidths $\kappa/2\pi$ of about 207 MHz (a,e), 127 MHz (b,f), 79 MHz (c,g) and 42 MHz (d,h). Dotted lines indicate the corresponding optical resonance Lorentzian, over which the laser was tuned. Dashed blue lines marks a detuning equal to the mechanical oscillator’s frequency of 56.5 MHz and full lines are fits from the models for dynamical backaction.

action) is at the level of $30 \mu\text{W}$ for typical parameters of silica microtoroids.

5.2 Radiation pressure cooling by dynamical backaction

In the preceding sections, we have only discussed the damping and resonance frequency of the mechanical mode and its modification by dynamical backaction. However, a major feature of light-induced damping is that it also changes the temperature of the mechanical mode. To introduce the concept of a “mode temperature”, let us first evaluate the amplitude of the displacement of a specific mode, which is driven by the thermal Langevin force, by integrating its

noise spectrum over all Fourier frequencies

$$\begin{aligned} \langle \delta x^2 \rangle &= \int_{-\infty}^{+\infty} \bar{S}_{xx}(\Omega) \frac{d\Omega}{2\pi} = \int_{-\infty}^{+\infty} |\chi(\Omega)|^2 \bar{S}_{FF}^{\text{th}}(\Omega) \frac{d\Omega}{2\pi} \approx \\ &\approx \int_{-\infty}^{+\infty} \frac{2m_{\text{eff}}\Gamma_m k_B T}{m_{\text{eff}}^2 ((\Omega^2 - \Omega_m^2)^2 + \Omega^2 \Gamma_m^2)} \frac{d\Omega}{2\pi}. \end{aligned} \quad (142)$$

This integral can be evaluated using the residue theorem, one obtains

$$\frac{1}{2} m_{\text{eff}} \Omega_m^2 \langle \delta x^2 \rangle = \frac{1}{2} k_B T. \quad (143)$$

We may turn this result around and use it to introduce the mechanical mode temperature

$$T_m = m_{\text{eff}} \Omega_m^2 \langle \delta x^2 \rangle / k_B. \quad (144)$$

With this definition, if the mechanical mode is only driven by the Langevin force, it ends up in thermal equilibrium with its environment, and $T_m = T$. As an example, the root-mean-square (RMS) displacement $\langle \delta x^2 \rangle^{1/2}$ of the RBM of a silica microtoroid is typically a few tens of femtometers at room temperature (figure 31).

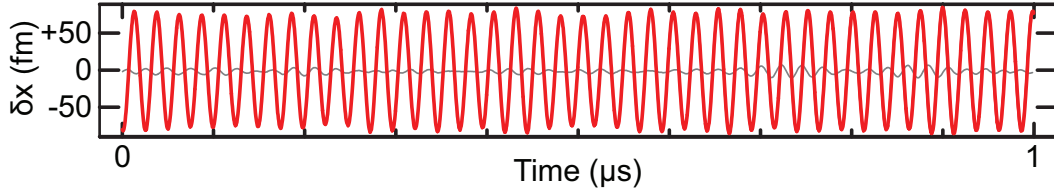


Fig. 31. Real-time recording of the displacement of a 40.6-MHz RBM of a silica microtoroid measured using the Hänsch-Couillaud technique. A 2 MHz-wide band was filtered out of the displacement signal and selectively amplified to record the mechanical trace (red line). The gray line is a background trace recorded with the taper retracted from the cavity. Figure from ref. (Schliesser et al. (2008b)).

In the presence of detuned pumping, the mechanical susceptibility is modified due to dynamical backaction, *the thermal Langevin force, however, is not*. If, therefore, the RMS displacement is calculated from the modified spectrum

$$\bar{S}_{xx}(\Omega) = |\chi_{\text{eff}}(\Omega)|^2 \bar{S}_{FF}^{\text{th}}(\Omega) \quad (145)$$

one obtains

$$\frac{1}{2} m_{\text{eff}} \Omega_m^2 \langle \delta x^2 \rangle \approx \frac{1}{2} \frac{\Gamma_m}{\Gamma_{\text{eff}}} k_B T \quad (146)$$

as long as the mechanical oscillator can be described with its frequency-independent effective damping Γ_{eff} and resonance frequency Ω_{eff} for not too strong backaction effects¹⁰. The mode temperature of the mechanical oscilla-

¹⁰ See e. g. (Genes et al. (2008)) for more general calculations

tor therefore is changed to

$$T_m = \frac{\Gamma_m}{\Gamma_{\text{eff}}} T = \frac{\Gamma_m}{\Gamma_m + \Gamma_{\text{dba}}} T. \quad (147)$$

As for $\Gamma_{\text{dba}} > 0$ one has $T_m < T$ the damping rate Γ_{dba} induced by dynamical backaction is often referred to as the laser *cooling rate*.

Indeed it can be shown that Γ_{dba} is the rate with which energy is transferred from the mechanical resonator to the optical field. Returning, for simplicity, to the example of a sinusoidally oscillating boundary considered in section 2.1 ($x(t) = x_0 \sin(\Omega_m t)$), the cycle-averaged work done by the mechanical oscillator on the optical field can be calculated to

$$P_{\text{dba}} = -\frac{2\pi}{\Omega_m} \int_0^{2\pi/\Omega_m} F_{\text{rp}}(t) \dot{x}(t) dt \approx \Gamma_{\text{dba}} \left(\frac{1}{2} m_{\text{eff}} \Omega_m^2 x_0^2 \right) \quad (148)$$

using only the elementary relations (8) and (11).

In very general terms, this cooling effect arises by coupling the mechanical oscillator not only to the reservoir—consisting of all other mechanical modes present in the device, the gas and thermal radiation field surrounding it etc.—at room temperature, but also to the cooling laser field. Laser cooling therefore disequilibrates the oscillator with the reservoir, and brings it into a new equilibrium in which it is coupled both to the reservoir and the laser field. This field possesses an effective temperature very close to zero (see section 6 for the limitations), and acts as a “cold damper”, by introducing dissipation, but only very little fluctuations to the mechanical mode.

We note here that the application of cold damping schemes has a long history in physics, and has been successfully applied in systems as diverse as electrometers and particle storage rings (Milatz et al. (1953); Milatz and van Zolingen (1953); Möhl et al. (1980)) (here often referred to as “stochastic cooling”). Interestingly, cold damping has also been used to cool a mechanical mode of a mirror in a pioneering 1999 experiment at Laboratoire Kastler Brossel in Paris (Cohadon et al. (1999)), and subsequently in many other experiments (Arcizet et al. (2006b); Kleckner and Bouwmeester (2006); Weld and Kapitulnik (2006); Poggio et al. (2007); Corbitt et al. (2007b)). However, these experiments all involve a complex hybrid electronic/optical feedback loop, whereas the method presented here relies solely on the intrinsic dynamics of radiation pressure.

In figure 32 we show cooling results obtained on the RBM of silica microresonators at frequencies around 57 MHz. In an experimental setup essentially identical to the one described in figure 29, a 980-nm wavelength diode laser was locked to the red wing of an optical resonance. Note that as the thermal bistability renders the red wing dynamically unstable under laser or cavity

frequency fluctuations (Carmon et al. (2004)), special care has to be taken in the implementation of the feedback loop stabilizing the laser frequency to a given detuning.

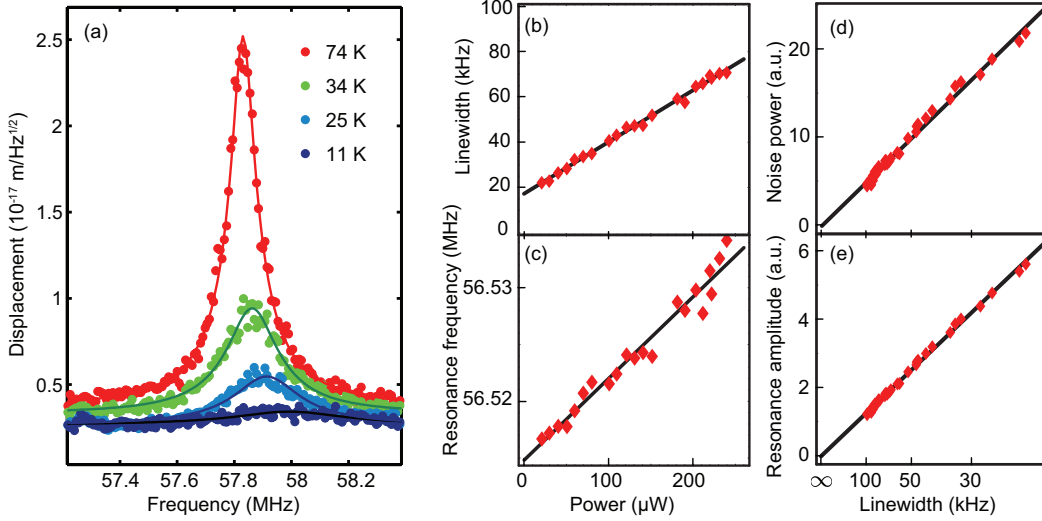


Fig. 32. Cooling of the RBM of silica microtoroids. (a) Noise spectra of the RBM when a 50 MHz-wide WGM resonance is pumped at $\bar{\Delta} \approx -\kappa/2$ with increasing power (0.25 mW, 0.75, 1.25 mW and 1.75 mW). The extracted increased damping rates Γ_{eff} correspond to mode temperatures T_m given in the legend. (b)–(e) Dependence of mechanical mode properties on the launched laser power (measured on the RBM of a different toroid). The linewidth Γ_{eff} and resonance frequency Ω_{eff} vary linearly with input power in this range, and both the noise power $\int_{-\infty}^{+\infty} \bar{S}_{xx}(\Omega) d\Omega / 2\pi \propto T_m$ and the resonance amplitude $\sqrt{\bar{S}_{xx}(\Omega_m)}$ vary linearly with the inverse linewidth Γ_{eff}^{-1} as expected.

As the launched laser power is increased, the total damping increases, and correspondingly so does the width of the Lorentzian resonance. At the same time, the temperature T_m of the mode is reduced by the optical pumping. Panel (a) shows four traces for detuned pumping of a WGM mode with $\bar{\Delta} \approx -\kappa/2 \approx -25$ MHz. For the highest pump powers, the damping is increased beyond 450 kHz, and the corresponding reduced mode temperature is 11 K. The other panels show a systematic power series, in which a different torus was pumped at $\bar{\Delta} \approx -0.7\kappa$ with powers between 20 and 200 μ W.

5.3 Radiation pressure versus thermal effects

In many early experiments, the optomechanical interaction has been mediated by thermal effects, sometimes referred to as “photothermal pressure” instead of radiation pressure (Höhberger Metzger and Karrai (2004); Gigan et al.

(2006); Harris et al. (2007); Favero et al. (2007); Ludwig et al. (2008b)). In the following we present evidence for the fact that the optomechanical interaction in silica microtoroids is strongly dominated by radiation pressure due to the high ($\Omega_m/2\pi \gtrsim 50$ MHz) frequencies of the RBM.

Prior work on the radiation-pressure-induced parametric oscillatory instability has provided independent evidence that radiation-pressure dominates the interaction between optical and mechanical modes (Kippenberg et al. (2005); Rokhsari et al. (2006)) in this system. For instance, it has been shown that the mechanical gain depends on the cavity finesse. This observation demonstrates that radiation pressure is responsible, since thermal forces only depend on the absorbed power and not on the cavity enhanced circulating power.

5.3.1 Theoretical estimate

To theoretically estimate the forces due to light absorption it is necessary to study the coupling of mechanical and thermal waves (or modes) of the structure. Thermodynamical considerations allow us to derive the mutually coupled differential equations for temperature and displacement distributions (Nowacki (1975)), adding a coupling term proportional to the linear expansion coefficient α to the heat diffusion equation and the equations of motion of the displacement field (58).

For small perturbations, we may however assume that the solutions of the uncoupled system ($\alpha \rightarrow 0$) are still approximately valid, and heat transport is still dominated by diffusion. In this case, the resulting temperature gradients give rise to a thermoelastic body force (Nowacki (1975))

$$\vec{f}_{te}(\vec{r}) = -(3\lambda + 2\mu)\alpha \vec{\nabla}\delta T(\vec{r}) \quad (149)$$

driving the mechanical modes (λ and μ are the Lamé constants). Importantly, this body force depends on the gradient of the temperature distribution.

The effective scalar thermal force on a mechanical mode with a displacement pattern \vec{u}_n^0 is determined by an overlap integral $\langle \vec{f}_{te} \vec{u}_n^0 \rangle$. Due to the very high mechanical resonance frequencies, the diffusion length for the temperature distribution $\lambda_D = \sqrt{2k/c_p\rho\Omega}$ becomes very short, for example about 50 nm for $\Omega/2\pi = 50$ MHz. If absorption takes place in the silica, we can therefore conclude that the temperature distribution is essentially given by the energy distribution of the optical mode, and the resulting temperature modulation in the volume can be estimated at $\delta T(\Omega) \approx 2P_{\text{abs}}/\Omega c_p \rho V_{\text{mode}}$, typically $\lesssim 10$ K/W for a typical 30 μm -radius toroid—a value confirmed by finite element modeling of heat diffusion in such a geometry. Due to the nearly *symmetric* temperature distribution in the radial direction with respect to the center of

the optical mode, the overlap integral over the gradient of the temperature distribution can be expected to yield only a small total contribution. For a rough estimate, we may use

$$\begin{aligned} \langle \vec{f}_{te} \vec{u}_n^0 \rangle &\propto \int_V \vec{\nabla} \delta T(\vec{r}) \vec{u}_n^0(\vec{r}) d^3 r \approx |\vec{u}_n^0(R)| 2\pi R d_m \int_{R-d_m}^R \partial \delta T / \partial r dr \\ &\approx |\vec{u}_n^0(R)| 2\pi R d_m \delta T(R), \end{aligned} \quad (150)$$

where $d_m \ll R$ is the transverse diameter of the optical mode. Using $\delta T(R)/P_{\text{abs}} \approx 2 \text{ K/W}$ for the parameters described above (again confirmed by FEM), we obtain $\langle \vec{f}_{rp} \vec{u}_n^0 \rangle / \langle \vec{f}_{te} \vec{u}_n^0 \rangle \approx \mathcal{O}(10^2)$. We note however that this result depends on the exact location of the heat source (absorption may also take place in a water or helium surface layer), and the cooling mechanisms provided by a surrounding medium, effects presently investigated in our group (Zhou et al. (2009)). We also note that at cryogenic temperatures, thermoelastic coupling is weaker as the expansion coefficient drops below $2 \cdot 10^{-9} \text{ K}^{-1}$ at 1.6 K (White (1975); Arcizet et al. (2009)).

5.3.2 Response measurements

Experimentally, we have made response measurements (Rokhsari et al. (2005)) to quantify the different nonlinearities—due to the thermal, Kerr and radiation-pressure effects—encountered in silica microtoroids. To that end, two lasers at different wavelengths (980 and 1550 nm in this case) are coupled to two WGM resonances of a single toroid. One laser, referred to as the “pump”, is amplitude modulated at a variable frequency Ω , while the other “probe” laser is used to measure the response of the WGM frequency to the pump laser power modulation. In the simplest case, this is accomplished by tuning the probe laser to the wing of a WGM resonance, and measuring the variation of its transmission at the same frequency Ω , most conveniently implemented using a network analyzer. Care is taken to suppress direct optical or electronic cross-talk of the pump modulation into this signal.

Figure 33 shows the result of such a measurement on a $29 \mu\text{m}$ -major radius toroid. Clearly, at low frequencies ($\Omega/2\pi < 1 \text{ MHz}$), a strong modulation of the probe WGM frequency is apparent. This is due to absorption of pump light and the consequent modulation of the temperature-dependent expansion and refractive index of the toroid material. Above this frequency, a plateau is observed in the response, due to the modulation of the refractive index seen by the probe WGM, which varies with pump power due to the non-linear refractive index of silica (Kerr effect). Finally, around a mechanical resonance, a dispersive peak is observed. This is due to the excitation of mechanical modes by the modulated pump power.

To fit the response, we use the model

$$\delta\omega_{\text{probe}}(\Omega) = \delta\omega_{\text{th}}(\Omega) + \delta\omega_{\text{K}}(\Omega) + \delta\omega_{\text{rp}}(\Omega) \quad (151)$$

with

$$\delta\omega_{\text{th}}(\Omega) = -\omega_{\text{c}} \left(\alpha + \frac{1}{n} \frac{dn}{dT} \right) \underbrace{\left(\frac{\beta_1}{1 + i\Omega/\Omega_1} + \frac{\beta_2}{1 + i\Omega/\Omega_2} \right)}_{\delta T_{\text{eff}}(\Omega)} \frac{2\pi n R \delta P_{\text{IC}}(\Omega)}{c \tau_{\text{abs}}} \quad (152)$$

$$\delta\omega_{\text{K}}(\Omega) = -\omega_{\text{c}} \frac{n_2 \delta P_{\text{IC}}(\Omega)}{n A_{\text{eff}}} \quad (153)$$

$$\begin{aligned} \delta\omega_{\text{rp}}(\Omega) &= g_0 \chi(\Omega) \delta F_{\text{rp}}(\Omega) = \\ &= -\frac{\omega_{\text{c}}}{R} \frac{1}{m_{\text{eff}}(\Omega_{\text{m}}^2 - \Omega^2 + i\Gamma_{\text{m}}\Omega)} \frac{2\pi n}{c} \delta P_{\text{IC}}(\Omega). \end{aligned} \quad (154)$$

For the thermal effect, we extract cutoff frequencies $\Omega_1 \approx 2\pi \cdot 900$ Hz and $\Omega_2 \approx 2\pi \cdot 69$ kHz. Furthermore, using the material parameters of silica and $R = 29 \mu\text{m}$ as well as $A_{\text{eff}} \approx 2.5 \mu\text{m}^2$, we can normalize all results to the measured Kerr response. In this manner, we extract $\beta_1/\tau_{\text{abs}} \approx 1.8 \cdot 10^4$ K/W/100 ns and $\beta_2/\tau_{\text{abs}} \approx 570$ K/W/100 ns. All these parameters are very well in the range expected for the thermal effects.

The combination of the radiation-pressure and Kerr responses gives rise to the dispersive signature around the mechanical resonance frequency: At modulation frequencies slightly above the mechanical resonance, the mechanical degree of freedom oscillates out of phase and therefore counteracts the Kerr effect, which always reacts instantaneously to power changes. Furthermore, at the resonance frequency Ω_{m} of the RBM we expect

$$\left| \frac{\delta\omega_{\text{rp}}(\Omega_{\text{m}})}{\delta\omega_{\text{K}}(\Omega_{\text{m}})} \right| = \frac{2\pi n^2 A_{\text{eff}}}{R n_2 \Gamma_{\text{m}} \Omega_{\text{m}} c m_{\text{eff}}} \approx 240 \quad (155)$$

with $\Gamma_{\text{m}} = 15.7$ kHz derived from the fit and the numerically determined effective mass $m_{\text{eff}} \approx 15$ ng, in very good agreement to the measured value of 260. The extrapolated thermal effect, in contrast, drops more than four orders of magnitude below the observed mechanical displacement at Ω_{m} (cf. figure 33). At mechanically non-resonant frequencies, this modulation would be largely dominated by a thermorefractive effect as compared to thermoelastic effects, as $(dn/dT)/n\alpha > 10$. Even if enhanced by the mechanical resonance, thermoelastic contributions may therefore be estimated at or below the 10^{-2} -level.

We finally note that thermally induced forces that may be related to the identified thermal effects would be out of phase (by nearly $\pi/2$) with the driving pump laser modulation, since the relevant radio frequencies are well beyond

the thermal cutoff frequencies. As a direct consequence, the observed interference effects between mechanical displacement and the Kerr-induced modulation would form a single symmetric resonant peak, fundamentally different to the observed dispersive shape. This again confirms the dominance of radiation pressure in this system.

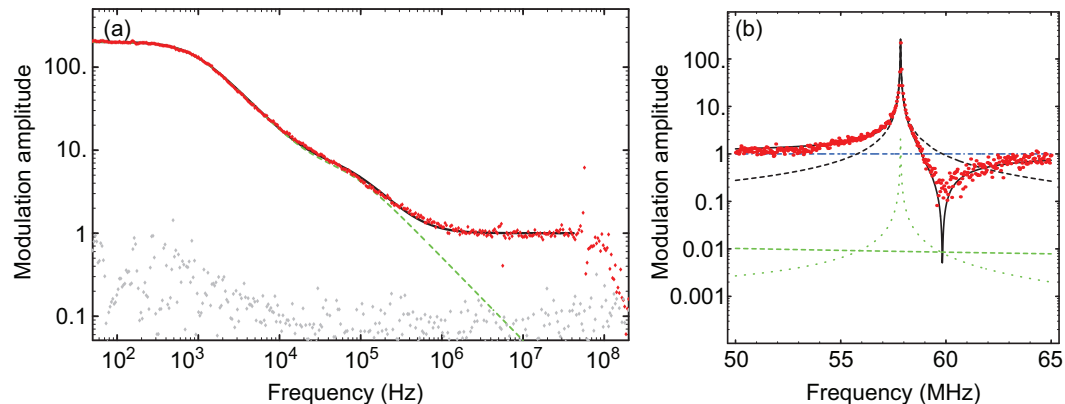


Fig. 33. Pump-probe type response measurements of the nonlinearities present in toroidal silica microcavities. (a) Measured response (red dots) and fit (black line) modeling a two-pole low-pass thermal nonlinearity and an instantaneous Kerr effect, which becomes significant above 1 MHz. The data furthermore show a detector and cavity-induced cutoff above 100 MHz as well as an indication of mechanical resonances at 5.6 and 58 MHz, though not resolved. The green dashed line shows the extrapolation of the thermal effects to higher frequencies and below the measurement background at about 0.1 (gray dots). All data are normalized to the fitted Kerr response. (b) Higher-resolution data (red points) as recorded in the vicinity of the radial-breathing mechanical resonance at ~ 58 MHz. Full black line, model for the harmonic response plus a constant background due to the Kerr effect. Black and blue dashed lines illustrate the individual contributions from the harmonic response and the Kerr effect, respectively. Green dashed line indicates the extrapolated thermal response, and the green dotted line the expected response if the thermally induced displacement was resonantly enhanced. All data are normalized to Kerr response.

6 Resolved-sideband cooling

The successful demonstration of cooling by dynamical backaction immediately raises the question of how strongly the temperature of the mechanical oscillator can be reduced. A series of theoretical and experimental investigations revealed the fundamental (Wilson-Rae et al. (2007); Marquardt et al. (2007)) and technical (Schliesser et al. (2008b); Diósi (2008); Rabl et al. (2009)) limitations of radiation-pressure cooling of mechanical oscillators. In essence, if all technical sources of heating are avoided, the quantum fluctuations of the cooling light field provide a fluctuating force, driving the oscillator to random motion and therefore compete with the laser cooling effect. An advantageous ratio of these two effects can however be achieved in the so-called *resolved-sideband* (RSB) regime, in which the mechanical oscillation frequency Ω_m exceeds the cavity linewidth κ . In this case, cooling of the mechanical oscillator to its quantum mechanical ground state is possible. In the following, a brief outline of the required theoretical considerations will be given after a motivation by well-known results from atomic physics. In the main part of this section, experimental results—including the first demonstration of resolved sideband laser cooling of an optomechanical device—will be presented.

6.1 Ground state cooling: the atomic physics case

The quantum mechanical expectation value of the energy of a harmonic mechanical oscillator of Ω_m and mass m_{eff} is given by

$$\langle H_{\text{mech}} \rangle = \frac{1}{2} \frac{\langle \hat{p}^2 \rangle}{m_{\text{eff}}} + \frac{1}{2} m_{\text{eff}} \Omega_m^2 \langle \hat{x}^2 \rangle = \quad (156)$$

$$= \hbar \Omega_m \left(\langle \hat{n} \rangle + \frac{1}{2} \right) \quad (157)$$

where the phonon number operator $\hat{n} = \hat{b}^\dagger \hat{b}$ is given by the creation and annihilation operators

$$\hat{b}^\dagger = \frac{1}{2x_{\text{ZPF}}} \left(\hat{x} - i \frac{\hat{p}}{m_{\text{eff}} \Omega_m} \right) \quad (158)$$

with the so-called zero-point fluctuations

$$x_{\text{ZPF}} = \sqrt{\frac{\hbar}{2m_{\text{eff}} \Omega_m}}, \quad (159)$$

which are of the order of 100 am for typical silica microtoroidal resonators ($m_{\text{eff}} = 10 \text{ ng}$, $\Omega_m/2\pi = 40 \text{ MHz}$).

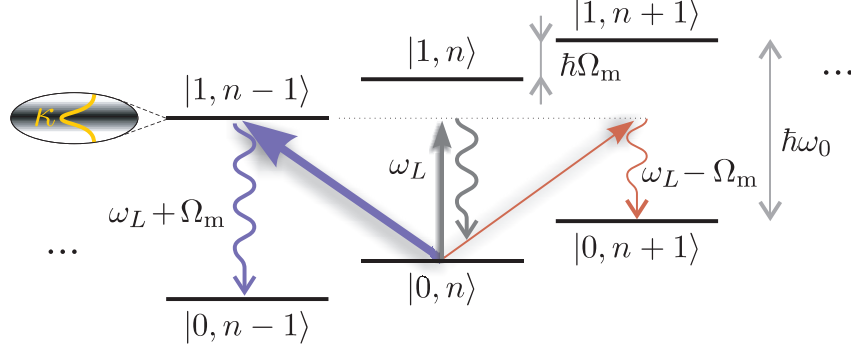


Fig. 34. Optical sideband cooling. Laser photons of energy $\hbar\omega_1 = \hbar(\omega_0 - \Omega_m)$ preferentially induce “red-sideband” transitions $|0, n\rangle \rightarrow |1, n - 1\rangle$ (blue arrow) if they are detuned from the carrier $|0, n\rangle \rightarrow |1, n\rangle$ (gray arrow) and blue sideband $|0, n\rangle \rightarrow |1, n + 1\rangle$ (red arrow) transitions. As a consequence, the phonon occupation n of the mechanical oscillator is reduced when the photon gets absorbed by the atom, or, in the optomechanical case, by the cavity. Re-emission of the photon (wavy lines), on average, does not change the phonon occupation (neglecting recoil), so that a detuned laser provides cooling. Figure from ref. (Schliesser et al. (2008b)).

The question raised by the cooling results presented in the previous section is whether it is possible to reduce $\langle H_{\text{mech}} \rangle$ to levels comparable with the ground-state energy $\hbar\Omega_m/2$. In other words, is it possible to reach the quantum ground state, in which the occupation number (the number of excitation quanta, phonons) $\langle n \rangle$ reaches zero? In this case, deviations from the classical cooling behavior described in the previous section are clearly expected in order to prevent cooling to reach arbitrarily low energy states.

To answer this question, it is instructive to consider the results obtained in the context of laser cooling of ions (or atoms) (Hänsch and Schawlow (1975); Wineland and Dehmelt (1975); Wineland and Itano (1979); Stenholm (1986)). Trapped in a harmonic potential, these elementary particles constitute mechanical oscillators as well, their eigenfrequency Ω_m being given by the tightness of the trap. Lasers can be used to drive electronic transitions of energy $\hbar\omega_0$ and lifetime κ^{-1} , and optical and mechanical degrees of freedom are coupled by the Doppler shift of the optical resonance if the ion is moving and by the momentum transfer of absorbed and emitted photons.

If the laser is detuned from the optical resonance, cooling can occur by favoring the absorption of a photon only in conjunction with the annihilation of a mechanical excitation quantum. Essentially, it is the phonon energy $\hbar\Omega_m$ which makes up for the energy mismatch $\hbar(\omega_0 - \omega_1)$ of the incoming photon to drive the electronic transition. If absorption takes place, the subsequently re-emitted photon has an average energy of $\hbar\omega_0$ (neglecting recoil). It therefore carries away the additional energy of the phonon, and leaves the mechanical oscillator in a state of lower excitation n (figure 34).

This method is usually referred to as optical sideband cooling: an ion oscillating in its trap exhibits absorption sidebands at frequencies $\omega_0 \pm j\Omega_m$, $j \in \mathbb{N}$, very similar to the case of a cavity discussed in section 2.1. If the laser is tuned to the red sideband at $\omega_0 - \Omega_m$, cooling transitions are resonantly enhanced as shown in figure 34. The quantum theory of laser cooling of trapped atoms or ions reveals that this method allows ground state cooling $\langle n \rangle \rightarrow 0$ provided that $\Omega_m \gg \kappa$ (neglecting recoil) (Wineland and Itano (1979); Stenholm (1986)). In this case, the lowest average occupation that can be achieved is given by

$$\langle n \rangle = \frac{\kappa^2}{16\Omega_m^2}. \quad (160)$$

Interestingly, this result can also be viewed as being due to the competition of the cooling effect of the detuned laser, due to an effective viscous force, and a “heating” effect due to quantum fluctuations of the light beam, giving rise to a fluctuating radiation-pressure force (Itano et al. (1992)).

6.2 Limits of radiation-pressure cooling using dynamical backaction

A similar analysis can be applied to cooling by dynamical backaction. To assess the fundamental cooling limits, we consider the radiation pressure force as it is obtained from the quantum Langevin equations:

$$\begin{aligned} \delta\hat{F}_{\text{rp}}(\Omega) = & -\hbar g_0 \bar{a} \left(\frac{\delta\hat{s}_{\text{in}}(\Omega)\tau_{\text{ex}}^{-1/2} + \delta\hat{s}_{\text{vac}}(\Omega)\tau_0^{-1/2}}{-i(\bar{\Delta} + \Omega) + \kappa/2} + \frac{\delta\hat{s}_{\text{in}}^\dagger(\Omega)\tau_{\text{ex}}^{-1/2} + \delta\hat{s}_{\text{vac}}^\dagger(\Omega)\tau_0^{-1/2}}{+i(\bar{\Delta} - \Omega) + \kappa/2} \right) \\ & + i\hbar g_0^2 \bar{a}^2 \delta\hat{x}(\Omega) \left(\frac{1}{-i(\bar{\Delta} + \Omega) + \kappa/2} - \frac{1}{+i(\bar{\Delta} - \Omega) + \kappa/2} \right). \end{aligned} \quad (161)$$

In essence, the expression in the first line correspond to quantum backaction due to quantum fluctuations of the intracavity photon number, while the expression on the second line is due to dynamical backaction (proportional to the mechanical displacement). The latter force contribution, is usually absorbed into the effective susceptibility χ_{eff} from equation (27), while the spectrum of the force quantum fluctuations is calculated as

$$\bar{S}_{FF}^{\text{ba,qn}}(\Omega) = \hbar^2 g_0^2 \bar{a}^2 \frac{\kappa}{2} \left(\frac{1}{(\bar{\Delta} + \Omega)^2 + (\kappa/2)^2} + \frac{1}{(\bar{\Delta} - \Omega)^2 + (\kappa/2)^2} \right) \quad (162)$$

$$= \frac{\hbar^2}{x_{\text{ZPF}}^2} \frac{1}{2} \left(\underbrace{\frac{g_0^2 \bar{a}^2 x_{\text{ZPF}}^2 \kappa}{(\bar{\Delta} + \Omega)^2 + (\kappa/2)^2}}_{A_-} + \underbrace{\frac{g_0^2 \bar{a}^2 x_{\text{ZPF}}^2 \kappa}{(\bar{\Delta} - \Omega)^2 + (\kappa/2)^2}}_{A_+} \right) \quad (163)$$

using the known correlation functions for the input quantum noise. We have introduced here the rates A_- and A_+ , which can be shown to correspond to rates of anti-Stokes and Stokes scattering events in which phonons are annihilated or created (Wilson-Rae et al. (2007); Marquardt et al. (2007); Genes et al. (2008); Clerk et al. (2008)).

The remaining energy stored in the mode after cavity cooling can be evaluated by integrating the mechanical displacement spectrum. This is possible analytically if a hot mechanical reservoir $\hbar\Omega_m \ll k_B T$ is assumed and the effective susceptibility still corresponds to a high-quality Lorentzian. Without further proof we note here that this can be safely assumed as long as the magnitude of the optomechanical coupling parameter

$$G = 2\bar{a}g_0x_{\text{ZPF}} \quad (164)$$

is much less than κ . For higher values of G , hybridization of optical and mechanical modes set in, a regime treated in detail in (Dobrindt et al. (2008); Gröblacher et al. (2009a)). In the limits $\Omega_m, \kappa \gg G, \Gamma_m$ relevant to the work presented in the following, one eventually obtains (Genes et al. (2008))

$$\frac{1}{2}m_{\text{eff}}\Omega_m^2\langle\delta\hat{x}^2\rangle = \int |\chi_{\text{eff}}(\Omega)|^2 \left(\bar{S}_{FF}^{\text{th}}(\Omega) + \bar{S}_{FF}^{\text{ba,qn}}(\Omega) \right) \frac{d\Omega}{2\pi} = \quad (165)$$

$$= \frac{1}{\Gamma_{\text{eff}}} \left(\Gamma_m k_B T + \frac{A_- + A_+}{2} \hbar\Omega_m \right) \quad (166)$$

$$= \frac{\Gamma_m}{\Gamma_{\text{eff}}} k_B T + \frac{A_-}{\Gamma_{\text{eff}}} \hbar\Omega_m + \frac{\hbar\Omega_m}{2}. \quad (167)$$

For significant cooling, one has $A_- \gg A_+ \gg \Gamma_m$, and finally

$$\langle n \rangle \approx \frac{\Gamma_m}{\Gamma_{\text{eff}}} \underbrace{\frac{k_B T}{\hbar\Omega_m}}_{n_{\text{bath}}} + \underbrace{\frac{A_+}{A_- - A_+}}_{n_{\text{min}}}. \quad (168)$$

As a consequence, even for very strong cooling $\Gamma_{\text{eff}} \gg \Gamma_m$, the phonon occupation cannot be reduced to arbitrarily low numbers; instead it is bound by n_{min} . Two simple limits are derived depending on the ratio of mechanical resonance frequency and optical cavity linewidth:

$$n_{\text{min}} \approx \frac{\kappa}{4\Omega_m} \quad \kappa \gg \Omega_m \quad \text{unresolved sidebands} \quad (169)$$

$$n_{\text{min}} \approx \frac{\kappa^2}{16\Omega_m^2} \quad \kappa \ll \Omega_m \quad \text{resolved sidebands.} \quad (170)$$

Evidently, the ground state $\langle n \rangle \rightarrow 0$ can only be reached in the resolved-sideband regime, where $\kappa \ll \Omega_m$. Due to the non-zero occupation $n_{\text{bath}} \approx k_B T / \hbar\Omega_m$ when in equilibrium with the thermal bath, more stringent require-

ments arise in laboratory experiments. In particular, both $\kappa > \Gamma_m n_{\text{bath}}$ (Dobrindt et al. (2008)) and $\Omega_m > \Gamma_m n_{\text{bath}}$ (Marquardt et al. (2007)) are necessary to enable sufficiently high cooling rates without being limited by the cavity decay rate or an effectively overdamped mechanical resonator, respectively. Apart from these limits, it is desirable to work with optical resonances as narrow as possible to enable ground state cooling.

Another advantage of working in the resolved-sideband regime is that the cooling rate increases monotonically for decreasing κ if all other parameters are fixed. As shown in figure 35, if the detuning is chosen for an optimum cooling rate, the intracavity power reduces as the laser is effectively detuned further from the WGM cavity resonance. This is advantageous to keep undesired nonlinearities at a low level, but also to prevent heating effects due to absorbed light. This effect is particularly relevant in cryogenic environments, where small absorbed powers may already significantly alter the temperature of the system, see section 7.3.

Finally, another technical imperfection in this cooling scheme may lead to a limit in the attainable occupation number. If the cooling laser frequency exhibits technical frequency noise, it is translated by the cavity into radiation pressure force noise. Laser frequency fluctuations $\bar{S}_{\omega\omega}(\Omega)$, with $\bar{S}_{qq}^{\text{in}}(\Omega) = 1 + 4|\bar{s}_{\text{in}}|^2 \bar{S}_{\omega\omega}(\Omega)/\Omega^2$ lead to additional radiation-pressure force fluctuations with the spectrum

$$\bar{S}_{FF}^{\text{ba,fn}}(\Omega) = \frac{\hbar^2 \bar{a}^4 g_0^2}{\Omega} \left(\frac{\bar{\Delta}}{(\bar{\Delta} - \Omega)^2 + (\kappa/2)^2} - \frac{\bar{\Delta}}{(\bar{\Delta} + \Omega)^2 + (\kappa/2)^2} \right) \bar{S}_{\omega\omega}(\Omega), \quad (171)$$

which can be derived from the intracavity fluctuations of the p -quadrature. A lower limit for the occupation can then be estimated by integration of the resulting displacement noise spectrum, taking into account the modified susceptibility of the mechanical oscillator (in particular its damping $\Gamma_{\text{dba}} \approx \Gamma_{\text{eff}}$, cf. equation (29). In the linear cooling regime (Dobrindt et al. (2008)), the integrand is simply a Lorentzian, and we assume that the force noise is approximately constant within the frequency band in which it interacts with the mechanical oscillator. Then one obtains

$$m_{\text{eff}} \Omega_m^2 \langle \delta x^2 \rangle \approx \frac{\bar{S}_{FF}^{\text{ba,fn}}(\Omega_m)}{2m_{\text{eff}} \Gamma_{\text{dba}}} = \underbrace{\bar{S}_{\omega\omega}(\Omega_m) \frac{\bar{a}^2 |\bar{\Delta}|}{\kappa \Omega_m}}_{n_{\text{fn}}} \hbar \Omega_m. \quad (172)$$

As will be discussed later, this result gets modified by the additional presence of thermal noise (Schliesser et al. (2008b)), not taken into account in other discussions of frequency-noise induced cooling limits which (Diósi (2008); Rabl et al. (2009)).

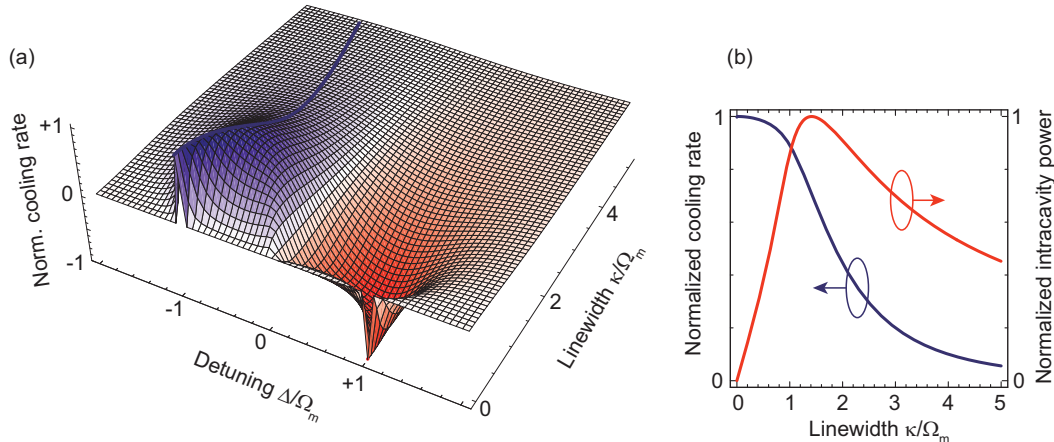


Fig. 35. (a) Normalized cooling rate as a function of detuning and linewidth, for a fixed mechanical resonance frequency Ω_m assuming $G < \kappa$. Blue line indicates the optimum detuning for a given cavity linewidth. (b) Normalized cooling rate (blue line) and intracavity power (red line) as a function of linewidth for fixed Ω_m , if the detuning is kept at the optimum value.

6.3 Resolved-sideband cooling of a silica microtoroid

Implementing an optomechanical system which operates in the resolved-sideband regime is advantageous to suppress the effects of nonlinearities and absorption-induced heating present in most laboratory experiments. Furthermore, the analysis at the quantum level has shown that this regime is mandatory for cooling to the quantum ground state. It is interesting to note that this finding is quite generally valid, and applies in an analogous manner to a large class of systems in which a mechanical oscillator is cooled by parametric coupling to physical systems as diverse as an ion (Tian and Zoller (2004)), a quantum dot (Wilson-Rae et al. (2004)), a Josephson qubit (Martin et al. (2004)), a superconducting quantum interference device (SQUID) (Blencowe and Buks (2007)), a superconducting single-electron transistor (sSET) (Blencowe et al. (2005); Naik et al. (2006)), or a resonant electric circuit (Brown et al. (2007)). The excitations of all these systems need to have a lifetime κ^{-1} exceeding the oscillation period $\sim \Omega_m^{-1}$ of the mechanical oscillator to enable ground-state cooling.

Experimental implementation of the resolved-sideband regime however proves non-trivial: in a classical optomechanical system involving a Fabry-Perot resonator, increasing the cavity length L in principle reduces κ , but at the same time also the coupling strength $g_0 = -\omega_c/L$. Also, it typically increases the waist size of the beam, which may induce diffraction losses (and therefore increase κ again) if, as it is typically the case, the micromechanical oscillator constitutes one of the cavity mirrors. In an integrated system such as silica

microtoroids, increasing the cavity size (within the relevant range of 60 to 100 μm diameter) typically leads only to modest improvements of κ , as the losses are dominated by absorption along the light propagation path. In addition to the reduced coupling $g_0 = -\omega_c/R$, the mechanical resonance frequency of the RBM is reduced for larger cavity size. The first experiment demonstrating efficient resolved-sideband laser cooling was eventually performed in 2008 with silica microresonators (Schliesser et al. (2008b)), while other systems, such as superconducting microwave cavities (Teufel et al. (2008)) or Fabry-Perot resonators (Gröblacher et al. (2009b)) followed soon thereafter.

Figure 36 shows data obtained with a 47 μm -diameter toroid hosting a RBM at $\Omega_m/2\pi = 73.5$ MHz. A first laser drives the RBM to regenerative oscillations, by pumping a WGM in a blue-detuned manner, leading to the well-known oscillatory instability (Kippenberg et al. (2005); Carmon et al. (2005); Rokhsari et al. (2005, 2006); Hossein-Zadeh et al. (2006)). A second laser, launched into the same tapered fibre, is used to probe a different, high-Q WGM resonance of the oscillating toroid. Using optical filters to extract only the transmission signal of the probe laser we obtained the traces shown in figure 36 as this laser is swept over the resonance.

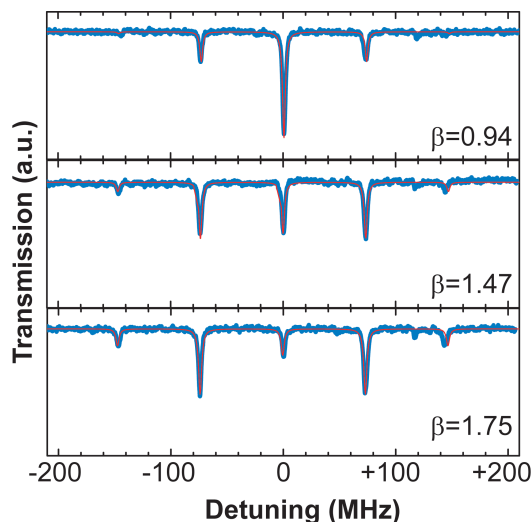


Fig. 36. Steady-state transmission spectrum of a microtoroid when the mechanical degree of freedom is excited to picometer-scale amplitude oscillations at its resonance frequency of $\Omega_m/2\pi = 73.5$ MHz using an auxiliary laser. The linewidth of the resonances corresponds to the optical decay rate of $\kappa/2\pi = 3.2$ MHz, placing this device deeply into the resolved sideband regime. Blue points are experimental data, and the red lines are fits using the Bessel function expansion (equation (173)) with β -parameters given in each panel. Figure from ref. (Schliesser et al. (2008b)).

Instead of a single dip, several dips are observed if the electronic signal is filtered with a low-pass filter with a cutoff far below Ω_m . From the intracavity mode amplitude of the oscillating cavity (equation (7)) the low-frequency

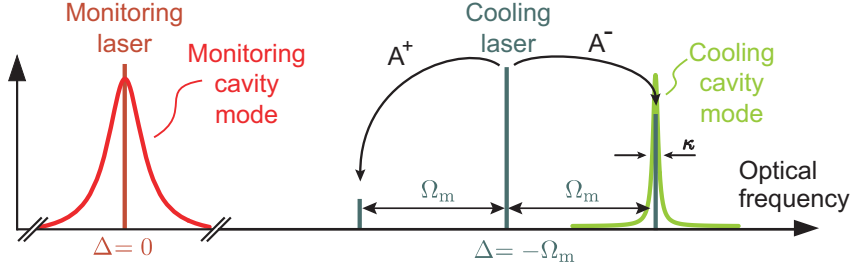


Fig. 37. Scheme used for resolved-sideband cooling. The cooling laser at $\lambda \approx 980$ nm (green line) is tuned to the lower sideband ($\bar{\Delta} = -\Omega_m$) of a high-Q optical resonance. Resonant anti-Stokes scattering into the cavity mode, at rate A_- dominates over Stokes scattering at rate A_+ . A second laser is tuned in resonance with a different WGM at $\lambda = 1064$ nm, and used to monitor the mechanical displacements. Figure from ref. (Schliesser et al. (2008b)).

component of the transmitted power

$$|\bar{s}_{\text{out}}^{\text{DC}}|^2 = \left(1 - \eta_c(1 - \eta_c) \sum_n \frac{\kappa^2 J_n(\beta)^2}{(\Delta + n\Omega_m)^2 + (\kappa/2)^2} \right) |\bar{s}_{\text{in}}^2| \quad (173)$$

is calculated (Schliesser et al. (2008b)), where J_n are the Bessel functions and $\beta = g_0 x_0 / \Omega_m$. From fits using this model, it is possible to derive the amplitude x_0 of the mechanical oscillation as about 5.3, 8.3 and 9.9 pm for the three traces, respectively. At the same time, these traces clearly show that the mechanical resonance frequency Ω_m —by which the Lorentzian dips are spaced—largely exceeds the optical cavity linewidth κ . Indeed, the fits yield a resolved-sideband factor $\Omega_m / \kappa \approx 23$, due to the very high cavity finesse of 440,000.

For resolved-sideband cooling, the two lasers are used in a different way. The cooling laser is tuned below the narrow WGM, to the lower sideband at $\bar{\Delta} = -\Omega_m$. The second laser is used to sensitively monitor mechanical displacements and therefore is tuned in resonance with a different WGM (figure 37). Using two completely independent laser sources helps to rule out artifacts in the displacement measurements, due to potentially induced noise correlations between the cooling beam and induced motion of the mechanical oscillator, referred to as “squashing” in feedback cooling (Poggio et al. (2007)).

In this experiment, sensitive monitoring of mechanical motion is accomplished using the Hänsch-Couillaud technique described in section 4.2.2. As shown in figure 38, a low-noise Nd:YAG laser is used for this purpose, which is locked to the line-center using feedback to a piezo in contact with the YAG crystal. In order to lock the cooling laser to a detuning much larger than the resonance linewidth κ , we use an experimental technique, in which the signal obtained by frequency modulation spectroscopy (Bjorklund et al. (1983)) is used as an error signal.

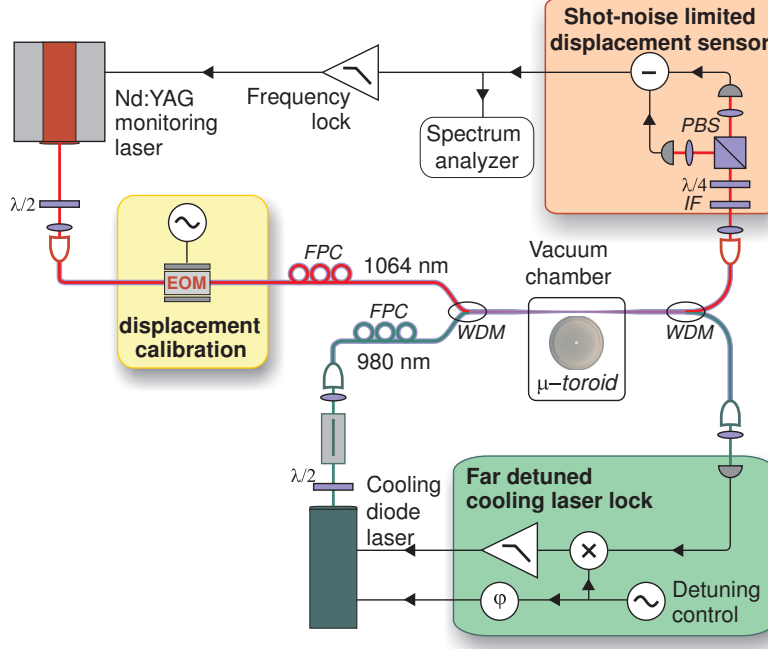


Fig. 38. Setup used to implement resolved-sideband cooling and high-sensitivity monitoring of the RBM of silica toroidal microresonators. Two lasers are used, a diode laser at 980 nm for cooling by tuning and locking it to the lower sideband of a high-Q WGM, and a Nd:YAG laser at 1064 nm monitoring mechanical displacements using the Hänsch-Couillaud technique. More details are given in the text. Figure from ref. (Schliesser et al. (2008b)).

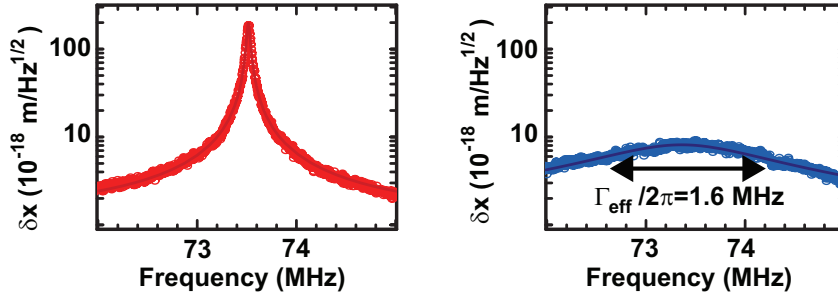


Fig. 39. Displacement noise spectra of the RBM as recorded by the monitoring laser with the cooling laser off (left panel), and running at a power of 2.7 mW, when detuned to the lower sideband (right panel). Cooling rates up to 1.6 MHz can be achieved. Circles are data points and lines Lorentzian fits. Figure from ref. (Schliesser et al. (2008b)).

Figure 39 shows cooling results obtained with the 73.5 MHz-sample. Note that due to the strongly detuned operation, only a fraction of about $\sim (4(\Omega_m/\kappa)^2 + 1)^{-1} \approx 5 \times 10^{-4}$ of the launched power of 3 mW, i. e. circa $1.5 \mu\text{W}$, is coupled into the cavity. Nonetheless, very high cooling rates up to $\Gamma_{\text{dba}}/2\pi = 1.56 \text{ MHz}$ can be achieved. The mode temperatures achieved with this sample, however, remained above 20 K, due to the modest mechanical quality factor of about $Q_m = 2,100$, and a heating mechanism described below.

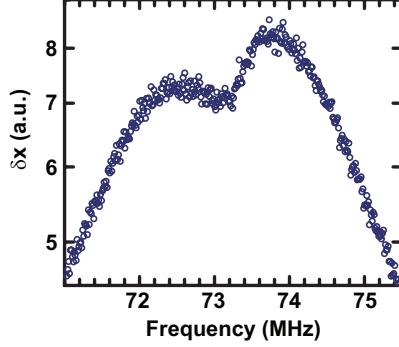


Fig. 40. Resonance doublet observed in the power spectrum of the cooling laser for strong cooling powers. See text for more information.

We have also recorded noise spectra of the mechanical oscillator by directly analyzing the transmitted power of the cooling laser (as explained in section 5). Qualitatively the same behavior of the mechanical spectra is observed during cooling, however with significantly worse signal-to-noise ratio. This renders, for example, the determination of the mode temperature extremely difficult for strong cooling. Furthermore, for cooling laser powers on the order of 3 mW, significant deformations of the mechanical spectra from their originally Lorentzian shape were observed. The particular shapes were strongly dependent on the detuning and coupling conditions. Figure 40 shows one example in which a resonance doublet appeared. We note that such a doublet would in principle be expected when entering the regime of strong optomechanical coupling, in which optical and mechanical modes hybridize (Dobbrindt et al. (2008); Gröblacher et al. (2009a)).

To achieve lower mode temperatures, a second cooling run was initiated. We used a larger toroid (radius $R = 28 \mu\text{m}$) with a RBM at $\Omega_m/2\pi = 40.6 \text{ MHz}$ and $\Gamma_m/2\pi = 1.3 \text{ kHz}$, corresponding to a very high mechanical quality factor of 30,000. The broadband displacement spectrum recorded with this sample using the Hänsch-Couillaud technique (cooling laser is off) is shown in figure 41. A displacement sensitivity at the $10^{-18} \text{ m}/\sqrt{\text{Hz}}$ -level is achieved. At low Fourier frequencies, the noise spectrum again reveals a thermorefractive background already discussed in section 4.

The strong peaks observed at 14.96, 28.58 and 40.59 MHz can be assigned to different radially symmetric modes in this sample. The latter peak belongs to the RBM, which has an effective mass of about 10 ng. If the cooling laser is tuned to the lower sideband of a $\kappa/2\pi = 5.8 \text{ MHz}$ -wide WGM, cooling of the RBM is evident by the reduction of the RBM’s thermal noise (figure 41). It is interesting to note that the thermal noise in the other radially symmetric modes is not affected. In the resolved sideband regime, this is possible due to the fact that the absorption sidebands of the individual mechanical modes do not overlap, as they are as narrow as the optical resonance. Furthermore, we note that effects analogous to “sympathetic cooling”—due to, for example a

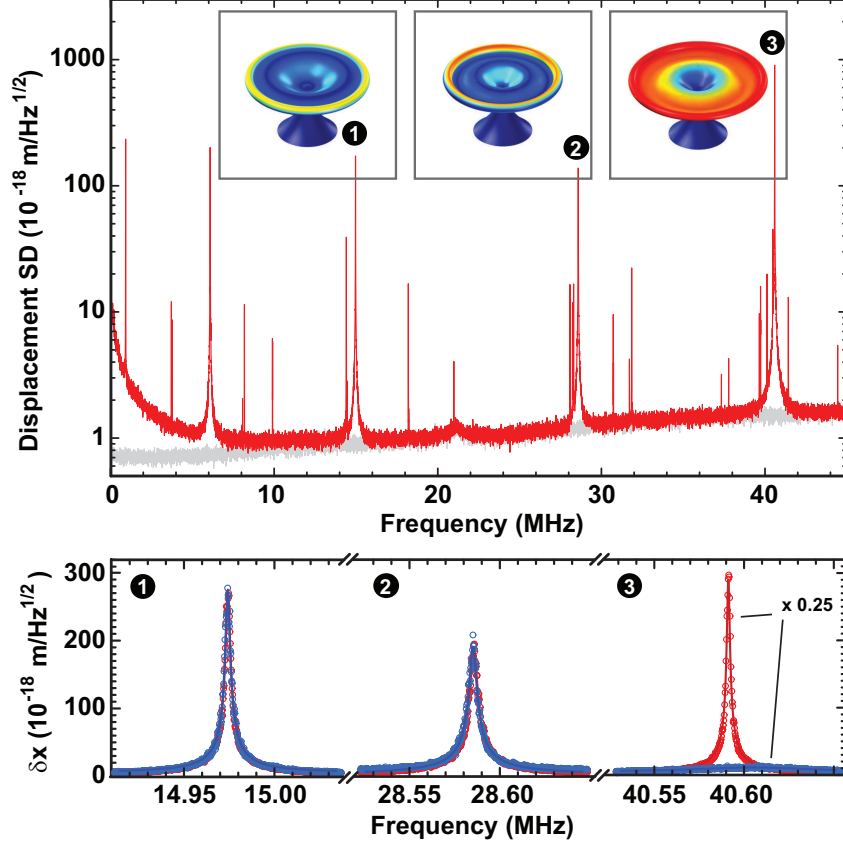


Fig. 41. Resolved-sideband cooling of the RBM of a microtoroidal oscillator. Top panel shows a broadband displacement noise spectrum recorded using the Hänsch-Couillaud technique (red trace). Gray trace is background trace with the fiber taper retracted from the WGM near field. It is dominated by shot noise, its dependence on Fourier frequency is due to the weaker transduction of displacement fluctuations to phase fluctuations at Fourier frequencies beyond the cavity cutoff $\kappa/2$. The sensitivity is at the $10^{-18} \text{ m}/\sqrt{\text{Hz}}$ -level. Insets show the displacement patterns of three radially symmetric modes, with the corresponding strain indicated in the color code. The bottom panel shows zooms on the displacement noise of these three modes, when the cooling laser is off (red traces) and on (blue traces), at a detuning of $\bar{\Delta} = -\Omega_m$. Clearly, only the RBM mode (number 3) is affected. The lowest achieved occupation number in these measurements was $\langle n \rangle \approx 5900$. Figure from ref. (Schliesser et al. (2008b)).

preferential coupling of the RBM to other radially symmetric modes—is not observed.

The mode temperature T_m of the RBM is subsequently evaluated by integrating the displacement noise spectrum $\bar{S}_{xx}(\Omega)$ (cf. section 5.2). The lowest mode temperature obtained with this sample is $T_m \approx 11 \text{ K}$, corresponding to a residual occupation of $\langle n \rangle \approx 5900$. As in the experiments with the first sample, this is significantly above the value expected from the high cooling rates, reaching up to $\Gamma_{\text{dba}}/2\pi = 119 \text{ kHz}$ with this sample. This discrepancy is attributed to

excess heating by the cooling laser's frequency noise.

Indeed, an independent measurement reveals frequency fluctuations of the cooling laser at the level of $\sqrt{\bar{S}_{\omega\omega}(\Omega_m)} = 2\pi \cdot 200 \text{ Hz}/\sqrt{\text{Hz}}$, a value consistent with earlier measurements on the frequency noise at radio frequencies of a grating stabilized diode laser (Zhang et al. (1995)). For a finite bath temperature T , the lowest occupation that can be attained can be estimated by

$$\langle n \rangle \approx \frac{\bar{S}_{FF}^{\text{ba,fn}}(\Omega_m) + \bar{S}_{FF}^{\text{th}}(\Omega_m)}{2m_{\text{eff}}\Gamma_{\text{dba}}}. \quad (174)$$

In the resolved-sideband limit $\kappa \ll \Omega_m$, the force noise due to frequency fluctuations from equation (171) simplifies to

$$\bar{S}_{FF}^{\text{ba,fn}}(\Omega_m) \approx \frac{4\eta_c^2 \bar{S}_{\omega\omega}(\Omega_m) P_{\text{in}}^2}{R^2 \Omega_m^4}, \quad (175)$$

and the cooling rate is approximately given by

$$\Gamma_{\text{dba}} \approx \frac{4g_0^2 \bar{a}^2 x_{\text{ZPF}}^2}{\kappa} = \frac{2g_0^2 \eta_c P_{\text{in}}}{m_{\text{eff}} \omega_1 \Omega_m^3}. \quad (176)$$

As a consequence, the lowest temperature is obtained at a finite input power, and one finds $n_{\text{min}} \approx \sqrt{2k_B T m_{\text{eff}} \Gamma_m \bar{S}_{\omega\omega}(\Omega_m) / \hbar |g_0|}$ (Schliesser et al. (2008b)). For the parameters of this experimental run, $T = 300 \text{ K}$, $m_{\text{eff}} = 10 \text{ ng}$, $\Gamma_m/2\pi = 1.3 \text{ kHz}$, $\sqrt{\bar{S}_{\omega\omega}(\Omega_m)}/\Omega_m^2 \approx 4 \mu\text{rad}/\sqrt{\text{Hz}}$, $R = 38 \mu\text{m}$, $\Omega_m/2\pi = 40.6 \text{ MHz}$, $\omega/2\pi \approx 300 \text{ THz}$, one obtains $n_{\text{min}} \approx 5200$, close to the lowest observed occupation number.

6.4 Direct sideband spectroscopy

If the ground state of the mechanical oscillator is approached, it becomes increasingly difficult to reliably measure its occupation number. For example, if the method demonstrated here—using an independent motion transducer based on an optical phase measurement—the requirements on its performance are quite challenging. Even for a perfect implementation of such a measurement, in which the standard quantum limit can be reached (cf. section 4), the signal-to-background ratio at the mechanical resonance frequency would be only equal to unity at the mechanical resonance frequency when the resonator is in its ground state: for $\langle n \rangle \rightarrow 0$, the spectrum of displacement fluctuations is expected to peak at a value of

$$\bar{S}_{xx}^0(\Omega_m) = \frac{\hbar}{m_{\text{eff}} \Gamma_m \Omega_m}, \quad (177)$$

which exactly equals $\bar{S}_{xx}^{\text{SQL}}(\Omega_m)$.

We note that our experiment reaches an imprecision level close to the SQL: For example, for the sample described above, we calculate $\sqrt{\bar{S}_{xx}^0(\Omega_m)} \approx 2.2 \text{ am}/\sqrt{\text{Hz}}$, and routinely achieve imprecision noise at the same level (cf. figure 41). However, as in most other experiments reporting similarly low imprecision levels (Regal et al. (2008); Teufel et al. (2009)), backaction of these measurements is difficult to quantify and may impede cooling to the quantum ground state.

As an alternative approach to measure the residual occupation number for small $\langle n \rangle$, it has been suggested to directly monitor the individual motional sidebands of the cooling laser (Wilson-Rae et al. (2007)). In theory, the optical spectrum¹¹ of the cooling laser light coupled back into the taper is described by the expression

$$S_{\Phi\Phi}(\omega) = \eta_c \left(\delta(\omega - \omega_1) \left(\frac{1}{\eta_c} - \frac{(1 - \eta_c)\kappa^2}{\Delta^2 + (\kappa/2)^2} \right) \bar{s}_{\text{in}}^2 + \frac{\Gamma_{\text{eff}}/(2\pi)}{(\omega - (\omega_1 + \Omega_m))^2 + (\Gamma_{\text{eff}}/2)^2} A_- \langle n \rangle + \frac{\Gamma_{\text{eff}}/(2\pi)}{(\omega - (\omega_1 - \Omega_m))^2 + (\Gamma_{\text{eff}}/2)^2} A_+ (\langle n \rangle + 1) \right), \quad (178)$$

where Φ is the photon flux emerging from the cavity (Wilson-Rae et al. (2007)). Next to the central line at the carrier frequency ω_1 , two sidebands are expected, their lineshape being determined by the effective susceptibility of the mechanical oscillator. Most notably, the spectrally integrated photon flux of the individual sidebands is given by $A_- \langle n \rangle$ and $A_+ (\langle n \rangle + 1)$ for the upper and lower sidebands, respectively. As a consequence, the sideband asymmetry, given initially by the asymmetry in A_- and A_+ , becomes balanced for sufficiently low $\langle n \rangle$. The change in the ratio of the sideband amplitudes could therefore serve as a gauge of the occupation (Wilson-Rae et al. (2007)).

Accessing the individual sidebands in a measurement necessitates the ability to individually resolve them against the much stronger carrier signal at the laser frequency. For typical parameters of an optomechanical experiment, this is difficult, as in the RSB regime the power even in the resonantly enhanced upper sideband is weaker by $\sim \langle n \rangle g_0^2 4\eta_c^2 x_{\text{ZPF}}^2 / \Omega_m^2 \sim \langle n \rangle \mathcal{O}(10^{-9})$ than the carrier, and the lower sideband is again weaker by a factor of $\kappa^2 / 16\Omega_m^2$. As a consequence, sufficient suppression of the carrier using a (single) filtering cavity is hardly possible, as it would require sub-kHz cavity linewidth, which could not even

¹¹Note that here the high- Q approximation for the mechanical susceptibility was used, $((\Omega_m^2 - \Omega^2)^2 - \Omega^2 \Gamma_{\text{eff}}^2)^{-1} \approx (4\Omega_m^2 ((\Omega - \Omega_m)^2 + (\Gamma_{\text{eff}}/2)^2))^{-1}$. We also emphasize that this spectrum lies in the optical domain, instead of the RF-domain of the spectra discussed previously.

simultaneously collect all light in the sidebands (typically $\Gamma_{\text{eff}}/2\pi > 1$ kHz).

An alternative way of individually resolving the sidebands is to use a heterodyne technique. A similar technique has been demonstrated to enable resolving motional sidebands¹² of a laser-cooled ion (Raab et al. (2000)). In such an experiment, the cooling light which couples back to the fiber taper is mixed with a strong local oscillator beam at a different frequency $\omega_1 - \Omega_{\text{AOM}}$ with $\Omega_{\text{AOM}} > \Omega_{\text{m}}$. Then the upper sideband, carrier, and lower sideband signals are detected at the radio frequencies $\Omega_{\text{AOM}} + \Omega_{\text{m}}$, Ω_{AOM} and $\Omega_{\text{AOM}} - \Omega_{\text{m}}$, respectively.

Figure 42 shows the implementation and results of a proof-of-principle experiment using this technique. When the laser is tuned close to resonance, the motional sidebands have roughly the same amplitude, which are again independently calibrated using a frequency-modulation technique. As $\langle n \rangle \gg 1$, the residual asymmetry in this case is attributed to a finite detuning from the WGM resonance. When the laser is further detuned, the asymmetry becomes more pronounced, as $A_- \gg A_+$. In this experiment, an asymmetry of more than 15 dB is reached. Higher values could not be observed due to the limited SBR. This limitation is due to the classical frequency noise of the cooling laser, which could be shown to induce the relatively high background noise level in this measurement.

We note however that, in contrast to the experiment performed on trapped ions (Raab et al. (2000)), this experiment was performed without actively driving the motion of the mechanical oscillator. In our case, the oscillator is exclusively driven by thermal noise. In that sense, this measurement technique beautifully reveals in a very direct manner the physical process underlying cooling by dynamical backaction: enhanced anti-Stokes scattering and suppressed Stokes-scattering.

¹²Note however that only micro-motion sidebands could be detected for a cold ion. To observe the secular motion, the ion was driven to large-amplitude oscillations in the trap.

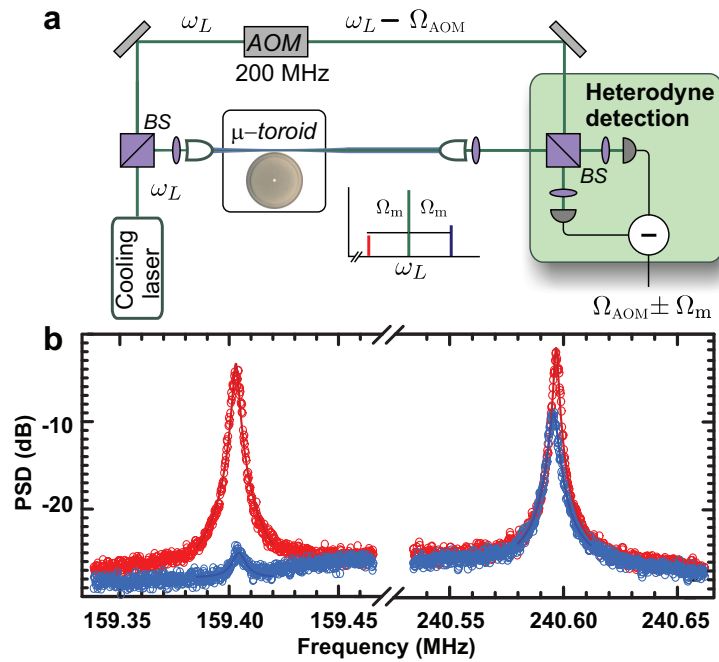


Fig. 42. Heterodyne spectroscopy of the motional sidebands during cooling. (a) Experimental setup, in which a frequency-shifted laser beam is used as a heterodyne local oscillator. (b) Experimental results, showing the power spectral density of the differential photocurrent recorded in the heterodyne receiver. Red points are recorded with the cooling laser close to resonance, and blue points are recorded with a detuned cooling laser. Figure from ref. (Schliesser et al. (2008b)).

7 Approaching the quantum ground state

The work presented in the previous sections has clearly demonstrated the potential of resolved-sideband cooling. In the following, we present experimental results in which this technique is successfully implemented to cool a mechanical oscillator close to its quantum ground state, rivalling the results achieved with nanoelectromechanical systems engineered for this purpose for nearly a decade (Knobel and Cleland (2003); LaHaye et al. (2004); Schwab and Roukes (2005); Naik et al. (2006); ?). In our laboratory these results (Schliesser et al. (2009)) were achieved by combining laser cooling with efficient cryogenic pre-cooling, a technique traditionally applied to nanoelectromechanical systems, but novel in the context of optomechanics.

As a second crucial feature, the vastly superior displacement sensitivity of our optomechanical system warrants the ability to monitor such an ultracold oscillator at levels close to the amplitude of its zero-point fluctuations $x_{\text{ZPF}} = \sqrt{\hbar/2m_{\text{eff}}\Omega_{\text{m}}}$ —in spite of the fact that its mass is more than 1000-times higher than in typical nanomechanical systems.

Finally, considered from the perspective of quantum measurement, we are able to assess the backaction of the measurement performed on the ultracold oscillator. We will show that considering both imprecision and backaction of our measurement, one can conclude that the optical displacement transduction performs in a near-ideal manner.

7.1 Implementation

From the theoretical considerations of the previous sections, we can summarize the limits in cooling by dynamical backaction in the simple expression

$$\langle n \rangle \geq \frac{\Gamma_{\text{m}}}{\Gamma_{\text{m}} + \Gamma_{\text{dba}}} \frac{k_{\text{B}}T}{\hbar\Omega_{\text{m}}} + n_{\text{fn}} + \frac{A_{+}}{A_{-} - A_{+}}. \quad (179)$$

Reaching $\langle n \rangle \rightarrow 0$ therefore requires low mechanical dissipation Γ_{m} , high cooling rates Γ_{dba} , a low environment temperature T , high mechanical resonance frequency Ω_{m} , low frequency noise $S_{\omega\omega}(\Omega_{\text{m}}) \propto n_{\text{fn}}$ of the cooling laser (or, more general, no technical noise of any kind), and operation in the resolved-sideband regime to achieve low $A_{+}/(A_{-} - A_{+}) \approx \kappa^2/16\Omega_{\text{m}}^2$.

After the optimization of the silica microtoroids for low dissipation, high frequency and operation deeply in the resolved-sideband regime, and the demonstration of very high cooling rates, the most significant performance improvements are expected for operation in a cryogenic experiment, and using a cool-

ing laser devoid of any technical noise at the relevant radio frequencies. In the following, we briefly describe the implementation of these two advances.

7.1.1 *Cryogenic optomechanical experiment*

For the successful cryogenic operation of an optomechanical cooling experiment, it is important that the concrete technical implementation provides a proper thermalization of the sample to the cryogen, even in presence of a microwatt-scale heat load through residual light absorption in the sample. This may be a non-trivial task, as strong thermal anchoring of the mechanically compliant device would in many cases imply designs opposite to the requirement of low clamping losses of the mechanical oscillator. For example, the highest mechanical quality factors in silica microresonators were achieved with toroids held only on a sub-micrometric pillar (Schliesser et al. (2008b)), or suspended from silica spokes (Anetsberger et al. (2008)). Heat transport from the region of the optical mode in the torus to a heat sink below the silicon chip can be expected to be prohibitively low.

For this reason, we chose to directly immerse the sample into the cryogen, a dilute helium gas, similar to an early experiment with silica microspheres (Treussart et al. (1998)) immersed in superfluid helium (figure 43). In contrast to other cryogenic experiments with optical microcavities employing a cold finger cryostat (Srinivasan and Painter (2007); Gröblacher et al. (2008)), this allows us to reliably thermalize the sample to the base temperature of the cryostat (1.6 K). At the same time, due its low pressure (typically held in the range 0.1 mbar-50 mbar), and the increased intrinsic damping of the mechanical mode due to two-level fluctuators (see section 3.2.4), the helium gas present in the sample chamber does not induce significant damping of the mechanical mode.

The employed commercial Optistat SXM cryostat (Oxford instruments) implements such a cooling scheme by providing two completely independent helium containers (cf. figure 43): A larger (volume 4.3 liters), thermally insulated reservoir contains liquid helium. From this reservoir, a rotary pump continuously draws helium through a capillary contained in a copper block. During this process, the helium evaporates and cools to temperatures down to 1.6 K. The copper block has a large central bore (49 mm diameter), and constitutes part of the wall of the second helium container—an approximately 50 cm-long tube filled with low-pressure helium gas. It therefore serves as a heat exchanger between the cold He gas from the reservoir and the buffer gas in the central chamber in which the sample is held. The temperature of the heat exchanger can be continuously tuned by controlling the evaporation rate of the He using a control valve. In addition, an electric heater in the copper block allows electronic temperature stabilization, and makes the whole

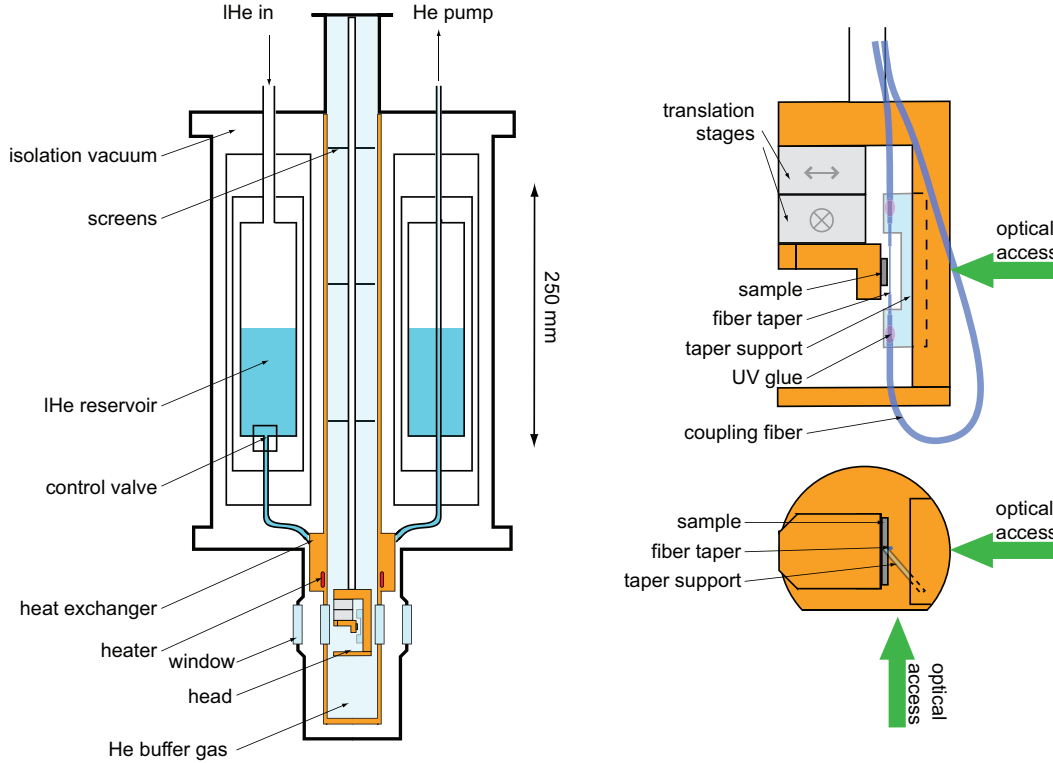


Fig. 43. Implementation of cryogenic cooling. Left panel: schematic drawing of the employed buffer gas cryostat. Liquid ^4He , kept in an isolated reservoir, evaporates when pumped through a capillary (“heat exchanger”) and thereby cools low-pressure (0.1 mbar-50 mbar) ^4He -gas in the sample space to temperatures down to 1.6 K. However, a heater can also be used to stabilize the temperature of the buffer gas to a different value in the full range up to 300 K. The experimental assembly (“head”) is directly immersed into the buffer gas. Right panel: side (top) and bottom (bottom) view of the experimental head. The coupling taper, glued to a glass taper mount, is fixed, while the position of the chip containing the silica microresonators can be adjusted using stick-slip piezoelectric actuators. Optical access from two orthogonal directions allows convenient addressing the toroids on a chip, and precision positioning for coupling to the tapered fiber.

temperature range up to 300 K accessible.

Successful coupling to the WGM in the toroids requires a stable, micrometer-scale gap between the fiber taper and the edge of the toroid. Low vibrations in the experimental assembly are therefore an important selection criterion. The chosen system has successfully been operated in many labs for the purpose of low-temperature scanning-probe microscopy—obviously very vibration-sensitive applications. Both the suspension of the experimental head from a ~ 0.5 m-long metallic rod into the buffer gas, and our compact head design (figure 43) indeed renders the cryogenic coupling setup extremely stable (Rivière et al. (2010)). Standard techniques to reduce the coupling of vibrations from the running pumps (heavy masses on the transfer pipes between

cryostat and pump) are sufficient to eliminate vibrations to a degree that they cannot be observed in any experimental signal. At the same time, this cryostat allows convenient optical access from two orthogonal directions, providing both a side and top view of the silicon chip. Standard machine vision products (Navitar 12 \times) with large working distance (~ 9 cm) allow observation of the coupling region with up to $\times 14$ -magnification, sufficient for convenient addressing and alignment of the toroids versus the fixed fiber taper.

Preparation of a cryogenic cooling experiment includes two critical tasks: selection of an adequate cooling sample and preparation of a fiber taper mounted into the experiment. In particular, the resonators on the chip are tested for high-Q WGM resonances allowing to enter the RSB regime ($\kappa < \Omega_m$) and for low-mass, high-quality RBM modes. These measurements are done in standard room-temperature coupling setups. If an adequate sample is found, it is mounted into the cryogenic head.

The compactness of the cryogenic experiment renders the use of the bulky metallic taper holders used during taper fabrication impossible. Instead, tapers have to be transferred to a compact glass support made of a microscopy glass slide which, importantly, features the same coefficient of thermal expansion as the taper. In that manner, the taper tension remains constant during cooldown of the cryostat.

The fabrication and transfer of the fiber taper proceeds in several steps which are illustrated in figure 44. After the standard fabrication procedure in a hydrogen flame, the taper, still in the fabrication holder, is placed in an auxiliary testing setup. Here, a microtoroid is approached until it touches the taper at its central position. If retracted again, the toroid pulls the taper with it for a certain distance due to proximity forces. Using a micrometer drive, the taper is strained by increasing the separation of the clamps (“elongation” in figure 44), and the tests are repeated until the distance over which the taper can be displaced by the toroid is in the range of $10 \mu\text{m}$. While not particularly quantitative, this simple test was found very helpful in the delicate task of mounting a well-strained taper into the cryostat: floppy tapers make coupling at low temperatures impossible, while too tightly strained tapers are prone to rupture during cooldown. The glass support, fabricated from a simple microscopy slide is then positioned underneath the taper with a 3d-translation stage. The taper is glued to the support with UV-hardening epoxy applied first on one side, hardened, and then on the other side. Then the fiber is released from the metal holder and transferred to the cryostat. We finally note that due to its reduced diameter and potentially lower quality of the available single-mode fiber material, creating a cryogenic fiber taper at shorter wavelength (e. g. 780 nm as in this work) is significantly more difficult than at near-IR wavelengths ($1.5 \mu\text{m}$).

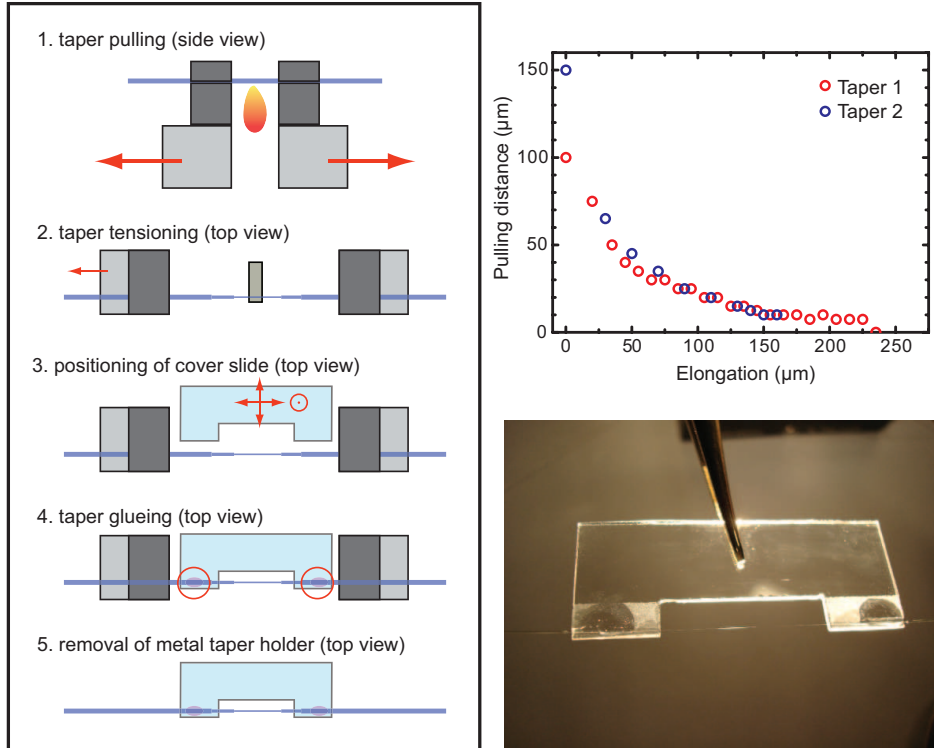


Fig. 44. Five steps in the fabrication and transfer of a fiber taper to the compact glass support used in the cryogenic experiments (left panel). After pulling the taper over the flame of a hydrogen torch, its strain is tested using an auxiliary chip with microtoroids (upper right graph). If properly strained, the glass support (prepared from a cover slide) is positioned underneath the taper, and the fiber is glued to the support with an epoxy. After hardening the epoxy with UV light, the metal clamps of the fabrication holder are opened to release the taper now only held by the glass support (photograph bottom right). It can then be mounted into the experimental head. See text for more details.

The slide carrying the taper is then mounted into the experimental head, and the fiber ends are guided to the top of the sample insert and leave the cryostat via a helium-tight feedthrough. We have achieved total optical transmission through the cryostat up to 80% from fiber end to fiber end. A toroid from the mounted sample can then be approached using the piezoelectric stick-slip actuators (Attocube systems) that carry the sample chip. For testing purposes, and to check the correct alignment of the taper mount (position, tilt), these experiments can also be done with the sample insert (experimental head, suspension rod, and top vacuum flange) held outside the cryostat.

To verify the effectiveness of the buffer gas, a sample with microtoroids, and a coupling taper suited for 1550 nm-light was mounted into the cryostat. The cryostat was cooled down, and the mode temperature of this sample's RBM was determined using a displacement measurement based on the PDH technique (see section 4.2.3). To enhance the sensitivity, the weak probing light ($< 2 \mu\text{W}$) from the employed low-noise fiber laser (BASIK, Koheras) was am-

plified using an erbium-doped amplifier after leaving the cryostat, allowing us to measure displacement spectra down to the base temperature of the cryostat (Arcizet et al. (2009)). In figure 45, the mode temperature T_m extracted from the calibrated spectra is shown to closely follow the temperature of the helium buffer gas down to about 1.8 K, or $\langle n \rangle \approx 600$. In spite of being exclusively in contact with the cold helium gas, this 62 MHz-RBM could therefore be thermalized to occupation numbers which are, for lower frequency oscillators, often only attainable in dilution refrigerator systems.

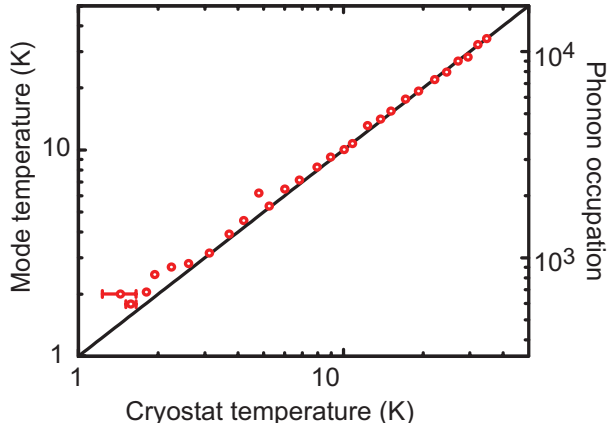


Fig. 45. Thermalization of the 62 MHz-RBM of a silica microtoroid. The mode temperature T_m follows the temperature of the helium buffer gas down to 1.8 K, or $\langle n \rangle \approx 600$, proving the effectiveness of the buffer gas cooling. Figure from ref. (Schliesser et al. (2009)).

Cryogenic cooling of the silica microresonators implies severe modifications of the properties of these devices. As discussed already in section 3.2.4, the mechanical quality factor critically depends on the temperature of the structure, due to coupling of the mechanical modes to two-level systems in the glass. In contrast, the change in the sound velocity, and therefore the mechanical resonance frequencies, is a relatively weak effect at the $\mathcal{O}(10^{-2})$ -level (Arcizet et al. (2009)). At the same time, the thermorefractive (dn/dT) and thermoelastic (α) coefficients are strongly modified. While α tends to zero at low temperatures ($T < 2 \cdot 10^{-9} \text{ K}^{-1}$ at 1.6 K), the thermorefractive coefficient continuously drops and changes sign at a temperature of about 8 K.¹³ The resulting non-trivial temperature dependence of the optical resonance frequency gives rise to interesting thermal multistability effects when an optical resonance is probed using a laser powerful enough to heat the cavity above this temperature (Arcizet et al. (2009)). In the context of the cooling experiments, it is important to note that negative dn/dT implies that the red wing of an optical resonance is dynamically self-stable, relaxing dramatically the requirements on the laser frequency stability and locking speed when working with red detunings.

¹³Note these observations (Arcizet et al. (2009)) differ from a previous report (Treussart et al. (1998)).

7.1.2 *Optical system*

For a cooling experiment with the aim of reaching very low occupation numbers, it is mandatory to avoid excess backaction noise in the cooling laser beam, as this leads to a limit (Schliesser et al. (2008b); Diósi (2008); Rabl et al. (2009)) in the cooling performance. The grating-stabilized diode lasers employed in our previous cooling work was observed to exhibit excess frequency noise (cf. section 6.3). One possible strategy to eliminate this noise is to measure the noise using an independent, quiet cavity, and fast feedback on the frequency of the laser using e. g. the diode laser current as an actuator. Feedback with the required bandwidth exceeding 50 MHz however is technically difficult, as a few meters of cable alone would already induce phase lags in the loop sufficient to render it ineffective.

As an alternative approach, a quiet cavity could be used in transmission to filter out the noise. In this manner, reduction of phase noise by 85 dB has been demonstrated at 1 MHz Fourier frequency (Hald and Ruseva (2005)). However, the filtering reduces the available power by more than a factor of 5, so that the remaining available power of ~ 2 mW is problematically low for cooling experiments. At the same time, the complex filtering setup derogates one important asset of a grating-stabilized diode laser: its convenient, wide-range, and fast tunability.

For these reasons, we chose to use a solid-state pumped continuous wave titanium-sapphire (Ti:S) laser (Matisse TX, Sirah Lasertechnik), which combines very wide tunability (750 to 870 nm) with high output power (> 0.5 W) and quantum-limited noise in both amplitude and phase at the relevant Fourier frequencies. Figure 46 shows the schematic setup of this device. The laser is pumped with up to 6 W at 532 nm from a frequency-doubled diode-pumped solid-state laser (Millenia, Spectra Physics). The frequency of the laser is adjusted by a combination of intracavity filters: a Lyot birefringent filter narrows down the frequency range in which gain exceeds loss to a few hundred GHz, and a thin and a thick etalon, with free-spectral ranges of about 250 GHz and 20 GHz, respectively, single out one longitudinal mode of the laser to oscillate. Once the desired laser mode oscillates, electronic feedback loops are used to lock the etalons to keep their transmission maximum resonant with the laser mode. These loops are implemented by the controller of the laser and can be adjusted on a computer using an USB-interface.

Two mirrors mounted on piezo-electric transducers can then be used to fine-adjust the frequency of the laser. In particular, the “slow” transducer allows frequency scans up to about 60 GHz. The “fast” transducer, together with the intracavity electro-optic modulator, can be used for fast feedback to the laser frequency. In normal operation, these actuators are employed in a feedback-loop to lock the laser to an external, temperature-stabilized, ~ 30 cm-long

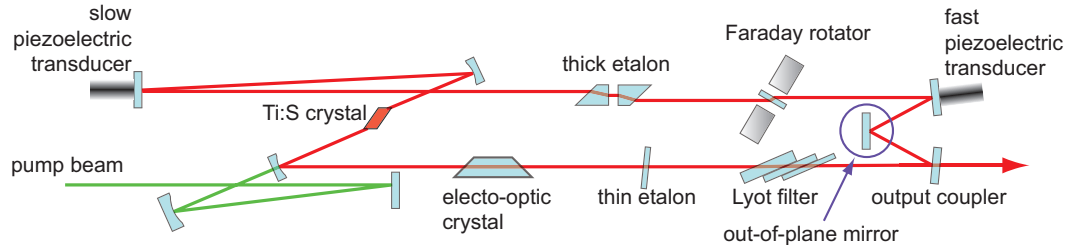


Fig. 46. Layout of the titanium-sapphire laser used for the cryogenic cooling experiments. The Ti:S crystal in the ring cavity is pumped optically at 532 nm (green beam). In order to select a single longitudinal mode within the tuning range of 750 to 870 nm (determined by the cavity mirrors), a Lyot filter, thick etalon and thin etalon are used. A Faraday rotator, one reflection point lying outside the plane of the rest of the cavity mode, and a number of Brewster-angled surfaces ensure unidirectional lasing action. The precise frequency of the laser can be actuated by displacing cavity mirrors using a fast, a slow piezo, as well as an intracavity electro-optic modulator.

high-finesse ($\mathcal{F} \sim 300$) cavity via the PDH technique, in order to eliminate low-frequency frequency noise of the laser, reducing the laser linewidth to < 30 kHz. In this case, the laser frequency is controlled by tuning the resonance frequency of the reference cavity, again by displacing a cavity mirror mounted on a piezoelectric transducer. The custom version of the laser set up in our laboratory allows alternatively to directly lock the laser to a WGM in a silica microtoroid, by feeding an error signal (derived using one of the above-described methods) to the laser controller.

The Ti:S laser can be tuned to arbitrary frequencies within its tuning range; however, continuous scanning over the whole range is not possible, as the various frequency selectors (Lyot and etalon filters) have to be readjusted if the laser has to be tuned by more than about 30 GHz. We therefore resort to a continuously tunable grating-stabilized diode laser (DL) in Littman-Metcalf configuration (TLB-6300, New Focus) for pre-characterization of the toroids (cf. figure 47). Once a well-suited WGM resonance is found with the DL, the Ti:S laser is tuned close to the frequency of this resonance.

For this purpose, the Ti:S frequency is coarsely adjusted first, using a grating spectrograph. For the subsequent fine-adjustment, it was found very useful to monitor the interference signal of the DL—scanning over a broader frequency range including the WGM resonance—and the slowly tuning Ti:S laser. When the DL scans through the Ti:S frequency, a transient interference signal is observed as long as the difference frequency is within the bandwidth of the receiver (125 MHz). This transient beat serves as a convenient marker of the Ti:S frequency, while the standard transmission signal of the DL indicates the WGM resonance frequency.

After the Ti:S has been tuned close to the WGM resonance, an optical switch

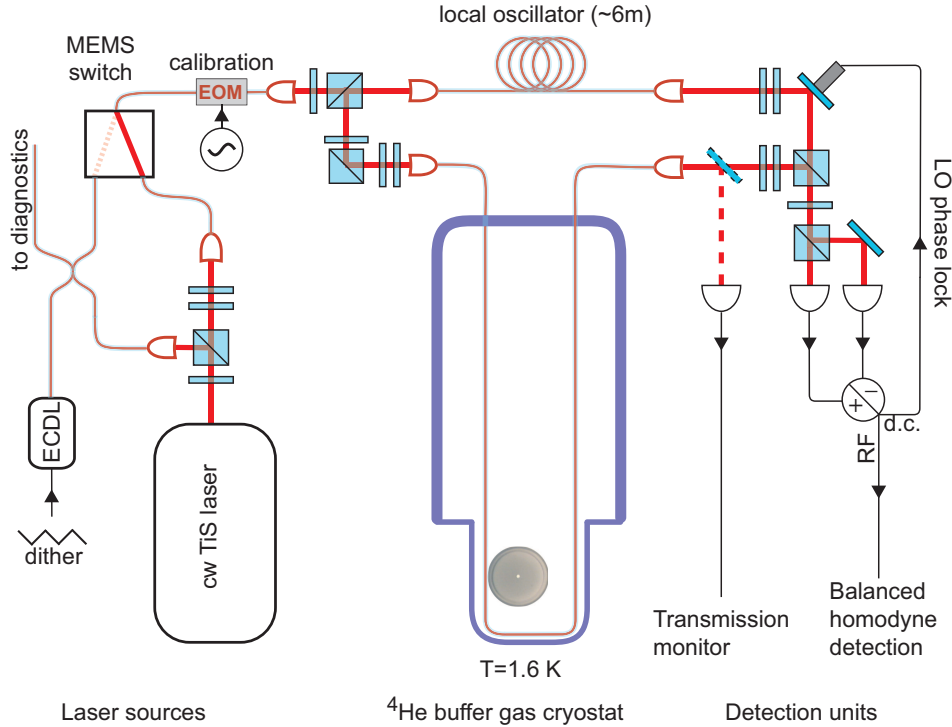


Fig. 47. Schematic of the setup used for resolved-sideband laser cooling in a cryogenic environment. An external cavity diode laser (ECDL) is used for precharacterization of the optical modes. When a suited WGM resonance is found, the Ti:S laser is tuned to the frequency of the ECDL using the “diagnostics” optical output (see text). Then the input to the experiment is switched to the Ti:S using a MEMS switch. The subsequent optical setup is essentially a Mach-Zehnder interferometer, one arm of which contains the cryostat with the taper coupled to the WGM in a microtoroid. For testing purposes, the output of the taper can also directly be monitored by guiding the light to an auxiliary photoreceiver (dashed beam path). In normal operation, the transmitted light is spatially overlapped with the local oscillator in a polarizing beam splitter cube, albeit in orthogonal polarization modes. Projected into a different polarization basis using a waveplate and another polarizing cube, the modes interfere, and the interference signal is recorded with a balanced receiver. The phase of the local oscillator—and therefore also the detected signal quadrature—is locked using the DC-signal from the balanced receiver. The radio-frequency-part is sent to a spectrum analyzer to obtain the displacement noise spectra, calibrated again by the frequency modulation of probing laser using an electro-optic modulator (EOM). Waveplates and polarizing beam splitter cubes are used at various positions in the optical setup to adjust powers and polarizations of the beams.

based on MEMS¹⁴-technology is used to switch to the Ti:S laser as input to the experiment. The optical setup of the experiment corresponds essentially to a homodyne measurement (figure 47). To achieve the highest possible SBR, good interference contrast between the local oscillator and signal beams is

¹⁴ MEMS: microelectromechanical system

crucial. For this reason, identical collimators in both beams are employed. Careful alignment then allowed to achieve interference contrast up to 90% (figure 48).

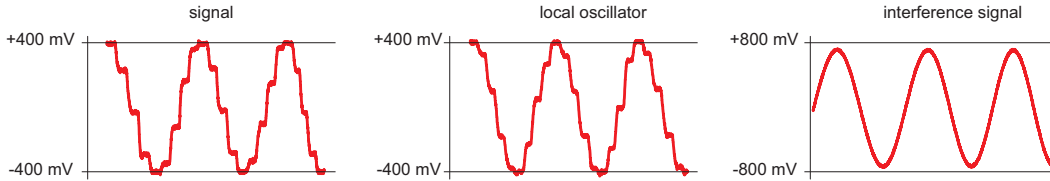


Fig. 48. Interference contrast of the homodyne receiver. “Signal” and “local oscillator” traces are recorded by manually rotating the last $\lambda/2$ -waveplate in front of the last polarizing beam splitter cube in steps of 10° , with the other input beam blocked. For this test, the powers in both beams are adjusted to yield a maximum signal of 400 mV. If both beams are opened, and the detection unit is properly aligned, a total signal amplitude of 1440 mV, corresponding to 90% interference contrast, is recorded.

The phase of the local oscillator is locked by using the DC-part of the homodyne signal from the balanced receiver, forcing the average detected differential photocurrent to zero for a phase measurement. Note that this is slightly different to the technique described in 4.2.1, where an orthogonal polarization component (in both signal and LO beams) was used to derive the LO phase error signal. In this experiment, the length of the employed fibers renders this approach problematic due to apparent drifts in the polarization rotation in the fibers. Note also that it is necessary to match the total length of the fibers in both arms of the interferometer (excluding the potential propagation length in the toroid) in order to measure the correct signal quadrature at all Fourier frequencies.

Figure 49 shows typical displacement spectra of the 65.3 MHz-RBM of a silica microtoroid probed by homodyne spectroscopy with the Ti:S laser. The sample is held in the cryostat, at a temperature of 2.4 K, corresponding to $\langle n \rangle \approx 770$. Sensitivity at the 10^{-18} m/ $\sqrt{\text{Hz}}$ -level, as well as a SBR of nearly 20 dB (in noise power) is achieved, in spite of a mechanical quality factor which was as low as 540 in this case. Note that displacement noise measured at resonance is the sum of the thermal noise in the mechanical mode *plus* the imprecision background noise due to quantum noise in the detection, which is reduced at higher probing powers.

7.2 Cooling towards the quantum ground state

To demonstrate the performance of combined optical and cryogenic cooling, we used a $52 \mu\text{m}$ -diameter sample with a WGM of 5.5 MHz intrinsic decay rate and 9 MHz mode splitting, loaded down to $\kappa/2\pi \approx 19$ MHz using the

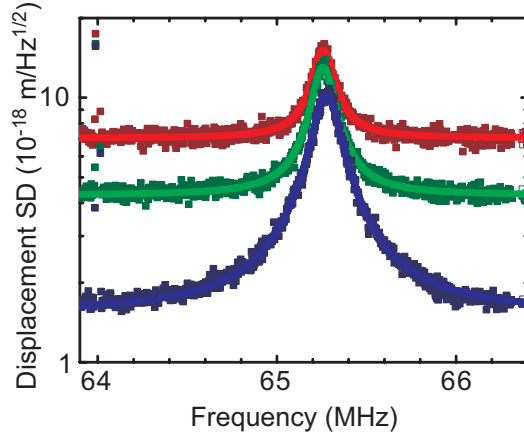


Fig. 49. Displacement noise spectra of the RBM of a silica microtoroid held at a temperature of 2.4 K. The power used to probe the RBM was about $3 \mu\text{W}$ (red trace), $10 \mu\text{W}$ (green trace) and $100 \mu\text{W}$ (blue trace). Points are measured data, lines are Lorentzian fits. Figure from ref. (Schliesser et al. (2009)).

fiber taper, corresponding to a finesse of about 70,000. A room-temperature reference measurement (figure 49) of its RBM at 65.2 MHz reveals an effective mass of 5.6 ng, in good agreement with the simulated value of 4.9 ng. Note that the experimentally determined mass can only be as accurate as is the displacement calibration and the knowledge of the actual temperature of the RBM. We generally estimate the resulting systematic error to a level of 30%, arising from imperfections in the modulation scheme and temperature changes induced by dynamical backaction or absorption-induced heating.

Using this effective mass, it is possible to derive the mode temperature from subsequent displacement measurements during cooldown of the cryostat. The results again confirm proper thermalization of the sample (figure 49), down to an occupation of $\langle n \rangle \approx 550$. For further cooling, the Ti:S laser is tuned to the lower sideband at $\bar{\Delta} = -\Omega_m$. The signal from the homodyne receiver can still be used to measure mechanical displacements, however, due to the detuned operation, the spectrum of the phase quadrature now displays a more complicated dependence from the mechanical noise spectrum. In contrast to the simple expression (118) for $\bar{\Delta} = 0$, we now obtain

$$\bar{S}_{qq}^{\text{out}}(\Omega) = 1 + \frac{4\bar{a}^2 g_0^2 \eta_c \kappa}{\bar{\Delta}^2 + (2\eta_c - 1)^2 (\kappa/2)^2} \times \frac{\bar{\Delta}^4 + 2\bar{\Delta}^2 (2\eta_c - 1) (\kappa/2)^2 + (2\eta_c - 1)^2 (\kappa/2)^2 ((\kappa/2)^2 + \Omega^2)}{\bar{\Delta}^4 + 2\bar{\Delta}^2 ((\kappa/2)^2 - \Omega^2) + ((\kappa/2)^2 + \Omega^2)^2} \bar{S}_{xx}(\Omega), \quad (180)$$

where the first term, equal to unity, again is due to quantum noise. Importantly, the transduction of a frequency modulation into \bar{S}_{qq} has the same dependence on the relevant experimental parameters as the transduction of

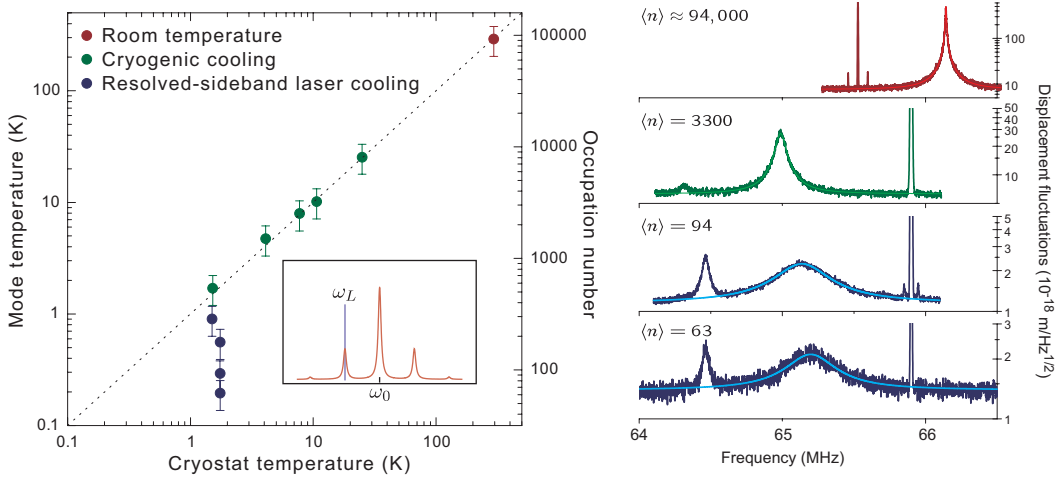


Fig. 50. Left panel: Mode temperature and occupation number of the RBM, measured using noise thermometry, versus the temperature of the buffer gas in the cryostat, including a reference measurement at room temperature (red point). Green data points are taken with the laser tuned to the optical resonance, so no optical cooling takes place. When tuned to the lower mechanical sideband (inset), additional laser cooling is observed (blue points). Panels on the right show a selection of displacement noise spectra, from which the mode temperatures of the measurements were derived. Apart from the calibration peak these spectra also reveal a nearby second mechanical mode. Nonetheless, the spectrum of the RBM can be well-fit with a Lorentzian (thin lines). Figure from ref. (Schliesser et al. (2009)).

displacements \bar{S}_{xx} , so that the calibration scheme remains valid also in the detuned case.

Rewriting equation (180) as a quantum-noise induced imprecision in the displacement measurement one obtains

$$\bar{S}_{xx}^{\text{im,qn}}(\Omega) = \frac{\bar{\Delta}^2 + (2\eta_c - 1)^2(\kappa/2)^2}{4\bar{a}^2 g_0^2 \eta_c \kappa} \times \frac{\Delta^4 + 2\bar{\Delta}^2((\kappa/2)^2 - \Omega^2) + ((\kappa/2)^2 + \Omega^2)^2}{\bar{\Delta}^4 + 2\bar{\Delta}^2(2\eta_c - 1)(\kappa/2)^2 + (2\eta_c - 1)^2(\kappa/2)^2((\kappa/2)^2 + \Omega^2)}. \quad (181)$$

For $\kappa \gg \Gamma_{\text{eff}}$, which is typically in the case in the experiments presented here, the spectral shape of this function can be assumed to be flat over the frequency range of interest, and we find as a useful approximation

$$\bar{S}_{xx}^{\text{im,qn}}(\Omega_m) \approx \frac{\Omega_m^2}{4\eta_c^2 g_0^2} \frac{\hbar\omega}{P_{\text{in}}} \quad (182)$$

in the resolved sideband regime ($\bar{\Delta} = -\Omega_m \gg \kappa$). It is noteworthy that this value is only a factor of 4 higher than expected for resonant probing $\bar{\Delta} = 0$ in this regime. However, in the resolved sideband regime, only a fraction of

$\sim (\kappa/4\Omega_m)^2$ of the launched power is coupled to the cavity.

Figure 50 shows displacement spectra and corresponding mode temperatures recorded during such a cooling run. As expected, the damping of the mechanical modes is optically increased, when the laser is detuned to $\bar{\Delta} = -\Omega_m$. Note that for these experiments, active stabilization of the laser frequency to the optical sideband of the WGM has not been necessary. Instead, a second electronic spectrum analyzer was used to demodulate the homodyne signal at the frequency Ω_{mod} of the calibration modulation. As expected from equation (181), this signal displays local maxima at $\bar{\Delta} = 0, \pm\Omega_{\text{mod}}$. After the laser is tuned to $\bar{\Delta} = -\Omega_m$, the system is sufficiently stable during the averaging of typically several tens of seconds (small drifts can be manually compensated).

For the highest launched powers of ~ 0.2 mW, the total damping rate was increased to $\Gamma_{\text{eff}}/2\pi = 370$ kHz. At the same time, the mode temperature was reduced to $T_m = 200 \pm 60$ mK, corresponding to an occupation number of $\langle n \rangle = 63 \pm 20$ (Schliesser et al. (2009)). The error interval is due to potential calibration errors in the displacement measurement and the determination of the effective mass. This value is comparable to the lowest occupation number achieved in nanoelectromechanical systems, yet those experiments have to rely more heavily on advanced cryogenic machinery (Naik et al. (2006)), and suffer from the insufficient signal-to-noise ratio.

7.3 Assessing measurement backaction

The strong suppression of thermal noise in the measurements presented here allows an interesting analysis of the data from the perspective of quantum measurement (Braginsky and Khalili (1992)). As discussed in section 4.1, fundamentally, the achieved total uncertainty in the measurement of the displacement of the mechanical oscillator is limited by two effects: imprecision and backaction. The imprecision in our experiment is given by detection shot noise, in the detuned case discussed here it is described by equation (181).

On the other hand, the light used to measure the mechanical oscillator exerts backaction on it. Inevitably, intracavity photon number fluctuations give rise to a fluctuating force, the spectrum of which can be derived as (Schliesser et al. (2009))

$$\bar{S}_{FF}^{\text{ba,qn}}(\Omega) = \hbar^2 g_0^2 \bar{a}^2 \kappa \frac{\bar{\Delta}^2 + (\kappa/2)^2 + \Omega^2}{\bar{\Delta}^4 + 2\bar{\Delta}^2((\kappa/2)^2 - \Omega^2) + ((\kappa/2)^2 + \Omega^2)^2}. \quad (183)$$

These force fluctuations are usually referred to as quantum backaction, sim-

plifying to

$$\bar{S}_{FF}^{\text{ba,qn}}(\Omega_m) \approx \frac{2g_0^2 P_{\text{in}} \eta_c \hbar}{\omega \Omega_m^2} \quad (184)$$

in the resolved-sideband regime ($|\bar{\Delta}| = \Omega_m \gg \kappa$). Note that the spectra of imprecision and backaction noise, as well as their possible correlation $S_{xF}(\Omega)$ reflect properties of the measurement device (the cavity pumped by a laser field)—independent of the mechanical oscillator.

Other sources of measurement backaction include excess noise in the intracavity photon number, which may arise from laser frequency fluctuations (Schliesser et al. (2008b); Diósi (2008); Rabl et al. (2009)). This effect can be ruled out in this work as the employed Ti:S is known to exhibit only quantum fluctuations at the Fourier frequencies of interest. Another possible source of measurement backaction is heating of the torus due to light absorption. This increases the temperature of the structure, and raises the level of Langevin force fluctuations driving the mechanical oscillator.

A series of cooling measurements (figure 51) indeed reveals a deviation from the simple relation (147), which can however be reproduced by introducing a heating term

$$T_m = \frac{\Gamma_m(T')}{\Gamma_m(T') + \Gamma_{\text{dba}}} T', \quad (185)$$

with $T' = T + \Delta T_{\text{abs}}$, where ΔT_{abs} is proportional to the power circulating in the cavity. In addition, we have taken also the temperature dependence of the mechanical damping $\Gamma_m(T')$ into account. For the 65 MHz-oscillator below 2 K, with (Arcizet et al. (2009)) $d\Gamma_m/dT \approx 2\pi 16 \text{ kHz/K}$, we find a heating of about 5 K per Watt of circulating power. Similar values were extracted from studies of optical multi-stability at low temperature at a wavelength of $1.5 \mu\text{m}$, corroborating the attribution of the observed backaction effect to laser-induced heating.

A comparison with a second cooling run with a different sample with $\Omega_m/2\pi = 121.7 \text{ MHz}$ and $Q_m = 2,200$, but a broader WGM resonance ($\kappa/2\pi = 155 \text{ MHz}$) emphasizes the importance of the resolved-sideband regime for the efficiency of cooling in the presence of laser absorption: A significantly more pronounced heating effect prevents reaching occupation numbers below $\langle n \rangle = 100$, in spite of the higher mechanical frequency (figure 51).

From the data of the $\langle n \rangle \approx 63$ -cooling run we can now extract quantitative values of the corresponding backaction force fluctuations. As a very conservative upper limit, we may use the *total* thermal force fluctuations $\bar{S}_{FF}^{\text{the}}(\Omega) = 2m_{\text{eff}}\Gamma_m k_B T'$, and find a value of $\sqrt{\bar{S}_{FF}^{\text{the}}(\Omega_m)} = 8 \text{ fN}/\sqrt{\text{Hz}}$. If we consider only the temperature *rise* ΔT_{abs} caused by the laser absorption as

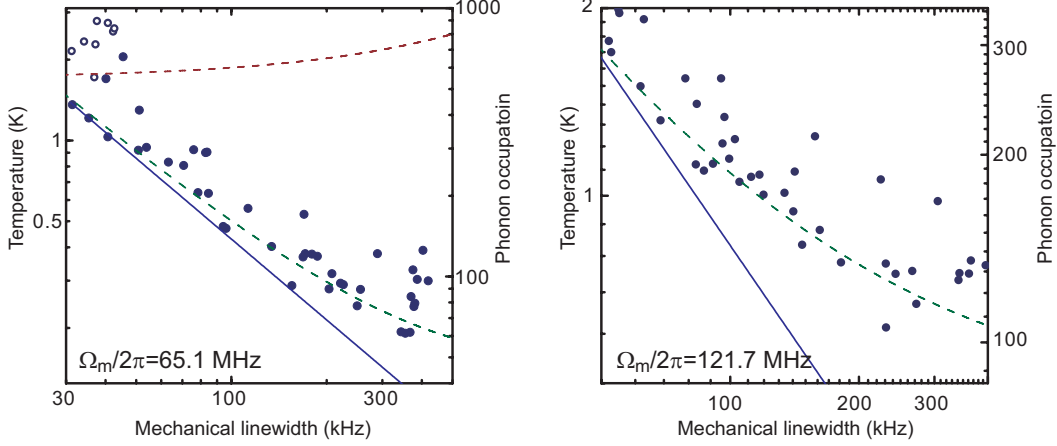


Fig. 51. Resolved-sideband cooling of two samples with frequencies of $\Omega_m/2\pi = 65.1$ MHz (left panel) and $\Omega_m/2\pi = 121.7$ MHz (right panel). The graphs show the mechanical linewidth Γ_{eff} (abscissa) versus the derived mode temperature T_m (ordinate) during a cooling run. Open points correspond to measurements with the laser tuned close to the optical resonance (no optical cooling), and filled points to measurements with the laser tuned close to the lower sideband. When varying the power of the cooling laser, both linewidth and mode temperature are changed. Deviation from the simple cooling behavior (blue line) is attributed to an increase of the structures' temperature (red dashed line), taken into account in a more elaborate model (green dashed line). Scatter is due to varying operation conditions, uncertainty in phonon occupation for each point is $< 30\%$. Figure from ref. (Schliesser et al. (2009)).

the backaction of the measurement, a lower value of $\sqrt{\bar{S}_{FF}^{\text{ba}}(\Omega_m)} = 4 \text{ fN}/\sqrt{\text{Hz}}$ is found. In these assessments, we benefit from the low occupation which allows us to extract the effect of measurement backaction, as it is large enough to be observed on top of the background of the thermal noise.

It is interesting to compare these findings with fundamental limits. Quantum mechanics imposes an inequality on imprecision and backaction noise, which, for the particular case of an optical measurement of a mechanical oscillator's displacement, can be written as (Braginsky and Khalili (1992))

$$\bar{S}_{xx}^{\text{im}}(\Omega) \cdot \bar{S}_{FF}^{\text{ba}}(\Omega) \geq \frac{\hbar^2}{4}. \quad (186)$$

This relation can be considered a manifestation of the Heisenberg uncertainty principle in the context of continuous position measurement (Braginsky and Khalili (1992)).

Taking the force noise extracted from our data, and the experimental imprecision of $\sqrt{\bar{S}_{xx}^{\text{im}}(\Omega_m)} \approx 1.4 \text{ am}/\sqrt{\text{Hz}}$ achieved in the same measurement, an upper limit from the backaction-imprecision product of $\sqrt{\bar{S}_{xx}^{\text{im}}(\Omega_m) \cdot \bar{S}_{FF}^{\text{the}}(\Omega_m)} \approx$

$220 \hbar/2$ is found. Considering only the absorption-induced heating as a back-action mechanism, an even lower value of $\sqrt{\bar{S}_{xx}^{\text{im}}(\Omega_m) \cdot \bar{S}_{FF}^{\text{ba}}(\Omega_m)} \approx 100 \hbar/2$ is found from our experiments. This is an order of magnitude lower than the values achieved with nanomechanical oscillators cooled in dilution refrigerators: Readout with an atomic point contact (Flowers-Jacobs et al. (2007)) achieved a backaction-imprecision product of $1700 \pm 400 \hbar/2$, while measurements using a superconducting single-electron transistor (Naik et al. (2006)) have achieved a value¹⁵ of $\sim 800 \hbar/2$.

¹⁵Note that the number quoted in this manuscript, $15 \hbar/2$, is a theoretical estimate if shot-noise limited detection was possible. As discussed in the supplementary information, the actual imprecision noise in the experiment was 50-times higher (Naik et al. (2006); Clerk et al. (2008)).

8 Conclusion

In this chapter, we have reported on optomechanical interactions in high-finesse optical whispering gallery mode resonators. Careful analysis and understanding of these devices' properties has allowed us to optimize their performance for the purpose of cavity optomechanics. Among the various systems now designed and studied in this context, they offer a unique combination of high-frequency (30–120 MHz), high-quality (Q_m up to 80,000) mechanical modes and ultra-high finesse (intrinsic finesse $\mathcal{F}_0 \approx 0.9 \cdot 10^6$) optical resonances. These key figures rival even the best optical cavities developed in the context of cavity quantum electrodynamics (Rempe et al. (1992)) in terms of finesse, and the mechanical quality factors of state-of-the art nano- and micromechanical oscillators (Naik et al. (2006); Verbridge et al. (2007)) in the same frequency range.

Together with an intrinsically strong parametric coupling of optical and mechanical degrees of freedom—with optical resonance frequency shifts of typically more than 10 kHz per femtometer displacement—this has enabled ultrasensitive optical monitoring of the mechanical mode. Adapting powerful tools from quantum optics as optical displacement meters limited only by optical quantum noise, sensitivities at the level of $10^{-18} \text{ m}/\sqrt{\text{Hz}}$ were achieved (Schliesser et al. (2008b,a)). This experimentally demonstrated imprecision is below the expected noise level associated with the zero-point fluctuations of the mechanical mode, which so far has been achieved only with much lighter nanomechanical oscillators (Naik et al. (2006); Clerk et al. (2008)). Reaching such a sensitivity is a crucial precondition for the experimental verification of the concepts of quantum measurement in the context of displacement measurements, such as quantum backaction and the emergence of the standard quantum limit (Braginsky and Khalili (1992); Tittonen et al. (1999); Schwab and Roukes (2005)). Furthermore, this exquisite sensitivity (Schliesser et al. (2008a)) may also be exploited to monitor nanomechanical oscillators brought into the near-field of the cavity mode, such as silicon nitride nanobeams or -membranes (Anetsberger et al. (2009)), graphene sheets or diamond nanowires. Beyond mechanical effects, this sensitivity has allowed us to study fundamental thermal noise mechanisms, such as thermorefractive noise, which are of interest for the application of silica microresonators as frequency references (Vassiliev et al. (1998); Matsko et al. (2007)), as biophysical sensors (Armani et al. (2007); Schröter et al. (2008); Vollmer et al. (2009)) or for the proposed demonstration of Kerr squeezing (Kippenberg et al. (2004)).

Due to the high-finesse, the dramatically enhanced intracavity radiation pressure exerts a readily detectable force on the mechanical mode. This effect was directly measured in a “pump-probe”-type measurement, in which the displacements induced by modulated radiation-pressure is probed with a second

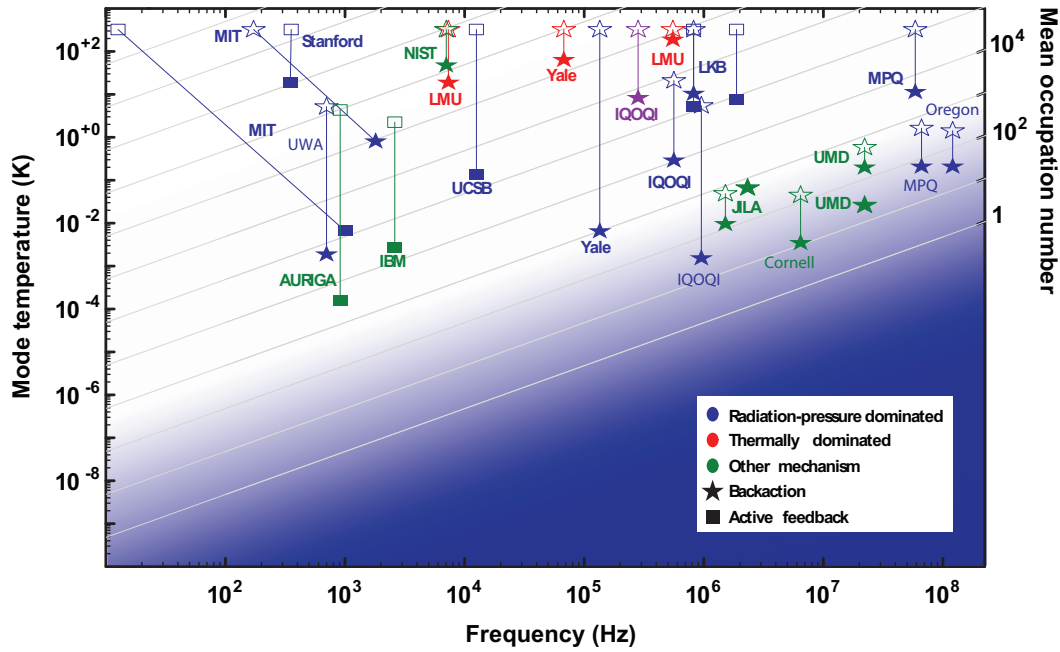
laser. It was shown that the nonlinear cross-coupling of the two light fields is strongly dominated by radiation pressure induced mechanical displacement, and more than two orders of magnitude stronger than the well-known Kerr effect (Schliesser et al. (2006)). Furthermore, radiation pressure has also been shown to induce a modification of the dynamics of the mechanical mode, changing both its effective spring constant (optical spring) and its damping (amplification and cooling). Predicted as early as 1967 by Braginsky (Braginskii and Manukin (1967)), this dynamical backaction was systematically studied over a wide regime of experimental parameters (detuning, photon storage time, mechanical oscillation period). Our experiments have demonstrated, for the first time, efficient optical cooling of a mechanical mode induced by dynamical backaction, both in the “Doppler” (Schliesser et al. (2006)) and the resolved-sideband regime (Schliesser et al. (2008b)). These techniques are now widely employed in experiments which aim to demonstrate ground-state cooling of a mechanical device (figure 52).

In our experiments, we have identified several important barriers on the way towards this ultimate goal. Frequency noise of the driving electromagnetic field, practically relevant in many systems (Schliesser et al. (2008b); Diósi (2008); Rabl et al. (2009)), is shown here to be eliminated by resorting to a quantum-noise limited laser system. Furthermore, much in contrast to trapped atoms or ions, even very high-Q macroscopic oscillators are not very well isolated from their finite-temperature environment. Fluctuating thermal forces thus compete with laser cooling, limiting the occupancies achieved in room-temperature experiments to a few thousand quanta (figure 52).

To overcome this limit, we have implemented resolved-sideband laser cooling in a cryogenic environment (Schliesser et al. (2009)). The mechanical oscillator is cooled to an occupation number of $\langle n \rangle \approx 63 \pm 20$. The optical detection scheme provides small enough displacement imprecision to enable monitoring even such an ultracold oscillator with appreciable signal-to-noise ratio. Additionally, due to the low occupation number, we are able to extract an upper limit on the *backaction* of the displacement measurement. The product of backaction and imprecision noise lies only a factor of 100 above the fundamental quantum limit (Braginsky and Khalili (1992)), and constitutes the lowest value reported in the literature (Clerk et al. (2008)).

In conclusion, we have introduced an optomechanical system suited for the exploration of quantum effects in mesoscopic mechanical oscillators, by experimentally demonstrating *(i)* the possibility to monitor its displacements with an imprecision below the standard quantum limit, *(ii)* a combination of cooling techniques based on radiation-pressure and standard cryogenics capable of cooling the oscillator close to its quantum ground state, and *(iii)* a near-ideal operation of the displacement transducer in the sense of quantum measurement (imprecision-backaction product). Leveraging quantum optical

Fig. 52. Cooling experiments performed in different laboratories around the globe, including both experiments based on dynamical backaction and active feedback cooling. The cooled oscillators span about 8 orders of magnitude in frequency. Open symbols indicate the reservoir temperature of the experiments, distinguishing cryogenic from room-temperature experiments. Full symbols indicate the lowest mode temperature achieved when optomechanical cooling is applied. The dashed line indicates the temperature for which $\hbar\Omega_m \approx k_B T$. The individual results are described in references: AURIGA (Vinante et al. (2008)), Cornell (Hertzberg et al. (2009)), IBM (Poggio et al. (2007)), IQOQI (Gigan et al. (2006); Gröblacher et al. (2008, 2009b)), JILA (Teufel et al. (2008)), LKB (Cohadon et al. (1999); Arcizet et al. (2006b,a)), LMU (Höhberger Metzger and Karrai (2004); Favero et al. (2007)), MIT (Corbitt et al. (2007a,b)), MPQ (Schliesser et al. (2006, 2008b, 2009)), NIST (Brown et al. (2007)), Oregon (Park and Wang (2009)), Stanford (Weld and Kapitulnik (2006)), UCSB (Kleckner and Bouwmeester (2006)), UMD (Naik et al. (2006)), UWA (Mow-Lowry et al. (2008)), Yale (Thomson et al. (2008)).



techniques, we have therefore established a route into the quantum realm of mesoscopic oscillators, which previously was thought to be uniquely accessible with nano-electromechanical systems (Schwab and Roukes (2005)).

9 Outlook

Notwithstanding such progress, true quantum effects of radiation pressure and the quantum states of a mechanical oscillator have not been observed in any experiment today.¹⁶ In our experiments involving WGM microresonators, it appears that cooling to the quantum ground state, and the observation of quantum backaction are closest to fruition. In the following, we briefly outline the strategies pursued in our laboratory to achieve these goals, and, concluding this chapter, point to other interesting optomechanical effects.

The most severe antagonist to ground state cooling is the intrinsic damping Γ_m of the mechanical mode, coupling it to the environment at a finite temperature T . This coupling tries to maintain the mode and the environment in thermal equilibrium, essentially feeding the power $\Gamma_m k_B(T - T_m)$ into the mechanical mode, which has to be continuously removed by laser cooling. There are two obvious ways to reduce this load: reducing the environment temperature T , and reducing the mechanical damping Γ_m . While the former is a technical task, the latter exhibits complex dependence on material, geometry and operating conditions.

In particular we have observed (sections 3.2.4 and 7.2) a strong increase of the mechanical damping at cryogenic temperatures due to relaxation of two-level systems (TLS) present in silica material (Pohl et al. (2002); Arcizet et al. (2009)). This flaw is known, however, to ameliorate at sufficiently low temperatures $\lesssim 1$ K, at which the damping due to TLS falls off with $\Gamma_m \propto \Omega_m/T^3$. Thus, lowering the operating temperature of the experiment may be expected to enhance the cooling performance with a scaling up to T^{-4} . For this reason, a ^3He -cryogenic system is presently being tested in our laboratory. A base temperature of 600 mK and significantly higher mechanical quality factors ($> 10^4$) than in the ^4He -cryostat were already measured. Resolved-sideband cooling, with the cooling rates of 1.5 MHz already demonstrated, would place a 70 MHz RBM directly in the quantum ground state. A very crucial issue in this context, however, is the suppression of heating by laser absorption, requiring very high-quality samples and operation deeply in the resolved sideband regime.

Optical absorption could be reduced by using ultrapure crystalline materials for the WGM resonators. Indeed, pioneering work at the Jet Propulsion Laboratory has resulted in WGM resonators made of quartz (?), MgF_2 and CaF_2 (Grudin et al. (2006)) having optical quality factors up to $6 \cdot 10^{10}$. Machining and polishing WGM resonators down to a diameter of $80 \mu\text{m}$ has also been achieved. At the same time, the pristine crystalline structure avoids me-

¹⁶ There are, however, experiments that could be considered “quantum simulations” of mesoscopic mechanical oscillators—based on ultracold atoms (Murch et al. (2008); Brennecke et al. (2008)).

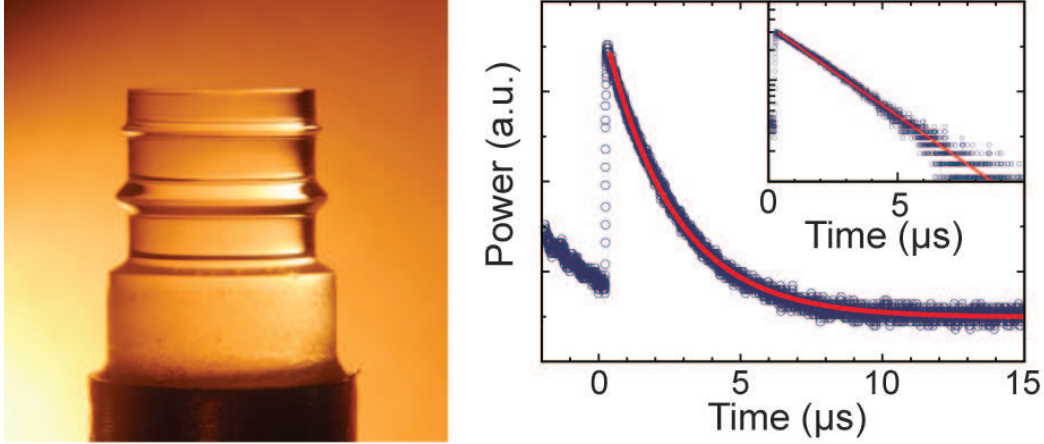


Fig. 53. Whispering gallery mode resonator made of calcium fluoride. The rims of the protrusions support WGM with extreme photon storage times. Left panel is a photograph of a 6 mm-diameter prototype resonator produced at MPQ. Right panel shows a ringdown trace for a critically coupled resonator. The ringdown time of $2.5 \mu\text{s}$ corresponds to an intrinsic quality factor of $1.2 \cdot 10^{10}$ (Hofer et al. (2009)).

chanical losses due to two-level systems. At ~ 100 kHz-frequencies, mechanical quality factors $Q_m \gtrsim 10^8$ were measured in bulk CaF_2 samples, both at room and cryogenic temperatures (Nawrodt et al. (2007)).

We have therefore started to explore the optomechanical properties of crystalline WGM resonators in our laboratory. Several different geometries were fabricated using a precision lathe and polished using diamond slurry. An example of such a resonator is shown in figure 53. We have achieved optical quality factors up to $Q_0 = 1.2 \cdot 10^{10}$, corresponding to a linewidth of $\kappa/2\pi = 24$ kHz in a $R = 1.8$ mm resonator (intrinsic Finesse $\mathcal{F}_0 = 760,000$). We have also produced an $800 \mu\text{m}$ -diameter, $100 \mu\text{m}$ thick disk and achieved $Q_0 \approx 10^9$ ($\mathcal{F}_0 = 400,000$). Optical transduction techniques described in section 4 are used to measure mechanical modes in these structures, which are typically found in the range between 0.5 and 5 MHz. The highest measured mechanical quality factor was $Q_m = 136,000$. Already an encouraging value, there is strong evidence for this value to be still limited by clamping losses which can be mitigated by a more suitable design and suspension of the resonators. Furthermore, the rather high effective masses (around $600 \mu\text{g}$) and the slightly weaker optomechanical coupling ($|g_0|/2\pi \sim 1.5$ kHz/fm) call for further miniaturization of the structures. For example, a $80 \mu\text{m}$ -diameter, $10 \mu\text{m}$ thick disk would possess $m_{\text{eff}} = 90$ ng and $\Omega_m/2\pi = 63$ MHz. If $Q_m \sim 10^8$ can be reached, the power required to cool such a device from $T = T_m = 1.6$ K to $T_m \approx \hbar\Omega_m/k_B$ is as low as $10 \mu\text{W}$ in the resolved-sideband regime. Heating due to absorption is likely to be totally negligible considering the optical quality of the crystals.

We finally point out that many other crystalline materials may be amenable to this approach, combining optomechanical coupling with yet other function-

ality. As an example, we have tested various polished diamond spheres, and have observed WGMs with quality factors up to $3 \cdot 10^6$ in a 3 mm-diameter sphere.

A somewhat opposite approach consists in decoupling optical and mechanical degrees of freedom. Keeping the silica WGM resonators as optical cavities, but placing an external mechanical oscillator in the near-field of the WGM allows for independently engineered mechanical properties. For example, light-weight ($m_{\text{eff}} \approx 1$ pg) nanomechanical oscillators such as strained SiN strings, have been shown to result in $Q_m \approx 10^6$ at ~ 1 MHz-resonance frequencies (Verbridge et al. (2008)). Placed in the near-field of a WGM, movement of the polarizable oscillator in the optical field gradient induces frequency shifts on the order of $|g_0| \approx 10$ MHz/nm, without inducing detectable optical loss of the WGM. A measurement imprecision below the noise level associated with zero-point fluctuations and dynamical backaction induced by the optical dipole force have been demonstrated with such a system in our laboratory (Anetsberger et al. (2009)).

These results are very encouraging for studies pertaining to the observation of quantum backaction. Usually masked by the much stronger thermal noise, this effect may become detectable if the ratio $\bar{S}_{FF}^{\text{ba,qn}}(\Omega_m)/\bar{S}_{FF}^{\text{the}}(\Omega_m) \approx \bar{a}^2 g_0^2 \kappa \hbar^2 \Omega_m^{-2} / 2m_{\text{eff}} \Gamma_m kT$ (assuming the limit $\Omega_m \gtrsim \kappa/2$) approaches unity. Leveraging the low mass and high quality factor available with nanomechanical oscillators, it appears feasible to approach this regime, with moderate optical probing powers of $\sim 100 \mu\text{W}$ even *at room temperature*. To differentiate the added noise induced by quantum backaction from potentially present absorption induced heating, correlation measurements (Verlot et al. (2008)) or backaction cancellation (Caniard et al. (2007b)) between two oscillators with slightly different frequencies may be employed.

A final example of near-future research projects enabled by the progress presented in this thesis is an investigation of the regime of strong optomechanical coupling (Dobrindt et al. (2008)) in the yet unexplored optical domain. As our analysis shows, the strong—but tunable—coupling of the optical mode to the mechanical mode via the mean photon field \bar{a} gives rise to features very similar to the effect of electromagnetically induced transparency (EIT) in atomic physics (Zhang et al. (2003); Fleischhauer et al. (2005)).

The basic idea of such an experiment is illustrated in figure 54. The strong field \bar{a} of the coupling (formerly “cooling”) laser oscillates at frequency $\omega_1 = \omega_c - \Omega_m$, and thereby couples the levels $2 \leftrightarrow 3$ by processes in which a phonon is removed upon the addition of a photon to the intracavity field (red-sideband transitions). A second, very weak laser oscillating at $\omega_p = \omega_1 + \Omega$, probes “carrier” transitions $1 \leftrightarrow 2$, in which originally no phonons are added or removed. Due to the strong optomechanical coupling induced by the coupling

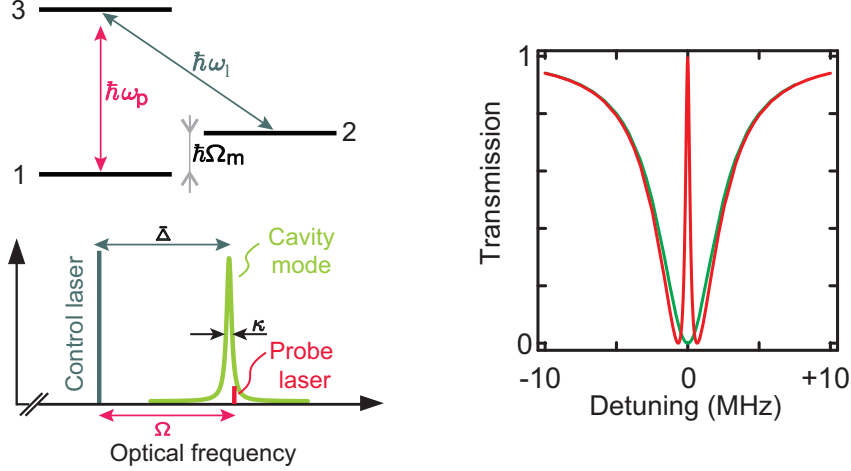


Fig. 54. Optomechanically induced transparency. Left: A coupling laser of frequency ω_1 drives red sideband transitions between (sets of) levels 2 and 3, which differ both in the number of optical and mechanical excitation quanta (each time a photon is added to the coupling field, a phonon in the mechanical degree of freedom is removed). A probing laser tuned close to the $1 \rightarrow 3$ transition of the unperturbed systems actually interacts with a superposition of levels 2 and 3, leading to the opening of a transmission window in the case of an optomechanical system. Right panel shows the resulting power transmission of the probe laser through a taper-toroid system for $\bar{\Delta} = -\Omega_m$ versus the detuning $(\Omega - \Omega_m)/2\pi$ of the probe laser. Numerical parameters are typical for silica microtoroids, with $\Omega_m/2\pi = 40$ MHz, $\Gamma_m/2\pi = 1.3$ kHz, $\kappa/2\pi = 5$ MHz, $R = m_{\text{eff}} = 10$ ng, $R = 40$ μm and $\bar{s}_{\text{in}}^2 \hbar\omega_1 = 300$ μW (red line) or $\bar{s}_{\text{in}}^2 \hbar\omega_1 = 0$ μW (green line).

field, it effectively interacts with a hybrid optomechanical resonance. Similar to EIT, this hybridization opens up a *tunable* transmission window for the probing laser at the center of the optical resonance. We therefore refer to this effect as “optomechanically induced transparency”.

A simple model for this scheme can be set up directly from the Langevin equations (50)–(52). Neglecting thermal and quantum noise for an elementary analysis, one obtains for the (power) transmission of the probing laser

$$T_p = \left| 1 - \frac{1 + if(\Omega)}{-i(\bar{\Delta} + \Omega) + \kappa/2 + 2\bar{\Delta}f(\Omega)} \eta_c \kappa \right|^2 \quad (187)$$

with

$$f(\Omega) = \hbar g_0^2 \bar{a}^2 \frac{\chi(\Omega)}{i(\bar{\Delta} - \Omega) + \kappa/2}. \quad (188)$$

At a basic level, this effect can be understood from the fact that for $\omega_p - \omega_1 = \Omega \approx \Omega_m$, the beat of coupling and probing laser drives the mechanical oscillator. The anti-Stokes field generated, in turn, from the coupling field

interferes with the incoming probing light.

The formal analogy with atomic EIT is even more obvious in the limiting case of: *(i)* a high- Q oscillator $\Omega_m \gg \Gamma_m$ *(ii)* the resolved-sideband regime $\Omega_m \gg \kappa$ and *(iii)* the detuning $\bar{\Delta} = -\Omega_m$. Using the abbreviation $\Delta' \equiv \Omega - \Omega_m$ one can then simplify the equation system to

$$(-i\Delta' + \kappa/2) \delta\hat{a}(\Omega) = +ig_0\bar{a}\delta\hat{x}(\Omega) + \sqrt{\eta_c\kappa} \delta\hat{s}_{\text{in}}(\Omega) \quad (189)$$

$$(-i\Delta' + \Gamma_m)\delta\hat{x}(\Omega) = i\frac{\hbar g_0\bar{a}}{m_{\text{eff}}\Omega_m}\delta\hat{a}(\Omega) \quad (190)$$

directly analogous to the EIT case (Milonni (2005)), with the well-known solution

$$\delta\hat{a}(\Omega) = \frac{\eta_c\kappa}{(-i\Delta' + \kappa/2) + \frac{2\bar{a}^2 g_0^2 x_{\text{ZPF}}^2}{i\Delta' + \Gamma_m}}. \quad (191)$$

Mechanical and optical oscillator play the role of two dipole transitions, where a pump laser couples two of the involved three levels. As in EIT, the modification of the transmission for the probe laser may be used for tuning optical group velocities to generate slow or fast light (Kash et al. (1999); Hau et al. (1999); Milonni (2005)), or, in designs hosting large arrays of optomechanical systems, even storage of light in mechanical states (Fleischhauer and Lukin (2000); Liu et al. (2001); Phillips et al. (2001)) may be envisioned.

Acknowledgements

We are grateful to many people for their contributions to the work presented in this chapter. In particular, we would like to thank our collaborators Olivier Arcizet, Rémi Rivière, Georg Anetsberger, Johannes Hofer and Stefan Weis for their experimental and theoretical contributions, and Thomas Becker and Jörg Kotthaus for infrastructure support. We are indebted to Nima Nooshi, Ignacio Wilson-Rae and Wilhelm Zwerger for their input on theoretical aspects of this work. We also benefited from stimulating discussions with Jörg Kotthaus and Theodor Hänsch. This work was funded by the Max-Planck Society, the Deutsche Forschungsgemeinschaft, the European Union MINOS Project and a Marie Curie Excellence Grant.

References

Anetsberger, G., Arcizet, O., Unterreithmeier, Q. P., Rivière, R., Schliesser, A., Weig, E. M., Kotthaus, J. P., Kippenberg, T. J., 2009. Near-field cavity optomechanics with nanomechanical oscillators. *Nature Physics* 5, 909–914.

- Anetsberger, G., Rivière, R., Schliesser, A., Arcizet, O., Kippenberg, T. J., 2008. Ultralow-dissipation optomechanical resonators on a chip. *Nature Photonics* 2, 627–633.
- Aoki, T., Bayan, D., Wilcut, E., Bowen, W. P., Parkins, A. S., Kippenberg, T. J., Vahala, K. J., Kimble, H. J., 2006. Observation of strong coupling between one atom and a monolithic microresonator. *Nature* 443, 671–674.
- Arcizet, O., 2007. Mesure optique ultrasensible et refroidissement par pression de radiation d'un micro-résonateur mécanique. Ph.D. thesis, Université Paris VI.
- Arcizet, O., Cohadon, P.-F., Briant, T., Pinard, M., Heidmann, A., 2006a. Radiation-pressure cooling and optomechanical instability of a micromirror. *Nature* 444, 71–74.
- Arcizet, O., Cohadon, P.-F., Briant, T., Pinard, M., Heidmann, A., Mackowski, J.-M., Michel, C., Pinard, L., Francais, O., Rousseau, L., 2006b. High-sensitivity optical monitoring of a micromechanical resonator with a quantum-limited optomechanical sensor. *Physical Review Letters* 97, 133601.
- Arcizet, O., Molinelli, C., Briant, T. and Cohadon, P.-F., Heidmann, A., Mackowski, J.-M., Michel, C., Pinard, L., Francais, O., Rousseau, L., 2008. Experimental optomechanics with silicon micromirrors. *New Journal of Physics* 10, 125021.
- Arcizet, O., Rivière, R., Schliesser, A., Anetsberger, G., Kippenberg, T. J., 2009. Cryogenic properties of optomechanical silica microcavities. *Physical Review A* 80, 021803(R).
- Armani, A. M., Kulkarni, R. P., Fraser, S. E., Flagan, R. C., Vahala, K. J., 2007. Label-free, single-molecule detection with optical microcavities. *Science* 317, 783–787.
- Arnold, S., Khoshima, M., Teraoka, I., Holler, S., Vollmer, F., 2003. Shift of whispering-gallery modes in microspheres by protein adsorption. *Optics Letters* 28, 272–274.
- Ashkin, A., 1970. Acceleration and trapping of particles by radiation pressure. *Physical Review Letters* 24, 156–159.
- Ashkin, A., 1978. Trapping of atoms by resonance radiation pressure. *Physical Review Letters* 40, 729–732.
- Bartell, U., Hunklinger, S., 1982. Pressure dependence of the low-temperature acoustic anomalies in vitreous silica. *Journal de Physique Colloques* 43, 498.
- Bhattacharya, M., Giscard, P. L., Meystre, P., JAN 2008a. Entanglement of a Laguerre-Gaussian cavity mode with a rotating mirror. *Physical Review A* 77 (1), 013827.
- Bhattacharya, M., Giscard, P. L., Meystre, P., MAR 2008b. Entangling the rovibrational modes of a macroscopic mirror using radiation pressure. *Physical Review A* 77 (3), 030303.
- Bhattacharya, M., Meystre, P., AUG 17 2007. Trapping and cooling a mirror to its quantum mechanical ground state. *Physical Review Letters* 99 (7), 073601.

- Bjorklund, D. C., Levenson, M. D., Lenth, W., Ortiz, C., 1983. Frequency Modulation (FM) Spectroscopy. *Applied Physics B* 32, 145–152.
- Black, E. D., 2001. An introduction to Pound-Drever-Hall laser frequency stabilization. *American Journal of Physics* 69, 79–87.
- Blair, D. G., Ivanov, E. N., Tobar, M. E., Turner, P. J., van Kann, F., Heng, I. S., 1995. High sensitivity gravitational wave antenna with parametric transducer readout. *Physical Review Letters* 74, 1908–1911.
- Blencowe, M. P., Buks, E., 2007. Quantum analysis of a linear dc squid mechanical displacement detector. *Physical Review B* 76, 014511.
- Blencowe, M. P., Imbers, J., Armour, A. D., 2005. Dynamics of a nanomechanical resonator coupled to a superconducting single-electron transistor. *New Journal of Physics* 7, 236.
- Bocko, M. F., Onofrio, R., 1996. On the measurement of a weak classical force coupled to a harmonic oscillator: experimental progress. *Review of Modern Physics* 68, 755–799.
- Böhm, H. R., Gigan, S., Blaser, F., Zeilinger, A., Aspelmeyer, M., Langer, G., Bäuerle, D., Hertzberg, J. B., Schwab, K. C., 2006. High reflectivity high-Q micromechanical Bragg mirror. *Applied Physics Letters* 89, 223101.
- Bose, S., Jacobs, K., Knight, P. L., 1997. Preparation of nonclassical states in cavities with a moving mirror. *Physical Review A* 56, 4175–4186.
- Braginskii, V. B., Manukin, A. B., 1967. Ponderomotive effects of electromagnetic radiation. *Soviet Physics JETP Letters* 25 (4), 653–655.
- Braginskii, V. B., Manukin, A. B., Tikhonov, M. Y., 1970. Investigation of dissipative ponderomotive effects of electromagnetic radiation. *Soviet Physics JETP* 31, 829–830.
- Braginsky, V. B., Gorodetsky, M., Vyatchanin, S., 2000. Thermo-refractive noise in gravitational wave antennae. *Physics Letters A* 271, 303–307.
- Braginsky, V. B., Gorodetsky, M. L., Ilchenko, V. S., 1989. Quality-factor and nonlinear properties of optical whispering-gallery modes. *Physics Letters A* 137 (7-8), 393–397.
- Braginsky, V. B., Gorodetsky, M. L., Khalili, F. Y., Matsko, A. B., Thorne, K. S., Vyatchanin, S. P., 2003. Noise in gravitational-wave detectors and other classical-force measurements is not influenced by test-mass quantization. *Physical Review D* 67, 082001.
- Braginsky, V. B., Gorodetsky, M. L., Vyatchanin, S. P., 1999. Thermodynamical fluctuations and photo-thermal shot noise in gravitational wave antennae. *Physics Letters A* 264, 1–10.
- Braginsky, V. B., Khalili, F. Y., 1992. *Quantum Measurement*. Cambridge University Press.
- Braginsky, V. B., Khalili, F. Y., 1996. Quantum nondemolition measurements: the route from toys to tools. *Reviews of Modern Physics* 68, 1–11.
- Braginsky, V. B., Manukin, A. B., 1977. *Measurement of Weak Forces in Physics Experiments*. University of Chicago Press.
- Braginsky, V. B., Strigin, S. E., Vyatchanin, V. P., 2001. Parametric oscillatory instability in Fabry-Perot interferometer. *Physics Letters A* 287 (5-6), 331–

338.

- Braginsky, V. B., Vorontsov, Y. I., Khalili, F. Y., 1977. Soviet Physics JETP 46, 705.
- Braginsky, V. B., Vorontsov, Y. I., Thorne, K., 1980. Quantum Nondemolition Measurements. Science 209, 547–557.
- Braginsky, V. B., Vyatchanin, S. P., 2002. Low quantum noise tranquilizer for Fabry-Perot interferometer. Physics Letters A 293, 228–234.
- Brennecke, F., Ritter, S., Donner, T., Esslinger, T., 2008. Cavity optomechanics with a Bose-Einstein condensate. Science 322, 235–238.
- Briant, T., Cohadon, P.-F., Heidmann, A., Pinard, M., 2003. Optomechanical characterization of acoustic modes in a mirror. Physical Review A 68, 033823.
- Brown, K. R., Britton, J., Epstein, R. J., Chiaverini, J., Leibfried, D., Wineland, D. J., 2007. Passive cooling of a micromechanical oscillator with a resonant electric circuit. Physical Review Letters 99 (13), 137205.
URL <http://link.aps.org/abstract/PRL/v99/e137205>
- Caniard, T., Briant, T., Cohadon, P.-F., Pinard, M., Heidmann, A., 2007a. Ultrasensitive optical measurement of thermal and quantum noises. Optics and Spectroscopy 103, 225–230.
- Caniard, T., Verlot, P., Briant, T., Cohadon, P.-F., Heidmann, A., 2007b. Observation of back-action noise cancellation in interferometric and weak force measurements. Physical Review Letters 99, 110801.
- Carmon, T., Cross, M. C., Vahala, K. J., 2007. Chaotic quivering of micron-scaled on-chip resonators excited by centrifugal optical pressure. Physical Review Letters 98, 167203.
- Carmon, T., Rokhsari, H., Yang, L., Kippenberg, T. J., Vahala, K. J., 2005. Temporal behavior of radiation-pressure-induced vibrations of an optical microcavity phonon mode. Physical Review Letters 94 (22), 223902.
- Carmon, T., Vahala, K. J., 2007. Modal spectroscopy of optoexcited vibrations of a micron-scale on-chip resonator at greater than 1 GHz frequency. Physical Review Letters 98, 123901.
- Carmon, T., Yang, L., Vahala, K. J., 2004. Dynamical thermal behavior and thermal selfstability of microcavities. Optics Express 12, 4742–4750.
- Caves, C. M., Jul 1980. Quantum-mechanical radiation-pressure fluctuations in an interferometer. Physical Review Letters 45 (2), 75–79.
- Caves, C. M., 1981. Quantum-mechanical noise in an interferometer. Physical Review D 23, 1693.
- Chang, R. K., Campillo, A. J., 1996. Optical processes in microcavities. World Scientific.
- Chu, S., Hollberg, L., Bjorkholm, J. E., Cable, A., Ashkin, A., Jul 1985. Three-dimensional viscous confinement and cooling of atoms by resonance radiation pressure. Physical Review Letters 55 (1), 48–51.
- Clerk, A. A., Devoret, M. H., Girvin, S. M., Marquardt, F., Schoelkopf, R. J., 2008. Introduction to Quantum Noise, Measurement and Amplification. arXiv:0810.4729.

- Cohadon, P.-F., Heidmann, A., Pinard, M., 1999. Cooling of a mirror by radiation pressure. *Physical Review Letters* 83, 3174–3177.
- Cole, G. D., Gröblacher, S., Gugler, K., Gigan, S., Aspelmeyer, M., 2008. Monocrystalline $\text{Al}_x\text{Ga}_{1-x}\text{As}$ heterostructures for high-reflectivity high-Q micromechanical resonators in the megahertz regime. *Applied Physics Letters* 92, 261108.
- Collot, L., Lefèvre-Seguin, V., Brune, M., Raimond, J. M., Haroche, S., 1993. Very high-Q whispering-gallery mode resonances observed on fused silica microspheres. *Europhysics Letters* 23 (5), 327–334.
- Corbitt, T., Chen, Y., Innerhofer, E., Muller-Ebhardt, H., Ottaway, D., Rehbein, H., Sigg, D., Whitcomb, S., Wipf, C., Mavalvala, N., 2007a. An all-optical trap for a gram-scale mirror. *Physical Review Letters* 98 (15), 150802.
- Corbitt, T., Wipf, C., Bodiya, T., Ottaway, D., Sigg, D., Smith, N., Whitcomb, S., Mavalvala, N., 2007b. Optical dilution and feedback cooling of a gram-scale oscillator to 6.9 mK. *Physical Review Letters* 99 (16), 160801.
URL <http://link.aps.org/abstract/PRL/v99/e160801>
- Cuthbertson, B. D., Tobar, M. E., Ivanov, E. N., Blair, D. G., 1996. Parametric back-action effects in a high-Q cyrogenic sapphire transducer. *Review of Scientific Instruments* 67, 2435–2442.
- Dantan, A., Genes, C., Vitali, D., Pinard, M., 2008. Self-cooling of a movable mirror to the ground state using radiation pressure. *Physical Review A* 77, 011804(R).
- Diedrich, F., Bergquist, J. C., Itano, W. M., Wineland, D. J., Jan 1989. Laser cooling to the zero-point energy of motion. *Physical Review Letters* 62 (4), 403–406.
- Diósi, L., 2008. Laser linewidth hazard in optomechanical cooling. *Physical Review A* 78, 021801.
- Dixon, R. W., 1967. Photoelastic properties of selected materials and their relevance for applications to acoustic light modulators and scanners. *Journal of Applied Physics* 38, 5149.
- Dobrindt, J., Kippenberg, T. J., 2009. Theory of quantum backaction enhancement and displacement measurement using a multiple cavity mode transducer. arxiv.
- Dobrindt, J. M., Wilson-Rae, I., Kippenberg, T. J., 2008. Parametric normal-mode splitting in cavity optomechanics. *Physical Review Letters* 101, 263602.
- Dorsel, A., McCullen, J. D., Meystre, P., Vignes, E., Walther, H., 1983. Optical bistability and mirror confinement induced by radiation pressure. *Physical Review Letters* 51 (17), 1550–1553.
- Drever, R. W. P., Hall, J. L., Kowalski, F. V., Hough, J., Ford, G. M., Munley, A. J., Ward, H., 1983. Laser Phase and Frequency Stabilization Using an Optical Resonator. *Applied Physics B* 31, 97–105.
- Dykman, M. I., 1978. Heating and cooling of local and quasilocal vibrations by a nonresonance field. *Soviet Physics - Solid State* 20, 1306–1311.

- Eichenfield, M., Camacho, R., Chan, J., Vahala, K., Painter, O., 2009a. A picogram and nanometer scale photonic crystal opto-mechanical cavity. *Nature* 459, 550–555.
- Eichenfield, M., Chan, J., Camacho, R. M., Vahala, K. J., Painter, O., 2009b. Optomechanical crystals. *Nature* 462, 78–82.
- Eichenfield, M., Michael, C. P., Perahia, R., Painter, O., 2007. Actuation of micro-optomechanical systems via cavity-enhanced optical dipole forces. *Nature Photonics* 1, 416–422.
- Ekinci, K. L., Roukes, M. L., 2005. Nanoelectromechanical systems. *Review of Scientific Instruments* 76, 061101.
- Fabre, C., Pinard, M., Bourzeix, S., Heidmann, A., Giacobino, E., Reynaud, S., 1994. Quantum-noise reduction using a cavity with a movable mirror. *Physical Review A* 49, 1337–1343.
- Favero, I., Metzger, C., Camerer, S., König, D., Lorenz, H., Kotthaus, J. P., Karrai, K., 2007. Optical cooling of a micromirror of wavelength size. *Applied Physics Letters* 90, 104101.
- Favero, I., Stapfner, S., Hunger, D., Paulitschke, P., Reichel, J., Lorenz, H., Weig, E. M., Karrai, K., 2009. Fluctuating nanomechanical systems in a high finesse optical microcavity. *Optics Express* 17, 12813–12820.
- Fleischhauer, M., Imamoglu, A., Marangos, J. P., 2005. Electromagnetically induced transparency: Optics in coherent media. *Review of Modern Physics* 77, 633–673.
- Fleischhauer, M., Lukin, M. D., 2000. Dark-state polaritons in electromagnetically induced transparency. *Physical Review Letters* 84, 5094–5097.
- Flowers-Jacobs, N. E., Schmidt, D. R., Lehnert, K. W., 2007. Intrinsic noise properties of atomic point contact displacement detectors. *Physical Review Letters* 98, 096804.
- Gardiner, C. W., Zoller, P., 2004. *Quantum Noise*. Springer.
- Genes, C., Vitali, D., Tombesi, P., Gigan, S., Aspelmeyer, M., 2008. Ground-state cooling of a micromechanical oscillator: Comparing cold-damping and cavity-assisted cooling schemes. *Physical Review A* 77, 033804.
- Gigan, S., Böhm, H. R., Paternosto, M., Blaser, F., Langer, G., Hertzberg, J. B., Schwab, K. C., Bäuerle, D., Aspelmeyer, M., Zeilinger, A., 2006. Self-cooling of a micromirror by radiation pressure. *Nature* 444, 67–70.
- Gillespie, A., Raab, F., 1995. Thermally excited vibrations of the mirrors of laser interferometer gravitational wave detectors. *Physical Review D* 52, 577–585.
- Giovannetti, V., Vitali, D., 2001. Phase-noise measurement in a cavity with a movable mirror undergoing quantum Brownian motion. *Physical Review A* 63, 023812.
- Gorodetsky, M. L., Grudinin, I. S., 2004. Fundamental thermal fluctuations in microspheres. *Journal of the Optical Society of America B* 21, 697–705.
- Gozzini, A., Maccarrone, F., Mango, F., Longo, I., Barbarino, S., 1985. Light-pressure bistability at microwave frequencies. *Journal of the Optical Society of America B* 2, 1841.

- Gröblacher, S., Gigan, S., Böhm, H. R., Zeilinger, A., Aspelmeyer, M., 2008. Radiation pressure self-cooling of a micromirror in a cryogenic environment. *Europhysics Letters* 81, 54003.
- Gröblacher, S., Hammerer, K., Vanner, M. R., Aspelmeyer, M., 2009a. Observation of strong coupling between a micromechanical resonator and an optical cavity field. *Nature* 460, 724–727.
- Gröblacher, S., Hertzberg, J. B., Vanner, M. R., Gigan, S., Schwab, K. C., Aspelmeyer, M., 2009b. Demonstration of an ultracold micro-optomechanical oscillator in a cryogenic cavity. *Nature Physics* 5, 485–488.
- Grudin, I., Ilchenko, V. S., Maleki, L., 2006. Ultrahigh optical Q factors of crystalline resonators in the linear regime. *Physical Review A* 74, 063806.
- Hadjar, Y., Cohadon, P. F., Aminoff, C. G., Pinard, M., Heidmann, A., 1999. High-sensitivity optical measurement of mechanical Brownian motion. *Europhysics Letters* 47 (5), 545–551.
- Hahtela, O., Nera, K., Tittonen, I., 2004. Position measurement of a cavity mirror using polarization spectroscopy. *Journal of Optics A* 6, S115–S120.
- Hald, J., Ruseva, V., 2005. Efficient suppression of diode-laser phase noise by optical filtering. *Journal of the Optical Society of America B* 22 (11), 2338–2344.
- Hamann, S. E., Haycock, D. L., Klose, G., Pax, P. H., Deutsch, I. H., Jessen, P. S., May 1998. Resolved-sideband Raman cooling to the ground state of an optical lattice. *Physical Review Letters* 80 (19), 4149–4152.
- Hänsch, T. W., Couillaud, B., 1980. Laser frequency stabilization by polarization spectroscopy of a reflecting reference cavity. *Optics Communications* 35 (3), 441–444.
- Hänsch, T. W., Schawlow, A. L., 1975. Cooling of gases by laser radiation. *Optics Communications* 13, 68–69.
- Harris, J. G. E., Zwickl, B. M., Jayich, A. M., 2007. Stable, mode-matched, medium-finesse optical cavity incorporating a micromechanical cantilever. *Review of Scientific Instruments* 78, 013107.
- Hau, L. V., Harris, S. E., Dutton, Z., Behroozi, C. H., 1999. Light speed reduction to 17 metres per second in an ultracold atomic gas. *Nature* 397, 594–598.
- Haus, H. A., 1984. *Waves and fields in optoelectronics*. Prentice-Hall.
- Heidmann, A., Hadjar, Y., Pinard, M., 1997. Quantum non-demolition measurement by optomechanical coupling. *Applied Physics B* 64, 173–180.
- Hertzberg, J. B., Rocheleau, T., Ndukum, T., Savva, M., Clerk, A. A., Schwab, K. C., 2009. Back-action evading measurements of nanomechanical motion. [arxiv:0906.0967](https://arxiv.org/abs/0906.0967).
- Hofer, J., Schliesser, A., Kippenberg, T. J., 2009. Cavity optomechanics with ultra-high Q crystalline micro-resonators. [arXiv:0911.1178](https://arxiv.org/abs/0911.1178).
- Höhberger Metzger, C., Karrai, K., 2004. Cavity cooling of a microlever. *Nature* 432, 1002–1005.
- Hosseini-Zadeh, M., Rokhsari, H., Hajimiri, A., Vahala, K. J., 2006. Characterization of a radiation-pressure-driven micromechanical oscillator. *Physical*

- Review A 74, 023813.
- Hossein-Zadeh, M., Vahala, K., 2007. Observation of optical spring effect in a microtoroidal optomechanical resonator. *Optics Letters* 32 (12), 1611–1613.
- Hunklinger, S., Arnold, W., Stein, S., 1973. Anomalous ultrasonic attenuation in vitreous silica at low temperatures. *Physics Letters* 45A, 311–312.
- Hutchinson, J. R., 1979. Axisymmetric flexural vibrations of a thick free circular plate. *Journal of Applied Mechanics* 46, 139–144.
- Hutchinson, J. R., 1980. Vibrations of solid cylinders. *Journal of Applied Mechanics* 47, 901–907.
- Ilchenko, V., Volikov, P. S., Velichanski, V. L., Treussart, V. L., Lefèvre-Seguin, V., Raimond, J.-M., Haroche, S., 1998. Strain-tunable high-Q optical microresonator. *Optics Communications* 145, 86–90.
- Ilchenko, V. S., Gorodetsky, M. L., Vyatchanin, S. P., 1994. Coupling and tunability of optical whispering-gallery modes: a basis for coordinate meter. *Optics Communications* 107, 41–48.
- Itano, W. M., Bergquist, J. C., Bollinger, J. J., Wineland, D. J., 1992. Laser cooling of trapped ions. *Laser Manipulation of Atoms and Ions*. North-Holland, Amsterdam, pp. 519–537S.
- Jäckle, J., 1972. On the ultrasonic attenuation in glasses at low temperature. *Zeitschrift für Physik* 257, 212–223.
- Kash, M. M., Sautenkov, V. A., Zibrov, A. S., Hollberg, L., Welch, G. R., Lukin, M. D., Rostovtsev, Y., Fry, E. S., Scully, M. O., 1999. Ultraslow group velocity and enhanced nonlinear optical effects in a coherently driven hot atomic gas. *Physical Review Letters* 82, 5229–5232.
- Kippenberg, T. J., Rokhsari, H., Carmon, T., Scherer, A., Vahala, K. J., 2005. Analysis of Radiation-Pressure Induced Mechanical Oscillation of an Optical Microcavity. *Physical Review Letters* 95, 033901.
- Kippenberg, T. J., Rokhsari, H., Vahala, K., 2006. Scanning probe microscopy of thermally excited mechanical modes of an optical microcavity. [arxiv:0602234](https://arxiv.org/abs/0602234).
- Kippenberg, T. J., Spillane, S. M., Vahala, K. J., 2004. Kerr-nonlinearity optical parametric oscillation in an ultrahigh-Q toroid microcavity. *Physical Review Letters* 93 (8), 083904.
- Kippenberg, T. J., Vahala, K., 2007. Cavity Opto-Mechanics. *Optics Express* 15, 17172–17205.
- Kippenberg, T. J., Vahala, K. J., 2008. Cavity Optomechanics: Back-Action at the Mesoscale. *Science* 321, 1172–1176.
- Kleckner, D., Bouwmeester, D., 2006. Sub-kelvin optical cooling of a micromechanical resonator. *Nature* 444, 75–78.
- Kleckner, D., Marshall, W., De Dood, J. M. A., Khodadad, N. D., Pors, B.-J., Irvine, W. T. M., Bouwmeester, D., 2006. High finesse opto-mechanical cavity with a movable thirty-micron-size mirror. *Physical Review Letters* 96, 173901.
- Knobel, R. G., Cleland, A. N., 2003. Nanometre-scale displacement sensing using a single-electron transistor. *Nature* 424, 291–293.

- LaHaye, M. D., Buu, O., Camarota, B., Schwab, K. C., 2004. Approaching the quantum limit of a nanomechanical resonator. *Science* 304, 74–77.
- Landau, L. D., Lifshitz, E. M., 1970. Theory of elasticity, 2nd Edition. Vol. 7 of Course of Theoretical Physics. Pergamon Press.
- Landau, L. D., Lifshitz, E. M., 1980. Statistical Physics, 3rd Edition. Vol. 5 of Course of Theoretical Physics. Pergamon Press.
- Landau, L. D., Lifshitz, E. M., 1984. Electrodynamics of continuous media, 2nd Edition. Vol. 8 of Course of Theoretical Physics. Pergamon Press.
- Landau, L. D., Lifshitz, E. M., 1987. Fluid Mechanics, 2nd Edition. Vol. 6 of Course of Theoretical Physics. Pergamon Press.
- Law, C. K., 1995. Interaction between a moving mirror and radiation pressure: A Hamiltonian formulation. *Physical Review A* 51, 2537–2541.
- Lebedew, P., 1901. Untersuchungen über die Druckkräfte des Lichtes. *Annalen der Physik* 311, 433–458.
- Leibfried, D., Blatt, R., Monroe, C., Wineland, D., Mar 2003. Quantum dynamics of single trapped ions. *Review of Modern Physics* 75 (1), 281–324.
- Li, M., Pernice, W. H. P., Xiong, C., Baehr-Jones, T., Hochberg, M., Tang, H. X., 2008. Harnessing optical forces in integrated photonic circuits. *Nature* 456, 480–484.
- LIGO Scientific Collaboration, 2009. Observation of a kilogram-scale oscillator near its quantum ground state. *New Journal of Physics* 11 (7), 073032.
- Lin, Q., Rosenberg, J., Jiang, X., Vahala, K. J., Painter, O., 2009. Mechanical oscillation and cooling actuated by the optical gradient force. [arxiv:0905.2716](https://arxiv.org/abs/0905.2716).
- Liu, C., Dutton, Z., Behroozi, C., Hau, L., 2001. Observation of coherent optical information storage in an atomic medium using halted light pulses. *Nature* 409, 490–493.
- Locke, C. R., Tobar, M. E., 2004. Measurement of the strain-induced coefficient of permittivity of sapphire using whispering gallery modes excited in a high-Q acoustic sapphire oscillator. *Measurement Science and Technology* 15, 2145–2149.
- Locke, C. R., Tobar, M. E., Ivanov, E. N., Blair, D. G., 1998. Parametric interaction of the electric and acoustic fields in a sapphire monocrystal transducer with a microwave readout. *Journal of Applied Physics* 84, 6523–6527.
- Love, A. E. H., 1926. A treatise on the mathematical theory of elasticity. Cambridge University Press.
- Ludwig, M., Kubala, B., Marquardt, F., 2008a. The optomechanical instability in the quantum regime. *New Journal of Physics* 10, 095013.
- Ludwig, M., Neuenhahn, C., Metzger, C., Ortlieb, A., Favero, I., Karrai, K., Marquardt, F., 2008b. Self-induced oscillations in an optomechanical system driven by bolometric backaction. *Physical Review Letters* 101, 133903.
- Ma, R., Schliesser, A., Del’Haye, P., Dabirian, A., Anetsberger, G., Kippenberg, T., 2007. Radiation-pressure-driven vibrational modes in ultrahigh-Q silica microspheres. *Optics Letters* 32, 2200–2202.
- Mancini, S., Giovannetti, V., Vitali, D., Tombesi, P., 2002. Entangling Macro-

- scopic Oscillators Exploiting Radiation Pressure. *Physical Review Letters* 88, 120401.
- Mancini, S., Tombesi, P., 1994. Quantum noise reduction by radiation pressure. *Physical Review A* 49, 4055–4065.
- Marquardt, F., Chen, J. P., Clerk, A. A., Girvin, S. M., 2007. Quantum theory of cavity-assisted sideband cooling of mechanical motion. *Physical Review Letters* 99, 093902.
- Marquardt, F., Harris, J. G. E., Girvin, S. M., 2006. Dynamical multistability induced by radiation pressure in high-finesse micromechanical optical cavities. *Physical Review Letters* 96 (10), 103901.
URL <http://link.aps.org/abstract/PRL/v96/e103901>
- Marshall, W., Simon, C., Penrose, R., Bouwmeester, D., 2003. Towards Quantum Superpositions of a Mirror. *Physical Review Letters* 91, 130401.
- Martin, I., Shnirman, A., Tian, L., Zoller, P., 2004. Ground-state cooling of mechanical oscillators. *Physical Review B* 69, 125339.
- Matsko, A. B., Savchenko, A. A., Yu, N., Maleki, L., 2007. Whispering-gallery-mode resonators as frequency references. I. fundamental limitations. *Journal of the Optical Society of America B* 24, 1324–1335.
- Milatz, J. M. W., van Zolingen, J. J., 1953. The Brownian motion of electrometers. *Physica* 19, 181–194.
- Milatz, J. M. W., van Zolingen, J. J., van Iperen, B. B., 1953. The reduction in the Brownian motion in electrometers. *Physica* 19, 195–207.
- Milonni, P. W., 2005. *Fast light, slow light and left-handed light*. Taylor and Francis.
- Möhl, D., Petrucci, G., Thorndahl, L., van der Meer, S., 1980. Physics and technique of stochastic cooling. *Physics Reports* 58, 73–102.
- Monroe, C., Meekhof, D. M., King, B. E., Jefferts, S. R., Itano, W. M., Wineland, D. J., Gould, P., 1995. Resolved-sideband raman cooling of a bound atom to the 3d zero point energy. *Physical Review Letters* 75 (22), 4011–4014.
- Mow-Lowry, C. M., Mullavey, A. J., Goler, S., Gray, M. B., McClelland, D. E., 2008. Cooling of a gram-scale cantilever flexure to 70 mK with a servo-modified optical spring. *Physical Review Letters* 100, 010801.
- Murch, K. W., Moore, K. L., Gupta, S., Stamper-Kurn, D. M., 2008. Observation of quantum-measurement backaction with an ultracold atomic gas. *Nature Physics* 4, 561–564.
- Naik, A., Buu, O., LaHaye, M. D., Armour, A. D., Clerk, A. A., Blencowe, M. P., Schwab, K. C., 2006. Cooling a nanomechanical resonator with quantum back-action. *Nature* 443, 193–196.
- Nawrodt, R., Zimmer, A., Koettig, T., Nietzsche, S., Thürk, M., Vodel, M., Seidel, P., 2007. High mechanical Q-factor measurements on calcium fluoride at cryogenic temperatures. *European Physical Journal - Applied Physics* 38, 53–59.
- Nichols, E. F., Hull, G. F., 1901. A preliminary communication on the pressure of heat and light radiation. *Physical Review* 13, 307–320.

- Nichols, E. F., Hull, G. F., 1903a. The pressure due to radiation. *Physical Review* 17, 26–50.
- Nichols, E. F., Hull, G. F., 1903b. The pressure due to radiation. *Physical Review* 17, 91–104.
- Nowacki, W., 1975. *Dynamic problems of thermoelasticity*. Springer.
- Park, Y.-S., Wang, H., 2009. Resolved-sideband and cryogenic cooling of an optomechanical resonator. *Nature Physics* 5, 489–493.
- Park, Y. S., Wang, H. L., 2007. Radiation pressure driven mechanical oscillation in deformed silica microspheres via free-space evanescent excitation. *Optics Express* 15, 16471–16477.
- Pfeifer, R. N. C., Nieminen, T. A., Heckenberg, N. R., Rubinsztein-Dunlop, H., 2007. Colloquium: Momentum of an electromagnetic wave in dielectric media. *Reviews of Modern Physics* 79, 1197–1216.
- Phillips, D. F., Fleischhauer, A., Mair, A., Walsworth, R. L., Lukin, M. D., 2001. Storage of light in atomic vapor. *Physical Review Letters* 86, 783–786.
- Pinard, M., Cohadon, P. F., Briant, T., Heidmann, A., 2000. Full mechanical characterization of a cold damped mirror. *Physical Review A* 63, 013808.
- Pinard, M., Dantan, A., Vitali, D., Arcizet, O., Briant, T., Heidmann, A., 2005. Entangling movable mirrors in a double-cavity system. *Europhysics Letters* 72, 747–753.
- Pinard, M., Hadjar, Y., Heidmann, A., 1999. Effective mass in quantum effects of radiation pressure. *European Physics Journal D* 7, 107–116.
- Poggio, M., Degen, L., Mamin, J. J., Rugar, D., 2007. Feedback cooling of a cantilever’s fundamental mode below 5 mK. *Physical Review Letters* 99, 017201.
- Pohl, R. O., Liu, X., Thompson, E., 2002. Low-temperature thermal conductivity and acoustic attenuation in amorphous solids. *Review of Modern Physics* 74, 991–1013.
- Raab, C., Eschner, J., Bolle, J., Oberst, H., Schmidt-Kaler, F., Blatt, R., 2000. Motional sidebands and direct measurement of the cooling rate in the resonance fluorescence of a single trapped ion. *Physical Review Letters* 85 (3), 538.
- Rabl, P., Genes, C., Hammerer, K., Aspelmeyer, M., 2009. Phase-noise induced limitations in resolved-sideband cavity cooling of mechanical resonators. [arxiv:0903.1637](https://arxiv.org/abs/0903.1637).
- Regal, C. A., Teufel, J. D., Lehnert, K. W., 2008. Measuring nanomechanical motion with a microwave cavity interferometer. *Nature Physics* 4, 555–560.
- Rehbein, H., Harms, J., Schnabel, R., Danzmann, K., 2005. Optical transfer functions of Kerr nonlinear cavities and interferometers. *Physical Review Letters* 95, 193001.
- Rempe, G., Thomson, R. J., Kimble, H. J., Lalezari, R., 1992. Measurement of ultralow losses in an optical interferometer. *Optics Letters* 17, 363–365.
- Rivière, R., Arcizet, O., Schliesser, A., Anetsberger, G., Kippenberg, T., 2010. Design and operation of a cryogenic taper-coupling setup for cavity optomechanical experiments(in preparation).

- Rokhsari, H., Kippenberg, T. J., Carmon, T., Vahala, K. J., 2005. Radiation-pressure-driven micro-mechanical oscillator. *Optics Express* 13, 5293–5301.
- Rokhsari, H., Kippenberg, T. J., Carmon, T., Vahala, K. J., 2006. Theoretical and experimental study of radiation pressure-induced mechanical oscillations (parametric instability) in optical microcavities. *IEEE Journal of Selected Topics in Quantum Electronics* 12 (1), 96–107.
- Sandoghdar, V., Treussart, F., Hare, J., Lefèvre-Seguin, V., Raimond, J.-M., Haroche, S., 1996. Very low threshold whispering-gallery-mode microsphere laser. *Physical Review A* 54 (3), R1777–R1780.
- Schliesser, A., Anetsberger, G., Rivière, R., Arcizet, O., Kippenberg, T. J., 2008a. High-sensitivity monitoring of micromechanical vibration using optical whispering gallery mode resonators. *New Journal of Physics* 10, 095015.
- Schliesser, A., Arcizet, O., Rivière, R., Anetsberger, G., Kippenberg, T., 2009. Resolved-sideband cooling and position measurement of a micromechanical oscillator close to the Heisenberg uncertainty limit. *Nature Physics* 5, 509–514.
- Schliesser, A., Del’Haye, P., Nooshi, N., Vahala, K., Kippenberg, T., 2006. Radiation pressure cooling of a micromechanical oscillator using dynamical backaction. *Physical Review Letters* 97, 243905.
- Schliesser, A., Rivière, R., Anetsberger, G., Arcizet, O., Kippenberg, T., 2008b. Resolved-sideband cooling of a micromechanical oscillator. *Nature Physics* 4, 415–419.
- Schröter, B., Reich, C., Arcizet, O., Rädler, J. O., Nickel, B., Kippenberg, T. J., 2008. Chip based, lipid bilayer functionalized microresonators for label-free, ultra sensitive and time-resolved molecular detection. submitted.
- Schwab, K. C., Roukes, M. L., 2005. Putting mechanics into quantum mechanics. *Physics Today* 58 (7), 36–42.
- Sheard, B. S., Gray, M. B., Mow-Lowry, C. M., McClelland, D. E., Whitcomb, S. E., 2004. Observation and characterization of an optical spring. *Physical Review A* 69, 051801.
- Spillane, S. M., Kippenberg, T. J., Painter, O. J., Vahala, K. J., 2003. Ideality in a fiber-taper-coupled microresonator system for application to cavity quantum electrodynamics. *Physical Review Letters* 91 (4), 043902.
- Spillane, S. M., Kippenberg, T. J., Vahala, K. J., 2002. Ultralow-threshold Raman laser using a spherical dielectric microcavity. *Nature* 415 (6872), 621–623.
- Srinivasan, K., Painter, O., 2007. Optical fiber taper coupling and high-resolution wavelength tuning of microdisk resonators at cryogenic temperatures. *Applied Physics Letters* 90, 031114.
- Stenholm, S., 1986. The semiclassical theory of laser cooling. *Reviews of Modern Physics* 58, 699–739.
- Tamura, S.-I., 2009. Vibrational cavity modes in a free cylindrical disk. *Physical Review B* 79, 054302.
- Teufel, J. D., Donner, R., Castellanos-Beltran, M. A., Harlow, J. W., Lehnert, K. W., 2009. Nanomechanical motion measured with precision beyond the

- standard quantum limit. arxiv.
- Teufel, J. D., Harlow, J. D., Regal, C. A., Lehnert, K. W., 2008. Dynamical backaction of microwave fields on a nanomechanical oscillator. *Physical Review Letters* 101, 197203.
- Thomson, J. D., Zwickl, B. M., Jayich, A. M., Marquardt, F., Girvin, S. M., Harris, J. G. E., 2008. Strong dispersive coupling of a high finesse cavity to a micromechanical membrane. *Nature* 452, 72–75.
- Tian, L., Zoller, P., 2004. Coupled ion-nanomechanical systems. *Physical Review Letters* 93 (26), 266403.
- Tielburger, D., Merz, R., Ehrenfels, R., Hunklinger, S., 1992. Thermally activated relaxation processes in vitreous silica: An investigation by Brillouin scattering at high pressures. *Physical Review B* 45, 2750–2760.
- Tittonen, I., Breitenbach, G., Kalkbrenner, T., Muller, T., Conradt, R., Schiller, S., Steinsland, E., Blanc, N., de Rooij, N. F., 1999. Interferometric measurements of the position of a macroscopic body: Towards observations of quantum limits. *Physical Review A* 59, 1038–1044.
- Treussart, F., Ilchenko, V. S., Roch, J.-F., Hare, J., Lefevre-Seguin, V., Raymond, J.-M., Haroche, S., 1998. Evidence for intrinsic Kerr bistability of high-Q resonators in suprafluid helium. *European Physical Journal D* 1, 235–238.
- Vacher, R., Courtens, E., Foret, M., 2005. Anharmonic versus relaxational sound damping in glasses. II. Vitreous silica. *Physical Review B* 72, 214205.
- Vahala, K., Herrmann, M., Knunz, S., Batteiger, V., Saathoff, G., Hansch, T. W., Udem, T., 2009. A phonon laser. *Nature Physics Advance online publication*.
- Vahala, K. J., 2008. Back-action limit of linewidth in an optomechanical oscillator. *Physical Review A* 78, 023832.
- Vassiliev, V. V., Velichansky, V. L., Ilchenko, V. S., Gorodetsky, M. L., Hollberg, L., Yarovitsky, A. V., 1998. Narrow-line-width diode laser with a high-Q microsphere resonator. *Optics Communications* 158 (1-6), 305–312.
- Verbridge, S. S., Craighead, H. G., Parpia, J. M., 2008. A megahertz nanomechanical resonator with room temperature quality factor over a million. *Applied Physics Letters* 92, 013112.
- Verbridge, S. S., Shapiro, D. F., Craighead, H. G., Parpia, J. M., Jeevak, M., 2007. Macroscopic tuning of nanomechanics: Substrate bending for reversible control of frequency and quality factor of nanostring resonators. *Nano Letters* 7, 1728–1735.
- Verlot, P., Tavernarakis, A., Briant, T., Cohadon, P.-F., Heidmann, A., 2008. Scheme to probe optomechanical correlations between two optical beams down to the quantum level. *Physical Review Letters* 102, 103601.
- Vernooy, D. W., Furusawa, A., Georgiades, A. P., Ilchenko, V. S., Kimble, H. J., 1998a. Cavity QED with high-Q whispering gallery modes. *Physical Review A* 57, R2293–R2296.
- Vernooy, D. W., Ilchenko, V. S., Mabuchi, H., Sreed, W. W., Kimble, H. J., 1998b. High-Q measurements of fused-silica microspheres in the near in-

- frared. *Optics Letters* 23 (4), 247–249.
- Vinante, A., Bignotto, M., Bonaldi, M., Cerdonio, M., Conti, L., Falferi, P., Liguori, N., Longo, R., Mezzena, R., Ortolan, A., Prodi, G. A., Salemi, F., Taffarello, L., Vedovato, G., Vitale, S., Zendri, J.-P., 2008. Feedback cooling of the normal modes of a massive electromechanical system to submillikelvin temperature. *Physical Review Letters* 101, 033601.
- Vitali, D., Gigan, S., Ferreira, A., Bohm, H. R., Tombesi, P., Guerreiro, A., Vedral, V., Zeilinger, A., Aspelmeyer, M., 2007. Optomechanical entanglement between a movable mirror and a cavity field. *Physical Review Letters* 98, 030405.
- Vollmer, F., Arnold, S., Keng, D., 2009. Single virus detection from the reactive shift of a whispering-gallery mode. *PNAS* 105, 20701–20704.
- Vollmer, F., Braun, D., Libchaber, A., Khoshshima, M., Teraoka, I., Arnold, S., 2002. Protein detection by optical shift of a resonant microcavity. *Applied Physics Letters* 80 (21), 4057–4059.
- Weld, D. M., Kapitulnik, A., 2006. Feedback control and characterization of a microlever using optical radiation pressure. *Applied Physics Letters* 89, 164102.
- White, G. K., 1975. Thermal expansion of vitreous silica at low temperatures. *Physical Review Letters* 34, 204–205.
- Wilson-Rae, I., 2008. Intrinsic dissipation in nanomechanical resonators due to phonon tunneling. *Physical Review B* 77, 245418.
- Wilson-Rae, I., Nooshi, N., Zwerger, W., Kippenberg, T. J., 2007. Theory of ground state cooling of a mechanical oscillator using dynamical backaction. *Physical Review Letters* 99 (9), 093901.
- Wilson-Rae, I., Zoller, P., Imamoglu, A., 2004. Laser cooling of a nanomechanical resonator mode to its quantum ground state. *Physical Review Letters* 92 (7), 075507.
- Wineland, D. J., Dehmelt, H., 1975. Proposed $10^{14}\delta\nu < \nu$ Laser Fluorescence Spectroscopy on Tl^+ Ion Mono-Oscillator. *Bulletin of the American Physical Society* 20, 637.
- Wineland, D. J., Itano, W. M., 1979. Laser cooling of atoms. *Physical Review A* 20, 1521–1540.
- Woodruff, A. E., 1968. The radiometer and how it does not work. *The Physics Teacher* 6, 358–363.
- Yuen, H. P., Chan, V. W. S., 1983. Noise in homodyne and heterodyne detection. *Optics Letters* 8, 177–179.
- Zener, C., 1937. Internal friction in solids i. theory of internal friction in reeds. *Physical Review* 52, 230–235.
- Zener, C., 1938. Internal friction in solids II. General theory of thermoelastic internal friction. *Physical Review* 53, 90–99.
- Zhang, J., Peng, K., Braunstein, S. L., 2003. Quantum-state transfer from light to macroscopic oscillators. *Physical Review A* 68, 013808.
- Zhang, T. C., Poizat, J. P., et al., 1995. Quantum noise of free-running and externally-stabilized laser diodes. *Quantum and semiclassical optics* 7, 601–

613.

Zhou, X., Arcizet, O., Schliesser, A., Rivière, R., Kippenberg, T., 2009. in preparation.

Zwickl, B. M., Shanks, W. E., Jayich, A. M., Yang, C., Bleszynski Jayich, C., Thomson, J. D., Harris, J. G. E., 2008. High quality mechanical and optical properties of commercial silicon nitride membranes. *Applied Physics Letters* 92, 103125.